The Pennsylvania State University

The Graduate School

Department of Meteorology

PROBABILISTIC ESTIMATION AND VALIDATION OF REGIONAL CLIMATE CHANGE USING STATISTICAL DOWNSCALING METHODS

A Dissertation in

Meteorology

by

Liang Ning

Submitted in Partial Fulfillment
of the Requirements
for the Degree of

Doctor of Philosophy

August 2012

The dissertation of Liang Ning was reviewed and approved* by the following:

Michael E. Mann
Professor of Meteorology
Dissertation Co-Advisor
Co-Chair of Committee

Robert Crane
Professor of Geography
Dissertation Co-Advisor
Co-Chair of Committee

Raymond G. Najjar, Jr.
Professor of Oceanography

Thorsten Wagener
Associate Professor of Civil and Environmental Engineering

Johannes Verlinde
Professor of Meteorology
Associate Head of the Department of Meteorology

*Signatures are on file in the Graduate School

ABSTRACT

Two applications of regional climate changes are presented of a statistical downscaling method based on self-organizing maps (SOMs). The first application produces high-resolution, downscaled precipitation estimates over the state of Pennsylvania in the Mid-Atlantic region of the U.S. using synoptic circulation data from the National Center for Environmental Prediction (NCEP) and nine General Circulation Models (GCMs). The downscaling approach provides a faithful reproduction of the observed probability distributions and temporal characteristics of precipitation on both daily and monthly time scales. The downscaled precipitation field shows significant improvement over the raw GCM precipitation fields with regard to observed average monthly precipitation amounts, average monthly numbers of rainy days, and standard deviations of monthly precipitation amounts.

When applied to the future period 2046-2065, downscaling predicts an increase in annual and winter precipitation and a decrease in summer precipitation when ensemble averaged across the nine GCMs. In order to examine the sensitivity of precipitation change to the water vapor increase brought by global warming, two downscaling approaches are used: one includes the specific humidity in the downscaling algorithm and the other does not. The downscaled precipitation increases employing specific humidity are larger than those without it, and both of them are smaller than those increases from raw GCM simulations. And application of downscaling reduces the inter-GCM variation, suggesting that some of spread among models in the raw projected precipitation may result from differences in precipitation parameterization schemes rather than fundamentally different climate responses. Projected changes in the North Atlantic Oscillation (NAO) are found to be significantly related to changes in winter precipitation in the downscaled results but not for the raw GCM results, suggesting that the downscaling more effectively captures the influence of climate dynamics on projected changes in winter precipitation.

The second application of the downscaling method is the probabilistic estimation of temperature change over Central Africa as input for a malaria transmission model. The downscaled temperature data are then evaluated using the malaria transmission model requirements. The downscaled annual cycles and PDFs of maximum temperature, minimum temperature, average temperature, and diurnal temperature range (DTR), closely match observed annual cycles and probability distributions. And the downscaled time series of the monthly number of days with daily maximum temperature and minimum temperature within malaria development thresholds closely reproduce the observed variability on seasonal to interannual scales.

From period 1961-2000 to period 2046-2065, the downscaled ensemble average maximum temperature, minimum temperature, and average temperature increase by 1.5 ºC and the DTR decreases. The annual and boreal winter average temperature increases over West Africa are larger than those over East Africa and West Coastal Africa. The annual and boreal summer DTR decreases over West Africa are larger than those over the other two regions, and the results for boreal winter months are opposite.

The validations and probabilistic projections on the downscaling method show that this statistical downscaling method is capable of bridging the gap between coarse-resolution GCM output and the requirements of high-resolution input from the end users, on the inter-disciplinary studies about future climate impacts to hydrology, ecology, and human health.

TABLE OF CONTENTS

LIST OF FIGURES

LIST OF TABLES

ACKNOWLEDGEMENTS

The completion of this dissertation would not have been possible without the guidance from my advisors Dr. Michael E. Mann and Dr. Robert Crane. I would like to show my deepest gratitude to them for their excellent supervision, guidance, advice, and patience on the every step of this research as well as providing me extraordinary atmosphere throughout the work. Their scientific understanding and innovation, and constant enthusiasm on climate research will give me great benefit for my future research.

I am grateful to my committee members Dr. Raymond G. Najjar Jr. and Dr. Thorsten Wagener for their guidance and enlightenment through this research. I would also like to thank Dr. Eugene Clothiaux for his helpful suggestions and encouragement, and Dr. Bruce Hewitson for providing the downscaling code.

I am grateful to Dr. Zhihua Zhang, Dr. Fangxing Fan, and Ms. Sonya Miller who provide scientific help and technical assistance.

This research was supported by the Office of Science (BER), U.S. Department of Energy, Grant No. DE-FG02-08ER64641.

Finally, I would like to thank my family, especially my parents, my wife Lili Lei, and my daughter, Ellie Yuxuan Ning, for their love and support.

Chapter 1

Introduction

Recent studies indicate that the global mean surface has risen by 0.74 °C ± 0.18 °C when estimated by a linear trend over the last century, and this warming has brought a series of consequences, such as lower-tropospheric warming, increased intensity of tropical cyclones, and more frequent drought over the tropics and subtropics (Trenberth et al., 2007). Based on the Claussius-Clapeyron equation, the tropospheric warming will induce increased saturated water vapor pressure at a rate of approximately 7% per degree Kelvin of warming (Collins et al., 2010). This increased tropospheric water vapor (Willett et al., 2010) has likely resulted in inhomogeneous precipitation changes, with increased precipitation over land north of 30 °N and decreased precipitation over the tropics for the last several decades (Trenberth et al., 2007), and substantial increases in extreme precipitation frequency and intensity over different regions (e.g., Frich et al., 2002; Kharin and Zwiers, 2005; Ning and Qian, 2009).

Based on the simulations of General Circulation Models (GCMs) driven mainly by increases in anthropogenic greenhouse gas concentrations, with the warming proportional to the associated radiative forcing, the global mean surface temperature will continue to increase in the future, with a series of high-impact consequences, such as more intense and frequent heat waves, inhomogeneous mean precipitation changes, increased precipitation extremes over tropical and high-latitude areas, greater risk of droughts over mid-continental areas, more intense tropical cyclones, and melting snow and ice cover (Meehl et al., 2007).

Regional influences from global warming

On the regional scale, greenhouse gas increases will induce more significant influences, such as higher warming and increased spatial precipitation variability. In this study, we mainly focus on two regions: the Mid-Atlantic region of the U.S. and Central Africa. Over the Mid-Atlantic region, Christensen et al. (2007) find that the annual mean warming is likely to exceed the global-mean warming, and the annual-mean precipitation is very likely to increase, with decreased snow season length and snow depth. When using statistical and dynamical downscaling methods to simulate the regional climate-change projections for the Northeast U.S., Hayhoe et al. (2008) find temperature increases over the whole region with larger magnitudes at higher latitudes and inland, as well as the potential for changing precipitation patterns, particularly along the coast. Over Central Africa, the warming is very likely to be larger than the global annual mean warming throughout the continent and in all seasons, and the annual and winter precipitation are going to increase over tropical Africa, especially East Africa (Christensen et al., 2007). These potential regional precipitation and temperature changes will induce notable economical, environmental, and ecological impacts to local societies.

Over the Mid-Atlantic region, one important influence from climate change is the implications on regional hydrological system, such as intensification of the hydrological cycle and increase in extreme hydrological events (Shortle et al., 2009; Trenberth et al., 2007). These climate-induced changes in the hydrological cycle will affect the water demand, water quality, as well as the availability of water to meet growing demand (Frederick and Gleick, 1999). When examining the past and future changes in hydrological indicators over Northeast U.S., Hayhoe et al. (2006) find that the trends of the hydrological indicators are consistent with the warmer climate, and the magnitudes of the temperature-driven trends are sensitive to the emission scenarios.

Over Central Africa, one serious ecological problem brought by the warming is the resurgence of malaria. Malaria is a mosquito-borne disease caused by a parasite, and in 2010, an estimated 216 million cases of malaria occurred worldwide causing 655,000 deaths, most (91%) of which were in Africa (www.cdc.gov/malaria). Malaria is extremely sensitive to climate change. For example, Patz et al. (2002) indicate that the increase of temperature is a major reason for the recent resurgence in the East African highlands. Pascual et al. (2006) also show that over the East African highlands, even a mere 0.5 °C increase in temperature can translate into a 30-100% increase in mosquito abundance, known as "biological amplification." Ebi et al. (2005) use an ensemble of climate projections to find that, assuming no future human-imposed constraints on malaria transmission, changes in temperature and precipitation could alter the geographic distribution of malaria in Zimbabwe, with previously unsuitable areas of dense human population becoming suitable for transmission. Thus, the assessment of potential change in malaria risk due to past and projected warming trends is one of the most important questions at the interface of climate science and human health (Patz and Olson, 2006).

Most previous studies of the influence of climate on malaria focus on the impacts from mean temperature changes (e.g. Craig et al., 1999); however, Paaijmans et al. (2010) show that in addition to mean temperature, daily fluctuations in temperature affect parasite infection, the rate of parasite development, and essential elements of mosquito biology that combine to determine malaria transmission intensity.

Introduction of the downscaling method

Although the GCMs are the major tools to predict future climate change, their coarse resolution limits their ability and utility for providing detailed regional information for inter-disciplinary studies, such as hydrology, ecology, and human health. In order to overcome this

disadvantage, GCM simulations need to be downscaled to generate the required higher resolution data (Maraun et al., 2010). GCM simulations have been combined with hydrological modeling to predict future runoff changes and assess the impact of different climate change scenarios over different regions (Fowler et al., 2007). Probabilistic frameworks have been developed by combining information from an ensemble of GCMs, greenhouse gas emission scenarios, downscaling methods, and hydrological models, to assess the uncertainties in future hydrological projections and help decision-makers adapt to the climate change impacts on hydrology (e.g., Wilby and Harris, 2006). Downscaling methods have been widely used in the recent hydrological studies in U.S. For example, although different GCMs predict significantly different regional responses to increasing atmospheric CO_2, forced with downscaled GCM temperature and precipitation projections, streamflow changes over California are robust across different models: decreases in summer low flows and increases in winter flow, and a shift of flow to earlier in the year (Maurer and Duffy, 2005). Hayhoe et al. (2006) use the downscaled results from nine GCMs to examine past and future changes in hydrological and biophysical indicators across the U.S. Northeast, and find that all the indicator trends are consistent with the future warmer climate. Take southeast Australia for another example, when Chiew et al. (2010) apply five downscaling methods to the raw rainfall data from three GCMs to run a rainfall-runoff model, they find that all the downscaling methods can generally reproduce the observed historical rainfall characteristics over southeast Australia, and the differences between the modeled future runoff using different downscaled rainfall can be significant. Six downscaling methods are compared on multi-site daily precipitation over 30 rain gauges located within Southeastern Australia by Frost et al. (2011), and it is found that all the methods can reproduce observations reasonably, and different methods show different advantages.

There are two main approaches to downscaling: dynamical downscaling, which uses a high-resolution Regional Climate Model (RCM) driven by a low-resolution output from an GCM,

and statistical downscaling, which applies the relationships derived from observations to the GCM output to generate high-resolution results. Compared with dynamical downscaling, statistical downscaling has a lower computational cost and more flexible resolution, so it is becoming increasingly popular in climate studies (Christensen et al., 2007). For example, a relatively simple analog method has been used to downscale GCM-simulated large-scale circulation to local variables, and it is found that this downscaling method can produce the right level of variability of the local variables and preserve the spatial covariance between local variables (Zorita and Storch, 1999). Midmann et al. (2003) use three different statistical downscaling methods to reconstruct historical wintertime precipitation over Oregon and Washington and conclude that the GCM-simulated precipitation is a good predictor for regional precipitation downscaling. Timm and Diaz (2009) apply a linear statistical downscaling technique to climate projections from the Intergovernmental Panel on Climate Change (IPCC) Fourth Assessment Report to predict climate scenarios onto Hawaiian rainfall for the late twenty-first century, and conclude that, based on a six-model ensemble, the wet season precipitation will decrease 5%-10% and the dry season precipitation will increase 5%, due to the change of wind field.

Among the statistical downscaling methods, a new non-linear classification technique, self-organizing maps (SOMs), is gaining wide use. SOMs were first defined by Kohonen (1989; 1995), and have been proven to be able to extract and visualize the characteristic patterns from multivariate meteorological data (Hewitson and Crane, 2002; Crane and Hewtison, 2003). SOMs are used to investigate the role of the large-scale circulation and atmospheric moisture, as well as the North Atlantic Oscillation (NAO) and the Arctic Oscillation (AO), on extreme winter precipitation in the Balkans, and it is concluded that the artificial neural network based on SOMs can accurately represent synoptic events and dry spells (Cavazos, 2000). Hewitson and Crane (2006) also use an empirical downscaling technique based on SOMs to generate daily

precipitation over South Africa, and show that the downscaled precipitation can capture different characteristics of the observations. Yin et al. (2010) use a statistical downscaling method based on SOMs to simulate the daily precipitation over Southeast Australia, and find that the method displays a high skill in reproducing not only the climatologic statistical properties of the observed precipitation, but also the characteristics of extreme precipitation events. So in this study, we will apply a SOM-based downscaling method to make projections of precipitation in the Mid-Atlantic region and temperature in Central Africa.

Large scale climate variability

Since the basic assumption of downscaling is that the local variable change is a function of the large-scale synoptic circulation, the reliability of the downscaled results highly depends on the ability of GCMs to simulate this circulation. In this study, in order to evaluate the downscaled precipitation changes over the U.S. Mid-Atlantic region and temperature changes over Central Africa, the influences from two large-scale climate modes over the two regions, the El Niño – Southern Oscillation (ENSO) and NAO, will be examined.

ENSO is one of the most dominant climate modes on the interannual time scale in the world. It affects weather, agriculture, societies and ecosystems. Under the influence of global warming, the changes of ENSO amplitude, period and mean state will be critical in predicting future impacts of climate change on the regional scale. GCMs have been widely used to explore the changes of ENSO amplitude, period, pattern, and mean state in the changing climate (Liu et al., 2005; Merryfield et al., 2006; Philip et al., 2006; Yeh et al., 2009).

However, model studies show conflicting results on the changes of ENSO amplitude, period and mean state under the increase of anthropogenic CO_2 (e.g. Knutson et al., 1997; Timmermann et al., 1999; Collins, 2000; Zelle et al., 2005; Meehl et al., 2006). To avoid the

model bias and take advantage of the spread of different models' simulations, the multi-model ensemble is usually used to generate the probabilistic projection of ENSO changes. By analyzing the simulations of 19 models under the Special Report on Emission Scenarios (SRES) A2 scenario, van Oldenborgh et al. (2005) conclude that the six models that resemble the observed ENSO properties show either no change in the mean state or a slight shift towards El Niño-like conditions, with no statistically significant changes in amplitude of ENSO variability in the future. Merryfield (2006) intercompares the response of ENSO variability to CO_2 doubling in a multi-model ensemble, and finds that while most GCMs predict decreases in ENSO period, there are less consistent results on the amplitude and pattern changes. Based on the relation between the equatorial Pacific mean state and seasonal cycle and El Niño characteristics analyzed in 23 GCMs, Guilyardi (2006) concludes that results from models with the highest fidelity of tropical Pacific climatology suggest the likelihood of increased El Niño amplitude, but no clear indications of El Niño frequency change in a warmer climate. Further, many uncertainties associated with ENSO variability and other natural forcing agents, and the complicated relationship among different feedback processes, can also contribute to the difficulty predicting the change in amplitude and frequency of ENSO under global warming (Collins et al., 2010). Therefore, it can be concluded that even applying the multi-model ensemble, there is still no clear indication of future ENSO changes.

The aspect that we are most interested in is the relationships between the ENSO variability and regional precipitation changes over the Mid-Atlantic region, and regional temperature changes over Central Africa. Many studies have shown that there are teleconnetcions between ENSO and local precipitation over many different regions (Ropelewski et al., 1989; Larkin et al., 2005a; Cai et al., 2010). The typical precipitation and temperature patterns over different areas in North America are also demonstrated to have obvious relationships with ENSO events (Ropelewski et al., 1986). Larkin et al. (2005b) compare the

weather anomalies over the U.S. during the conventional El Niño and additional dateline El Niño seasons, and find that the seasonal weather anomalies associated with the dateline El Niño seasons are substantially different from those associated with conventional El Niño seasons. Mo (2010) uses composite analysis to examine the interdecadal impacts on precipitation and temperature over the U.S. from both central Pacific (CPAC) ENSO and eastern Pacific (EPAC) ENSO, and find that the ENSO influence on precipitation over the Southwest was stronger over the recent period, while the impact over the Ohio Valley weakened due to the more frequent occurrence of the CPAC ENSO and can be explained as the linear combination of the impacts of the CPAC and EPAC ENSO events. In a future warmer climate, the ENSO teleconnections in North America surface temperature and precipitation will probably change due to the changes of El Niño event amplitude and mid-latitude base state circulation changes (Meehl and Teng, 2007).

Moreover, many studies show that over Central Africa, besides local temperature variability, ENSO also has a detectable influence on transmission of infectious diseases through temperature and rainfall anomalies, and the forecast system based on this relationship can help predict malaria risk and improve the lead time for malaria warnings (Harvell et al., 2002). Thomson et al. (2006) introduce a system to forecast the probability of anomalously high and low malaria incidence with dynamically ENSO-based, seasonal-timescale, multi-model ensemble predictions of climate, and this forecast system has been successfully applied to the prediction of malaria risk in Botswana, adding up to four months lead time for malaria warnings issued with observed precipitation and having a comparably high level of probabilistic prediction skill.

Another important large-scale climate mode is the NAO, which is a major source of seasonal to interdecadal variability in the worldwide atmospheric circulation (Hurrell, 1995), and describes a large-scale meridional vacillation in atmospheric mass between the North Atlantic regions of the subtropical anticyclone near the Azores and the subpolar low pressure system near Iceland (Wanner et al., 2001). Wallace and Gutzler (1981) use monthly mean sea level pressure

data to identify and describe the NAO as the negative correlation between sea level pressure in the vicinity of the Iceland and south of the Aleutians. Previous studies indicate that the NAO has a strong influence on winter surface temperature, storminess and precipitation over the Northern Atlantic and European regions (Hurrell, 1995, 1996; Deser, 2000; Thompson and Wallace, 2001; Miettinen et al., 2011). Moreover, the NAO affects the ocean through changes in heat content, gyre circulation, mixed layer depth, salinity, high latitude deep water formation and sea ice cover, which are important in documenting and understanding the structure and functioning of marine ecosystems (Hurrell and Deser, 2009). Lin and Derome (1998) find that the winter NAO leads the changes in 500hPa geopotential height over the North Pacific and North American regions by three years. Ghatak et al. (2010) indicate that the high index phase of the NAO generates positive winter air temperature anomalies over eastern parts of North America. Seager et al. (2010) also confirm that a negative NAO index causes positive snow anomalies across eastern North America and in northern Europe.

So in this study, we will firstly examine the influences from ENSO and NAO on the regional precipitation change over the Mid-Atlantic region and temperature change over Central Africa. Then, we will apply these relationships to future simulations to show how the downscaling method can reduce the uncertainties in future regional climate change projections.

The dissertation is organized as follows: Chapter 2 will introduce the procedures of the downscaling method, and validate the precipitation downscaling over the Mid-Atlantic Region of the United States during the historical period. Chapter 3 will address the future precipitation changes over the Mid-Atlantic, and the corresponding inter-GCM uncertainties. Chapter 4 will apply the downscaling method to the temperature changes in Central Africa for both historical and future periods. The downscaled temperature data will be evaluated based on the input requirements of the malaria transmission model, and the influence of ENSO on malaria transmission will also be examined. The total conclusions are given in Chapter 5.

Chapter 2

Probabilistic Projections of Climate Change for the Mid-Atlantic Region of the United States - Validation of Precipitation Downscaling During the Historical Era

Introduction

Recent climate research indicates the likelihood of increasing precipitation extremes in a warmer climate (e.g. Meehl et al, 2007). Indeed, such changes are already apparent as the atmosphere has warmed over the past century (Trenberth et al., 2007; Ning and Qian, 2009). The underlying physics of this overall response is relatively well understood, involving basic factors such as those described by the Claussius-Clapeyron equation, which prescribes increased atmospheric water vapor mixing ratios with warming tropospheric temperatures. There is reason to believe that current generation General Circulation Models (GCMs) provide credible estimates of changes in the hydrological cycle at continental and larger spatial scales (Randall et al., 2007). However, the resolutions of GCMs are usually too coarse to provide detailed regional information about climate change on local scales, and the parameterizations of sub-grid-scale processes, such as precipitation, also results in some degree of uncertainty in the grid-scale projections. Understanding and projecting changes in the distribution of precipitation at regional spatial and short temporal scales most relevant for decision-making and as input into hydrological models, therefore, requires a more nuanced approach (Wagener et al., 2010).

Downscaling has become a popular technique for exploring the relationship between local-scale climate change and synoptic-scale climate forcing (Hewitson and Crane, 1992a; 1992b; Hewitson 1996; 2002; Wood et al., 2002). For example, Hewitson and Crane (1992c) use an artificial neural network-based technique to demonstrate that the local precipitation variability in southern

Mexico resulted from changes in the near-surface and 500 hPa circulation fields. Wilby and Wigley (1997) describe four categories of downscaling techniques: regression methods; weather pattern-based approaches; stochastic weather generators, which belong to statistical downscaling; and limited-area modeling, generally referred to as dynamic downscaling. Downscaling techniques have continued to evolve and their use has matured since the Intergovernmental Panel on Climate Change (IPCC) Third Assessment Report (IPCC, 2001). In the fourth IPCC report, Christensen et al. (2007) evaluate many downscaling methods over different regions of the world, and conclude that downscaling is an effective way to enhance the regional climate details of the GCM-simulated data.

With respect to the Mid-Atlantic and Northeast regions of the United States, Crane and Hewitson (1998) apply artificial neural networks and find that anthropogenic greenhouse gas forcing leads to changes in storm track and humidity fields over eastern North America, which, in an early version of the GISS model, resulted in a substantial increase in spring and summer rainfall. More recent high-resolution projections of future climate change across the northeastern U.S., using IPCC emission scenarios combined with both statistical and dynamical downscaling, suggest temperature increases, especially at higher latitudes and inland, as well as potential precipitation pattern changes (Hayhoe et al., 2007). According to Christensen et al. (2007), annual mean precipitation is very likely to increase in Canada and the northeast USA, and likely to decrease in the southwestern USA. They also indicate that over the mid-Atlantic region, most GCMs agree on increases of annual and winter mean precipitation, while for summer only about half of the GCMs predict increases. Climate change impacts over the mid-Atlantic region identified in these studies are influenced by several key processes, including mid-latitude cyclones, ENSO, and NAO/AO. The Ridge and Valley province of the Appalachian Mountains dominate a large part of Pennsylvania, and statistical downscaling has proven to perform well at

downscaling local temperature and precipitation in similar regions of high topographic variability (Benestad, 2005; Hanssen-Bauer et al, 2005; Hewitson and Crane, 2006).

In many cases it is necessary to propagate climate change projections of meteorological variables, such as precipitation through hydrological models, to yield the variables of interest (e.g. streamflow or soil moisture). Hydrologic models have a much finer resolution than GCMs, and GCMs output generally has to be downscaled before becoming useful for these models. Wood et al. (2004) use three different statistical downscaling methods: linear interpolation, spatial disaggregation, and bias-correction and spatial disaggregation. Each of these methods are applied to both the Parallel Climate Model (PCM) and a Regional Climate Model (RCM), to downscale climate model output to drive the Variable Infiltration Capacity (VIC) model at a 1/8-degree spatial resolution (Liang et al., 1996; Liang et al., 1999). They compared the results from the hydrological model driven by the downscaled data from the three other approaches, and found that the bias-correction and spatial disaggregation (BCSD) methods successfully reproduce the main features of the observed hydrometeorology from the retrospective climate. Maurer (2007) also shows that winter streamflow over California will increase while late spring and summer flow will decrease based on the VIC model driven by downscaled climate change projections from11 GCMs under both the higher emission SRES A2 scenario and lower emission SRES B1 scenario.

Self-organizing maps (SOMs) represent a nonlinear technique that supports the analysis of variability in large, multivariate and multidimensional data sets through the derivation of a spatially organized set of generalized patterns of variability from the data (Reusch et al., 2007). Cavazos (1999) uses SOMs to examine the relationships between large-scale circulation-humidity fields and local daily precipitation events in northeastern Mexico and southeastern Texas. SOMs are applied to combine the precipitation records of individual stations into a regional data set by Crane and Hewitson (2003). Hewitson and Crane (2006) use SOMs to downscale synoptically

controlled daily precipitation over South Africa, while Reusch and Alley (2007) find that SOM-based patterns concisely capture the spatial and temporal variability in monthly Antarctic sea-ice edge position data through the examination of area anomalies of Antarctic sea-ice coverage.

In this chapter, we use the SOM-based downscaling methodology introduced by Hewitson and Crane (2006) to reproduce historical daily precipitation observations for stations over Pennsylvania (USA). We evaluate how well GCMs reproduce the observed synoptic-scale atmospheric conditions and assess their usefulness in projecting current precipitation variability over the region.

Data and Methodology

Data

In this study, we use three sets of data for the downscaling procedure: NCEP reanalysis of daily gridded atmospheric data, observed daily station precipitation data, and GCM daily gridded atmospheric data. The daily gridded atmospheric data are constructed from six-hourly National Center for Environmental Prediction (NCEP) reanalysis data from 1979 to 2007 with a resolution of 2.5°×2.5°.

The SOM procedure uses seven variables: *u*- and *v*- components of the wind at 10 m and 700 hPa, relative humidity at 850 hPa, air temperature anomaly at 2 m, and the lapse rate of temperature from 850 hPa to 500 hPa. All seven variables are physically related to the local precipitation. The *u*- and *v*- components of the wind determine low level convergence and divergence, while water vapor content of the lower atmosphere relates to relative humidity and surface temperature. The 850 hPa to 500 hPa lapse rate determines whether the initial conditions for convection are met.

Detailed comparisons (Hewitson, pers. comm.) of the present SOM-based statistical downscaling to the application of climate regimes in Africa have shown that the additional use of specific humidity makes little difference to predictions of rainfall during the historical period but leads to predictions of greater increases in rainfall in response to future anthropogenic warming. Comparisons with dynamically downscaled estimates based on regional climate models suggest that these larger precipitation increases represent overestimates. The effects of using the additional humidity parameter will be discussed later in the context of our own downscaling results.

We limit our analysis to the post-1979 NCEP data when satellite observations improve the quality and climatological continuity of the product (Sturaro, 2003; Tennant, 2004). The precipitation data for Pennsylvania come from 17 stations for the period 1961 to 2005. The names, locations, and elevations of the stations are given in Table 2-1 and shown in Fig. 2-1. The GCM circulation data from 1961 to 2000 are taken from the 20th century simulation using historical greenhouse gas concentrations ('20c3m scenario') of the World Climate Research Programme (WCRP) Couple Model Intercomparison Project phase 3 (CMIP3), for nine different models: CCCMA_CGCM3_1, CNRM_CM3, CSIRO_MK3_0, GFDL_CM2_0, GISS_MODEL_E_R, IPSL_CM4, MIUB_ECHO_G, MPI_ECHAM5, and MRI_CGCM2_3_2A. The data and descriptions of the GCMs can be found at the WCRP CMIP3 Multi-Model Data website[1]. The variables simulated by the GCM data are the same as those for the NCEP data. In the assessment of the downscaled product, we also use daily NCEP sea level pressure from 1979 to 2007, and the precipitation rate of the nine GCMs from 1961-2000.

[1] https://esg.llnl.gov:8443/index.jsp

The Downscaling Procedure

The first step in the downscaling procedure used here involves training the SOMs. SOMs are analogous to a fuzzy-clustering algorithm, and are usually used to visualize and characterize multivariate data distributions (Kohonen, 1989; 1995). A SOM is typically depicted as a two-dimensional array of nodes, where each node is described by a vector representing the average of the surrounding points in the original data space. For an input data set that is described by a matrix of n variable data points and m observations, each node in the SOM is described by a reference vector having length n. The initial step in the SOM training involves assigning random values to each node reference vector, and then comparing the data record with each node vector. The reference vector that most closely matches the data vector is defined as the "winning" node. Then the reference vector of the winning node is updated slightly toward the direction of the input data by a factor termed the "learning rate". All the surrounding nodes are also updated in the direction of the input data by a smaller learning rate. The entire process is then repeated for multiple iterations until the differences between iterations are smaller than a selected threshold value. This training procedure is described in detail in Crane and Hewitson (2003) and illustrated in Figure 1 therein.

In our application, a separate SOM with 11×9=99 nodes is trained for each station, each node representing a characteristic atmospheric state. The choice of SOM size is ultimately subjective—fewer nodes increases generalization, while an increased number of nodes results in too few days being mapped to each node to derive a representative rainfall distribution function. However, statistical validation experiments, as described later, can be used to assess the sensitivity of the results to this precise choice.

Prior to the training step, the study area was divided into a grid with a resolution of 0.5 degrees (Fig. 2-2a), and for any given target station, the nearest cell is identified (Fig. 2-2b). For example,

the grid cell centered on 40.0°N, 76.5°W is the nearest cell for Harrisburg (40.22°N, 76.85°W). For each of the seven variables, nineteen hexagonal are created with the grid cell being in the center. For each hexagonal grid, four NCEP data points surrounding each of six triangular centroids are extracted and regridded to the centroid through a weight inversely proportional to the distance between the NCEP data point and the hexagonal centroid. The value over each of 19 hexagonal grids is then calculated through averaging the values of six triangular centroids (Fig. 2-2c). Finally, all the NCEP data are separately standardized. Thus, for each node, we use seven variables, creating a 19×7-member vector to describe each day's atmospheric state around the station.

For each station, we compare the observed daily atmospheric data to the SOM nodes and map each day to one particular node. For each SOM node, we take all the days that map to that particular node and then rank the precipitation on those days from low to high. A spline is fit to the ranked precipitation data to define a continuous Cumulative Distribution Function (CDF) of the node's rainfall. This procedure is repeated for all the nodes in the SOM and then for all stations.

To downscale the precipitation for a given station over a particular period, we first compare the circulation data (either from the GCMs or from the observations), to the SOM, associating each day with a node. For each day, a random number generator is used to select a value of precipitation from the CDF for the node to which the day is mapped. The procedure is repeated many times to produce an ensemble of time series for each station, any one of which can be considered a representative sample of the distribution characterizing the downscaled data set. We chose to produce ensembles consisting of 1500 realizations for the purpose of our downscaling applications.

Results

There are a large number of empirical downscaling methodologies currently being applied to regional climate data sets. However, many simply describe the application of a technique to a single region using one or maybe two GCMs to drive the downscaling and comparing the results to observed monthly rainfall. Here we attempt to go further by downscaling all available GCMs from the CMIP-3 archive that have the required daily parameters. Furthermore, we focus on validation using a variety of measures to achieve a more robust downscaling that also reflects the uncertainty resulting from the variations in the original GCM simulations.

Synoptic controls on precipitation

The basic assumptions behind our downscaling approach are: (i) precipitation at each of the stations will vary as a function of the atmospheric state, (ii) the NCEP variables can adequately describe that state, and (iii) they are to some degree a function of the larger scale atmospheric state. One appropriate diagnostic of that state is the sea level pressure (SLP) field. This motivates, as an internal consistency check on the validity of our underlying assumptions, assessing how well the nodes of the trained SOM reflect differences in the synoptic state of the atmosphere as indicated by their projection onto the SLP field—a field that was not used to define (train) the SOM.

The projection of the 99 SOM nodes on to the SLP field for the Harrisburg (40.0°N and 76.5°W) site is shown in Fig. 2-3. This site is chosen because of its central location, but results are similar for all sites. Each projection of a given node is defined by the average of the SLP field over all days mapped to that node. The figure demonstrates that, although the SLP data are not directly used in training the SOM, the SLP distributions are clearly well differentiated by the SOM

nodes: similar patterns locate close to each other in the SOM space, while different patterns locate further apart. High pressure dominates the nodes to the top and left of the SOM space, while low pressure dominates in the bottom right with transitional nodes in between.

GCM validation

A basic method for evaluating a particular GCM's usefulness in assessing climate change is to test the model's ability to simulate present climate (including variability and extremes). The differences between simulations and observations should be considered insignificant if they are within unpredictable internal variability, expected differences in forcing, or uncertainties in the observed fields (Randall et al., 2007). In the present case, we can compare the simulations to observations (NCEP) by mapping the GCM fields to the trained SOM and comparing the results with the NCEP mapping, providing the means for assessing how well the various GCMs reproduce the atmospheric states used to differentiate characteristic rainfall distributions.

As an example, we still consider the Harrisburg (40.0°N and 76.5°W) site (Fig. 2-4). In Fig. 2-4, each square represents one node in the SOM. The frequency of a node is equal to the number of the days mapped to this node as a percentage of the number of all the days used in the SOM training. Fig. 2-4a shows the frequency of days mapped to each of the 99 SOM nodes for the NCEP data for the period 1979-2007, while Fig. 2-4b-f shows the mapping of five GCMs for the period 1961-2000: CNRM, CSIRO3.0, GFDL, IPSL and MRI. These five models span the range of quantization errors (discussed below) encountered among the full set of GCMs analyzed. Mapping the GCM data on the SOM trained by the NCEP data shows how well the GCMs reproduce the atmospheric states used to differentiate characteristic rainfall distributions.

The NCEP frequency distribution (Fig. 2-4a) shows that the frequencies are fairly uniformly distributed across all the nodes with slightly larger frequencies located at the edges and corners.

The GCMs also show a fairly uniform distribution across all nodes, although several of the models show centers of higher frequencies that are not present in the NCEP distributions. CSIRO3.0 and IPSL in particular, the two models with the largest quantization errors, show a concentration of variance in fewer nodes. These centers of higher frequencies in some of the GCM mappings suggest slightly reduced variance in the model fields, but the distribution across nodes shows that the models do recreate the atmospheric states revealed in the NCEP data, indicating that the GCMs produce realistic synoptic-scale patterns and variability across the region.

The average quantization errors (Fig. 2-5), measure how well the NCEP or five GCMs circulation fields map onto the available nodes. The quantization error is the mean difference between the node vector and each of the days that map to the node. It shows how closely the days are clustered in the data space or, alternatively, how much of the data space is represented by that node. By analogy with cluster analysis, the quantization error represents the within-group variability. The quantization error of one day is defined as the smallest Euclidean distance between the input vector and its best-matching node when mapping that day to one of the SOM nodes, and it is the measure of how the node reference vector represents the mapped atmospheric vector. Fig. 2-4a shows that the quantization errors over the left side of the SOM are larger than those over the center and right side, indicating that the variances are larger for the synoptic states dominated by high-pressure systems (Fig. 2-3).

The average quantization error distributions of the GCMs (Fig. 2-5b-f) are very similar to the corresponding distribution for the NCEP fields, although with slightly higher error values in some cases. The blank node (7, 8) in the distribution of model CSIRO3.0 (Fig. 2-5c) indicates that no single day maps to that node. This observation suggests that while the GCMs may have reduced dimensionality compared to the observed data, there is, in some cases, greater variability within the synoptic states mapped to each node.

Recall that in the training of the SOM, each daily synoptic circulation state is treated as a location in the original multi-dimensional state space, and that similar circulation states locate close to each other, while those states with large differences locate further apart. Combining Figs. 3 and 4, it can be concluded that the total volume in state space of the NCEP data is larger than the volume of the GCMs' state spaces, but around separate characteristic synoptic atmospheric states, the distance among the daily synoptic states in each of the GCMs is usually larger than the distance in NCEP state space.

The average values and standard deviations of the averaged quantization errors through NCEP and nine GCMs are given in Fig. 2-6. The pattern of average values of the averaged quantization errors is similar to the pattern of averaged quantization errors seen with the NCEP data, with larger errors over the left hand side of the SOM and smaller errors over the right hand side (Fig. 2-6a). The additional four GCMs not shown in Fig.4 thus have similar quantization error distributions to the five GCMs that are shown. It can be concluded that the distribution of variance of the synoptic circulation patterns in the GCMs are broadly similar to those for the NCEP data. The standard deviations of the mean quantization errors (Fig. 2-6b) show that the variability is almost uniform over all the nodes. The average of all GCMs gives a close match to the observations (NCEP). This was also demonstrated for the Pennsylvania region by Shortle et al. (2010), who show that the present-day mean temperature and rainfall simulations for all GCMs in the CMIP3 archive provide a closer match to the observations than any individual model.

As a simple measure of GCM performance in reproducing the observed atmospheric states, we average all the mean quantization errors over the 99 nodes individually for the NCEP data and for each of the GCMs (Fig. 2-7). The average error for the NCEP data is about 7, and the average errors from most of the GCMs are also close to 7, with slightly larger errors from models CSIRO3.0, and IPSL. This suggests that, overall, these two models are slightly less accurate in

reproducing the observed distribution of synoptic-scale atmospheric states compared to the other seven models. Although it does not necessarily follow that the accuracy with which a particular GCM is able to simulate the present climate translates directly into its ability to project the future, using the inverse difference between the GCM and the NCEP quantization errors would be one possible approach to weighting the GCM output when looking at projected changes for future climates over the region based on a multi-model ensemble (e.g. the CMIP3 future climate change projections).

The downscaled precipitation

Fig. 2-8 shows the calculated cumulative distribution functions (CDFs) of daily precipitation values corresponding to the 99 SOM nodes. For the nodes located in regions of the SOM dominated by high surface pressure, most of the CDFs show low or zero precipitation amounts. As would be expected, for nodes located in regions of the SOM dominated by low surface pressure and certain transitional surface pressure patterns, precipitation amounts are much higher. The differences in the CDFs across the SOM indicate that the SOM categorization of atmospheric conditions does allow for substantial differentiation between different precipitation states, and that these differences make physical sense in the context of the synoptic-scale circulation.

The previous discussion clearly demonstrates that the SOM characterization of atmospheric states captures the synoptic variability, that the different atmospheric states (represented by the SOM nodes) have different precipitation characteristics, and that the GCMs exhibit the same atmospheric states and synoptic variability. The final step in the validation procedure is to examine whether the trained SOM can be used to generate realistic precipitation time series that have the same magnitude and frequency characteristics as the observed data.

The SOM approach to downscaling precipitation acknowledges that similar atmospheric conditions can result in different observed precipitation amounts. By randomly selecting from the rainfall CDF for each node, the approach captures some of this stochastic variability. Because the downscaling is a simplification of reality, and because of its stochastic element, any individual recreation of the precipitation represents only one possible realization of the precipitation regime that should match in its fundamental statistical attributes, the observed precipitation, while not necessarily matching the observed time series on a day-to-day basis. To be a valid and useful representation of actual precipitation, downscaling needs to match the characteristics needed for e.g. hydrologic modeling—that is, the downscaled precipitation should exhibit the same monthly and seasonal precipitation amounts, the same day-to-day variability, and the same number of rain days per month.

In some respects, validation is simply a matter of examining these characteristic statistics and assessing whether the results are good enough for a particular application. "Good enough," of course, is a subjective decision, which depends on the particular application. In this case, and to demonstrate that the downscaling may have broad application, we also ask: Does the downscaling give a better result than just using climatology? And, is the downscaling a significant improvement over using the nearest GCM grid cell data? We seek to demonstrate that the downscaled data are a close match to the observations, and that the downscaling gives an appreciable improvement over using the GCM precipitation field directly.

The first step in validating statistical downscaling is to compare the statistical properties of the downscaled time series generated by the reanalysis fields with those of the corresponding observations. Fig. 2-9 compares the probability distributions of the observed daily precipitation and the downscaled daily precipitation from one random iteration generated by the NCEP data over 17 stations for the period 1979-2005. In the calculation, only the days on which both observed and downscaled precipitation data are available are counted [note that only

precipitation events larger than 0.25 mm (0.01 inch) are considered, consistent with the threshold for defining a "rain day" used in past work—e.g. Fitzpatrick et al., 1967; Hershfield, 1971; Gallus et al., 2004]. The precipitation interval used in the calculation is 1 mm, and the probabilities of extreme precipitation larger than 50 mm are considered together. From Fig. 2-9 it can be concluded that, although there are some differences between the downscaled and observed probabilities of daily precipitation in the range from 0.25-1 mm, the downscaling reproduces the probability distributions extremely well. Moreover, the observed and downscaled probabilities of the largest precipitation events—with daily precipitation greater than 50 mm—are very close, which means that the downscaling, importantly, is also effective in capturing the extreme precipitation events for each station.

Visually, we can see that the downscaling captures the temporal variability of the actual observations (Fig. 2-10). While we generate many (1500) realizations of the downscaled precipitation to construct our ensemble, it is extremely unlikely that we will happen to reproduce the unique sequence of daily precipitation events that characterizes the actual observations. Nonetheless, it is instructive to see if we can find members of our ensemble that not only capture the overall statistical character of the observations, but also happen to approximate well the observed sequence of monthly precipitation anomalies. Fig. 2-10 shows the observed and downscaled monthly precipitation amount time series for three stations with the largest correlation coefficients between the observed and downscaled monthly precipitation: Allentown (a), Harrisburg (b), and Towanda (c).

As one important measure of statistical skill, we evaluate whether the mean downscaled precipitation estimates using the NCEP data (rain days only) are on average closer to the observations than the climatological mean for that season (Table 2-2). Ratios less than unity indicate nominally better skill than the null "no skill" prediction of climatological mean values. We used a remove-one-sample-at-a-time jackknife procedure (Efron, 1982) to provide non-

parametric confidence intervals in the mean skill over all 17 stations. If the associated upper 95% confidence limit remains below unity, we conclude that the downscaling procedure yields a statistically significant improvement above the climatological no-skill baseline. The ratios for each season (and annual mean), are in fact observed to be significantly below unity indicating, as we would hope, that the downscaling does perform better than simply invoking climatology. Among the four seasons, the least improvement occurs in summer, reflecting the fact that much of the summer precipitation is convective. In this case there is more of a stochastic element and less dependence on the synoptic circulation.

Continuing the process of skill evaluation, we would expect that if the downscaling is providing large-scale information that usefully informs the local distribution of precipitation, drawing from the precipitation CDFs for the appropriate SOM node should yield a narrower distribution than drawing simply from the climatological daily rainfall distribution for the appropriate season. In other words, accounting for the synoptic atmospheric state ought to provide some additional discrimination beyond a random draw from the climatological seasonal distribution. We define the width of the respective PDFs by the interquartile range (i.e. difference between the 75th and 25th percentiles of the distributions). Table 2-3 tabulates a skill metric defined as the ratio of the mean squared width of the PDFs constructed from the ensemble of 1500 downscaled precipitation values and the observed climatological distribution. In this analysis, in order to get the more precise PDFs with larger amounts of samples, we use a different rainy day definition as larger than 0 mm. A ratio below unity indicates that the downscaled values are drawn from a narrower PDF than would be the case for the corresponding climatological distributions, and is therefore suggestive that conditioning on the large-scale atmospheric state via the downscaling procedure provides some additional predictive skill beyond climatology. We once again use a jackknife procedure to estimate confidence intervals and evaluate statistical significance. Apart from a number of the stations in spring

(February/March/April), the ratios remain significantly below unity. The possible reason for the exception with the spring season results is that a large number of spring rain days are governed by synoptic circulation patterns with CDFs that have wide daily precipitation ranges.

We next compared the observed and NCEP-downscaled precipitation fields with respect to a several key measures: mean monthly precipitation, average monthly numbers of rain days, and standard deviations of monthly mean precipitation (Table 2-4). The comparison was performed over the 17 stations for the period 1979-2005. For the forgoing discussion, we make use of a randomly selected, representative realization from the ensemble of 1500 downscaling surrogates, though similar results are obtained for any realization. The observed average monthly precipitation amounts vary from roughly 80 to 110 mm among the different sites, with an average of 98.8 mm. The downscaling slightly underestimates the mean precipitation at 95.4 mm. This underestimation bias is statistically significant according to the jackknife error estimates, and appears to result from the fact that the downscaling underestimates the magnitude of the most intense daily precipitation events (larger than 50 mm). The observed and downscaled average monthly rain days are very close for all stations with an identical average over all stations of 10.9 days for both downscaled and observed. The observed and downscaled standard deviations of monthly precipitation totals are also similar, with the 95% confidence intervals overlapping (albeit only just so), indicating that the downscaling procedure is able to reproduce the observed variability.

Having validated the downscaling procedure for the late 20th century observations, we then turned to the GCM simulations. We compared the same characteristics of the precipitation field for the downscaled and raw GCM precipitation data over the full data record 1961-2000. Results were analyzed both by GCM (Table 2-5), averaging of the 17 stations, and by station (Table 2-6), averaging over GCMs. Errors relative to observations for both downscaled and raw GCM precipitation values are compared in Tables 2-7 and 2-8 respectively. Uncertainties in

averages across models are determined based on jackknifing with respect to model, while uncertainties in averages across stations are determined by jackknifing with respect to station.

These comparisons yield a number of important insights. First of all, the downscaled results are clearly closer to observations than the raw GCM results for nearly all models and all stations. This finding is also true for averages over stations and averages over the models. Extremely large errors are found with the raw precipitation field for individual GCMs with respect to e.g. mean monthly precipitation (see Tables 2-5 and 2-7). Interestingly however, because these errors are often of opposite sign in different models--i.e. either considerably below or above the observed value—they tend to cancel. Averages over GCMs are consequently considerably closer to observations than individual GCMs. This finding is consistent with the widely reported finding (e.g. Meehl et al, 2007) that averages over multi-model ensembles often provide more faithful estimates than individual models, presumably because of the cancellation of errors specific to models. In this particular case, the errors in question likely involve the differing convective parameterization schemes used to estimate precipitation in the various models.

While the downscaled model precipitation field closer in nearly all characteristics to observations than the models' raw precipitation field, it is worth noting that statistically significant biases nonetheless remain in the downscaled model estimates. Mean monthly rainfall totals are, as they were for the late 20th century observations (Table 2-5), biased slightly high (the mean monthly downscaled precipitation over all models and stations is 103.47 mm, while the observed value is 96.87 mm). Rain day numbers are also biased slightly at 11.42 days per month averaged over all models and stations, vs. the observed value of 10.89 days per month—the difference is small, but statistically significant. The monthly standard deviation of the downscaled precipitation field is 53.85 mm averaged over stations and GCMS while it is 48.58 for the observations—a difference that is once again statistically significant, and which suggests that the downscaled GCM precipitation is slightly more variable in time than the observations.

While some of the differences between the downscaled GCM values are the results of model bias and differences in the simulated atmospheric states. The similarity of the downscaled data, however, suggests that a large portion of the GCM differences is likely due to differences in precipitation parameterization schemes.

That such biases remain in the downscaled estimates is hardly surprising, as there are clearly systematic biases in the various fields of the model (temperature, winds, lapse rates, etc.) from which the downscaled precipitation estimates are derived, and not even downscaling methods can cure these ills. However, there is far greater consistency among the downscaled model estimates with respect to all diagnostics (monthly mean precipitation, rain days, and monthly standard deviation) than in the raw model precipitation values. The downscaling procedure appears to provide a more reliable determination of whether or not precipitation is likely, and when it is likely, how much an event will produce. These observations reinforce previous findings (e.g. Hewitson and Crane, 2006) that bypassing the convective parameterization schemes in the models yields precipitation estimates that are in all key attributes more consistent among models, closer to observations, and likely more robust with respect to *future projections*—an issue we will discuss further below.

Looking more loosely at the computed relative errors (Tables 2-7 and 2-8) we obtain some additional important insights. We see for example that the ability of the downscaled precipitation fields to reproduced observed characteristics at our sites is highly model-dependent (Table 2-7). Several models—CCCMA, CSIRO3.0 and MPI to be specific---are able to reproduce observed monthly means rainfall totals with less than 5% error relative to observations. These same models reproduce the observed frequency of rain days with under 6% relative error, and the monthly standard deviation with under 11% relative error. By contrast, relative errors remain high even for the downscaled estimates (though considerably less so than for the raw model precipitation) for certain models, specifically GISS (error is nearly 20% for mean precipitation, roughly 12% for

frequency of rain days, and roughly 24% for the standard deviation). Looking at the breakdown of error by site (Table 2-8), we see that certain sites (e.g. Stroudsburg and West Chester) show particularly large errors in mean monthly precipitation (11-13%) and monthly standard deviation (18-26%) (Errors remain small for the number of rain days). These are among the few wettest sites in our network, and they also produce among the largest discrepancies for both mean precipitation and monthly standard deviation in the downscaling of modern (NCEP) observations (Table 2-4). It is reasonable to speculate that the larger biases we see in the downscaled simulations in these locations may relate as much to the intrinsic biases in the application of downscaling at these sites to any features specific to the model simulations themselves.

Finally, we return to the issue of the potential sensitivity of the downscaling procedure to the precise variables used in training the SOM. As we discussed earlier, future projections of precipitation based on statistical downscaling methods show some sensitivity to which humidity variables are used. Previous work in Africa for example, indicates that use of specific humidity can lead to projections of large future increases in mean precipitation. Comparisons with parallel dynamical downscaling results suggest that these larger projections are unrealistic (Hewitson, pers. comm.). A plausible explanation is that the exponential dependence of specific humidity on temperature leads to a large potential extrapolation error when projecting future precipitation changes in a warmer atmosphere based on training over an historical interval for which there are no analog states for characterizing future atmospheric temperature. Arguably, the use of relative humidity as a training variable avoids this problem.

Nonetheless, one might view this sensitivity to the humidity variables used as a reasonable measure of a key structural uncertainty in projecting future precipitation changes. In this spirit, we have performed the same analyses as described earlier but where specific humidity has been added as an additional large-scale predictive variable in training the SOM. This alternative procedure yields remarkably similar results, including very similar relative errors. Thus, it is not

possible from the skill assessments presented in this study to objectively favor one choice of humidity variables over the other. In additional work involving the downscaling of future climate change projections we intend to use the sensitivity of projections to this choice as a measure of structural uncertainty in projecting regional changes in precipitation characteristics.

Since our downscaled results are generated as the input of hydrological models, we also need to assess the downscaling performance based on the concerns of hydrological studies. So we choose additional nine verification metrics important in hydrological studies: maximum dry spell per month, maximum and minimum daily precipitation per month, number of rainy days with daily precipitation larger than 5 mm, 10mm, and 15 mm, annual total precipitation, standard deviation of annual precipitation, and minimum consecutive three year total precipitation. For here, we show the results of the maximum dry spell per month (Fig. 2-11), monthly number of days with precipitation larger than 10 mm (Fig. 2-12), and minimum consecutive three year total precipitation (Fig. 2-13).

Fig. 2-11 shows the relative bias of downscaled monthly maximum dry spell from NCEP and nine GCMs. It can be concluded that all the downscaled results from NCEP and GCMs underestimates the metrics a little bit, with an average close to zero and total ranges within -0.1 to 0. For the monthly number of days with precipitation larger than 10 mm (Fig. 2-12), the downscaling usually overestimates it with larger standard deviations. For the minimum consecutive three year total precipitation (Fig. 2-13), the downscaling can reproduce this metric reasonably with averages close to zero and small standard deviations. The small magnitudes of these relative biases indicate that the downscaled results have the potential ability to drive the hydrological models to reproduce the runoff characteristics, such as drought and water availability, on different time scales.

Conclusions

Using a specific application—reproducing historical precipitation characteristics in Pennsylvania—we demonstrated how statistical downscaling using Self Organization Maps (SOMs) to condition local precipitation estimates on large-scale atmospheric states, can yield improved representations of precipitation characteristics. Using a variety of skill metrics and internal consistency tests, we showed that the downscaling procedure applied to modern (NCEP) atmospheric observations realistically reproduces observed daily precipitation characteristics at a network of sites throughout Pennsylvania.

Next we demonstrated that application of the same SOM procedure to a suite of nine simulations from the CMIP3 multi-model historical simulation archive yields local precipitation estimates form the model simulations which agree better with both each other, and with historical observations, than the raw GCM precipitation field. While the downscaling procedure does not entirely eliminate biases in the modeled local precipitation statistics, it does reduce these biases considerably, and it does provide greater consistency between the models, suggesting that bypassing the individual model's own varying precipitation parameterization schemes can yield more robust estimates of the distribution of local precipitation from the models.

Then, we found that similarly skillful precipitation statistics could be obtained using either of two alternative representations of humidity information in training the SOM, one in which only relative humidity is used, another in which both relative and specific humidity are used. Given that one cannot objectively distinguish, on the basis of validation against historical data alone, which of these two schemes is preferable, it is advisable to consider the sensitivity to this choice as one measure of structural error in examining downscaling results applied to future climate change projections, where the two schemes may give somewhat different results.

Finally, the relative biases of nine metrics important in the hydrological studies are calculated, and the small magnitudes of the relative biases indicate that the downscaled results are capable as the input of hydrological models to reproduce the observed runoff characters.

Table 2-1. The locations and elevations of the 18 stations over Pennsylvania.

Station ID	Station name	Latitude (°N)	Longitude (°W)	Elevation (m)
360106	Allentown	40.66	-75.44	118
363054	Chambersburg	39.94	-77.64	195
363028	Franklin	41.39	-79.82	302
363526	Greenville	41.42	-80.37	344
363699	Harrisburg	40.22	-76.85	103
364385	Johnstown	40.34	-78.92	370
365915	Montrose	41.84	-75.87	475
366233	New Castle	41.02	-80.37	251
366689	Palmerton	40.80	-75.62	125
367477	Ridgway	41.42	-78.75	414
368449	State College	40.80	-77.87	357
368596	Stroudsburg	41.01	-75.19	146
368905	Towanda	41.76	-76.42	229
369050	Uniontown	39.92	-79.72	291
369298	Warren	41.86	-79.16	369
369464	West Chester	39.97	-74.64	137
369933	York	39.92	-76.75	119

Table 2-2. Ratio of mean square errors (MSEs) [relative to the observed daily precipitation values] using mean downscaled estimates and climatological mean values.

Station	Spring	Summer	Autumn	Winter	Annual
Allentown	0.72	0.90	0.77	0.70	0.91
Chambersburg	0.77	0.87	0.78	0.72	0.73
Franklin	0.82	0.88	0.83	0.79	0.68
Greenville	0.82	0.85	0.82	0.81	0.76
Harrisburg	0.75	0.91	0.76	0.71	0.82
Johnstown	0.79	0.88	0.81	0.84	0.80
Montrose	0.75	0.86	0.78	0.81	0.87
New Castle	0.83	0.88	0.86	0.80	0.66
Palmerton	0.78	0.89	0.78	0.70	0.71
Ridgway	0.81	0.86	0.81	0.79	0.75
State College	0.85	0.86	0.81	0.80	0.70
Stroudsburg	0.70	0.86	0.73	0.70	0.92
Towanda	0.81	0.87	0.81	0.81	0.67
Uniontown	0.83	0.88	0.78	0.84	0.82
Warren	0.80	0.85	0.81	0.80	0.79
West Chester	0.77	0.85	0.80	0.78	0.80
York	0.71	0.87	0.74	0.72	0.84
Average	0.78	0.87	0.79	0.77	0.78
95% CI	(0.780,0.788)	(0.870,0.873)	(0.791,0.796)	(0.769,0.776)	(0.768,0.783)

Table 2-3. The ratio of widths (as defined by interquartile range) of downscaled NCEP vs. observed climatological precipitation distribution (days with non-zero precipitation only).

Station	Spring	Summer	Autumn	Winter	Annual
Allentown	1.35	0.46	0.89	0.80	0.91
Chambersburg	1.00	0.38	0.79	0.58	0.73
Franklin	0.77	0.41	0.66	0.67	0.68
Greenville	1.08	0.44	0.76	0.76	0.76
Harrisburg	1.07	0.29	0.79	0.79	0.82
Johnstown	0.91	0.51	0.87	0.94	0.80
Montrose	1.02	0.57	0.82	0.82	0.87
New Castle	0.89	0.37	0.75	0.67	0.66
Palmerton	1.12	0.31	0.74	0.61	0.71
Ridgway	0.85	0.53	0.69	0.73	0.75
State College	0.82	0.40	0.76	0.63	0.70
Stroudsburg	1.50	0.59	0.90	0.68	0.92
Towanda	0.97	0.42	0.67	0.53	0.67
Uniontown	1.10	0.47	0.77	0.72	0.82
Warren	0.92	0.50	0.75	0.95	0.79
West Chester	1.14	0.60	0.71	0.53	0.80
York	1.02	0.58	0.99	0.63	0.84
Average	1.03	0.46	0.78	0.71	0.78
95% CI	(1.012,1.045)	(0.452,0.470)	(0.776,0.791)	(0.692,0.718)	(0.768,0.783)

Table 2-4. The comparisons between observed and NCEP-downscaled average monthly precipitation amounts (mm), average monthly numbers of rainy days (day), and standard deviations of monthly precipitation (mm) over the 17 stations during the period 1979-2005.

Station ID	OA[a]	DA[b]	ON[c]	DN[d]	OSD[e]	DSD[f]
Allentown	101.49	96.73	9.61	9.69	55.96	57.75
Chambersburg	93.78	87.08	9.37	9.13	49.47	46.27
Franklin	103.76	101.82	11.87	12.23	46.93	48.75
Greenville	98.03	94.34	12.38	12.31	44.27	42.31
Harrisburg	90.63	87.51	9.77	9.67	50.57	46.81
Johnstown	105.91	103.28	12.71	12.71	50.92	48.01
Montrose	110.56	106.65	12.36	12.67	53.58	52.62
New Castle	86.09	84.72	10.88	11.02	44.16	45.62
Palmerton	91.99	87.79	8.02	8.19	55.10	56.36
Ridgway	101.91	98.97	12.40	12.23	44.81	44.51
State College	94.72	91.59	10.99	11.03	49.73	47.02
Stroudsburg	113.49	108.23	10.36	10.29	62.49	58.95
Towanda	80.26	79.11	9.78	9.69	43.58	43.78
Uniontown	97.52	95.38	11.80	11.91	44.97	43.74
Warren	107.59	105.34	13.37	13.26	44.35	45.75
West Chester	106.37	100.52	9.50	9.41	59.03	54.68
York	95.57	92.59	9.74	9.69	51.79	49.86
Average	98.80	95.39	10.88	10.89	50.10	48.99
95% CI	(98.07, 99.60)	(94.69, 96.06)	(10.72, 11.06)	(10.78, 11.06)	(49.33, 50.47)	(48.44, 49.40)

a. OA is observed average monthly precipitation amounts (mm).

b. DA is downscaled average monthly precipitation amounts (mm).

c. ON is observed average monthly number of rainy days (day).

d. DN is downscaled average monthly number of rainy days (day).

e. OSD is observed standard deviation of monthly precipitation amounts (mm).

f. DSD is downscaled standard deviation of monthly precipitation amounts (mm).

Table 2-5. Comparisons of average monthly precipitation amount (mm), average monthly numbers of rainy days (day), and standard deviations of monthly precipitation amount (mm) for observed, downscaled GCM, and raw GCM precipitation for all nine GCMs, averaged over stations (period 1961-2000, all months).

GCM names	DA[a]	DN[b]	DSD[c]	SA[d]	SN[e]	SSD[f]
Observation	96.87	10.89	48.58	96.87	10.89	48.58
95% CI[g]	(96.09, 97.68)	(10.77, 11.00)	(48.15, 49.14)	(96.09, 97.68)	(10.77, 11.00)	(48.15, 49.14)
CCCMA	98.07	11.12	50.95	90.89	21.64	36.08
95% CI[g]	(97.08, 98.93)	(10.98, 11.22)	(50.14, 51.56)	(90.28, 91.55)	(21.59, 21.72)	(35.80, 36.48)
CNRM	106.06	11.52	55.93	105.17	21.22	55.84
95% CI[g]	(104.87, 107.16)	(11.39, 11.63)	(54.97, 56.71)	(104.88, 106.74)	(21.12, 21.29)	(55.68, 57.04)
CSIRO3.0	99.06	11.50	52.94	78.71	18.09	32.29
95% CI[g]	(98.05, 99.94)	(11.36, 11.64)	(51.51, 53.48)	(78.30, 79.19)	(17.78, 18.44)	(31.97, 32.63)
GFDL	103.66	11.50	52.31	99.92	19.15	41.07
95% CI[g]	(102.70, 104.57)	(11.37, 11.61)	(51.04, 52.72)	(99.51, 100.18)	(19.01, 19.34)	(40.84, 41.18)
GISS	115.69	12.17	60.22	52.86	15.75	40.33
95% CI[g]	(114.18, 116.93)	(12.05, 12.28)	(58.94, 61.19)	(52.35, 53.17)	(15.73, 15.77)	(39.82, 40.64)
IPSL	101.30	11.28	55.01	120.35	19.23	50.17

95% CI[g]	(100.13, 102.24)	(11.16, 11.40)	(53.55, 55.52)	(119.45, 121.18)	(19.18, 19.32)	(49.80, 50.62)
MIUB	104.40	11.19	53.55	95.68	22.21	37.68
95% CI[g]	(103.68, 105.56)	(11.06, 11.29)	(52.76, 54.13)	(95.22, 96.09)	(22.17, 22.27)	(37.37, 37.99)
MPI	100.11	11.21	52.14	106.12	15.43	51.93
95% CI[g]	(99.30, 100.99)	(11.09, 11.32)	(51.45, 52.59)	(105.40, 106.63)	(15.28, 15.61)	(51.81, 52.11)
MRI	102.89	11.26	51.63	72.32	15.16	34.01
95% CI[g]	(102.16, 104.22)	(11.13, 11.35)	(50.76, 52.29)	(72.15, 72.52)	(15.14, 15.18)	(33.95, 34.08)
Average	103.47	11.42	53.85	91.34	18.65	42.16
95% CI[h]	(101.94, 104.15)	(11.32, 11.45)	(53.06, 54.22)	(87.71, 96.15)	(18.21, 19.09)	(40.45, 43.39)

a. DA is downscaled average monthly precipitation amounts (mm).

b. DN is downscaled average monthly number of rainy days (day).

c. DSD is downscaled standard deviation of monthly precipitation amounts (mm).

d. SA is raw simulated average monthly precipitation amounts (mm).

e. SN is raw simulated average monthly number of rainy days (day).

f. SSD is raw simulated standard deviation of monthly precipitation amounts (mm).

g. Confidence intervals based on jackknife analysis with respect to the stations

h. Confidence intervals based on jackknife analysis with respect to the GCMs

Table 2-6. Comparisons of average monthly precipitation amount (mm), average monthly numbers of rainy days (day), and standard deviations of monthly precipitation amount (mm) for observed, downscaled GCM, and raw GCM precipitation for all 17 stations averaged over the GCMs (period 1961-2000, all months).

Station ID	OA[a]	ON[b]	OSD[c]	DA[d]	DN[e]	DSD[f]	SA[g]	SN[h]	SSD[i]
Allentown	99.48	9.52	52.90	107.03	9.96	62.61	92.81	17.45	44.31
95% CI[j]				(105.40, 107.80)	(9.91, 10.00)	(61.29, 63.08)	(87.70, 98.40)	(16.87, 18.05)	(42.54, 45.50)
Chambersburg	91.41	9.23	49.06	97.84	9.68	53.64	94.02	18.37	44.86
95% CI[j]				(96.18, 98.90)	(9.57, 9.74)	(52.68, 54.09)	(90.69, 98.22)	(17.91, 18.99)	(43.24, 46.35)
Franklin	101.06	11.79	45.12	106.56	12.66	49.37	88.79	19.82	39.53
95% CI[j]				(105.53, 107.26)	(12.58, 12.71)	(48.95, 49.82)	(86.27, 93.32)	(19.43, 20.45)	(37.21, 41.07)
Greenville	92.19	12.19	40.73	96.81	12.35	44.62	87.79	20.11	38.35
95% CI[j]				(95.51, 97.41)	(12.27, 12.41)	(44.03, 45.05)	(85.04, 92.87)	(17.73, 20.76)	(36.64, 39.74)
Harrisburg	92.98	9.72	54.95	96.20	10.16	51.48	91.42	17.85	43.42
95% CI[j]				(94.80, 96.96)	(10.11, 10.20)	(50.45, 51.92)	(87.48, 96.69)	(17.31, 18.39)	(41.55, 44.73)
Johnstown	106.52	12.43	53.13	110.99	13.47	51.09	91.62	18.35	43.16
95% CI[j]				(109.42, 111.78)	(13.38, 13.51)	(49.91, 51.72)	(88.21, 96.85)	(17.91, 18.79)	(41.38, 44.40)
Montrose	110.25	12.37	52.68	117.54	13.33	58.11	93.64	18.95	41.94
95% CI[j]				(116.35, 118.10)	(13.22, 13.39)	(57.36, 58.74)	(88.50, 98.72)	(18.49, 19.40)	(39.89, 43.59)
New Castle	83.99	11.18	39.68	86.94	11.46	44.72	88.24	19.40	39.82
95% CI[j]				(85.82, 87.60)	(11.38, 11.52)	(43.84, 45.20)	(84.69, 93.28)	(18.98, 19.98)	(38.04, 41.04)

Palmerton	92.20	8.52	50.87	98.43	8.61	63.48	91.70	17.20	44.10
95% CI[j]				(96.43, 99.54)	(8.53, 8.67)	(61.95, 64.28)	(86.63, 96.78)	(16.66, 17.79)	(42.38, 45.27)
Ridgway	100.71	12.81	43.02	105.11	12.60	49.51	89.06	19.93	39.06
95% CI[j]				(103.86, 105.80)	(12.52, 12.66)	(49.00, 49.87)	(86.61, 93.59)	(19.57, 20.55)	(36.71, 40.60)
State College	90.93	10.84	47.97	98.93	11.58	52.67	92.29	19.08	42.32
95% CI[j]				(97.53, 99.63)	(11.47, 11.65)	(52.15, 52.93)	(90.14, 97.26)	(18.71, 19.59)	(41.33, 43.26)
Stroudsburg	109.41	10.13	55.43	123.58	10.94	69.52	91.56	17.76	42.95
95% CI[j]				(121.33, 124.69)	(10.83, 10.98)	(68.13, 70.23)	(86.18, 96.39)	(17.12, 18.40)	(41.05, 44.23)
Towanda	79.81	9.99	42.32	85.13	10.51	46.73	92.68	19.35	41.17
95% CI[j]				(84.00, 85.92)	(10.40, 10.55)	(46.35, 47.09)	(87.35, 97.69)	(18.91, 19.85)	(39.04, 43.09)
Uniontown	94.61	11.68	44.60	102.15	12.53	47.07	97.28	19.07	45.45
95% CI[j]				(101.15, 102.71)	(12.42, 12.58)	(46.68, 47.40)	(94.33, 101.85)	(18.67, 19.56)	(43.89, 47.01)
Warren	105.92	13.63	42.42	110.37	13.64	47.99	85.46	19.83	37.02
95% CI[j]				(109.39, 111.03)	(13.57, 13.69)	(47.43, 48.39)	(82.74, 89.61)	(19.48, 20.33)	(35.52, 38.25)
West Chester	101.97	9.47	56.36	113.53	10.14	66.56	91.30	16.99	44.00
95% CI[j]				(110.24, 115.07)	(9.99, 10.21)	(65.08, 67.22)	(87.79, 96.27)	(16.46, 17.54)	(42.27, 45.24)

York	93.45	9.67	54.59	101.89	10.43	56.33	93.05	17.58	45.19
95% CI[j]				(100.09, 102.73)	(10.30, 10.46)	(55.45, 56.67)	(89.10, 97.04)	(17.03, 18.11)	(43.54, 46.66)
Average	96.87	10.89	48.58	103.47	11.42	53.85	91.34	18.65	42.16
95% CI[k]	(96.04, 97.94)	(10.77, 11.00)	(48.09, 49.07)	(102.59, 104.62)	(11.29, 11.52)	(53.06, 54.43)	(91.17, 91.70)	(18.57, 18.74)	(41.97, 42.48)

a. OA is observed average monthly precipitation amounts (mm).

b. ON is observed average monthly number of rainy days (day).

c. OSD is observed standard deviation of monthly precipitation amounts (mm).

d. DA is downscaled average monthly precipitation amounts (mm).

e. DN is downscaled average monthly number of rainy days (day).

f. DSD is downscaled standard deviation of monthly precipitation amounts (mm).

g. SA is raw GCMs simulated average monthly precipitation amounts (mm).

h. SN is raw GCMs simulated average monthly number of rainy days (day).

i. SSD is raw GCMs simulated standard deviation of monthly precipitation amounts (mm).

j. Confidence intervals based on jackknife analysis with respect to the GCMs

k. Confidence intervals based on jackknife analysis with respect to the stations

Table 2-7. Absolute errors with respect to observations (expressed as %) for the average monthly precipitation amounts, average monthly number of rainy days, and standard deviations of monthly precipitation amounts across the 17 stations for all the months during the period 1961-2000.

GCM names	DPA[a]	DPN[b]	DPSD[c]	SPA[d]	SPN[e]	SPSD[f]
CCCMA	2.12	3.30	8.08	10.48	101.52	25.46
CNRM	9.42	5.89	15.81	13.11	97.43	17.37
CSIRO3.0	2.65	5.60	10.74	18.26	65.76	33.27
GFDL	6.96	5.57	10.57	9.14	77.58	15.33
GISS	19.38	12.03	23.55	45.02	47.07	17.68
IPSL	5.19	4.18	14.83	25.13	79.39	6.35
MIUB	7.72	3.79	11.30	9.80	107.26	21.94
MPI	3.44	3.69	9.81	11.50	41.99	11.29
MRI	6.73	5.08	7.62	24.80	41.65	29.11
Average across nine GCMs	7.07	5.46	12.48	18.58	73.29	19.75

a. DPA is downscaled percentages of absolute errors of average monthly precipitation amounts (%).

b. DPN is downscaled percentages of absolute errors of average monthly number of rainy days (%).

c. DPSD is downscaled percentages of absolute errors of standard deviations of monthly precipitation amounts (%).

d. SPA is raw simulated percentages of absolute errors of average monthly precipitation amounts (%).

e. SPN is raw simulated percentages of absolute errors of average monthly number of rainy days (%).

f. SPSD is raw simulated percentages of absolute errors of standard deviations of monthly precipitation amounts (%)

g. Confidence intervals based on jackknife analysis with respect to the stations

h. Confidence intervals based on jackknife analysis with respect to the GCMs

Table 2-8. Absolute errors with respect to observations (expressed as %) for the average monthly precipitation amounts, average monthly number of rainy days, and standard deviations of monthly precipitation amounts across the 9 GCMs for all the months during the period 1961-2000.

Station ID	DPA[a]	DPN[b]	DPSD[c]	SPA[d]	SPN[e]	SPSD[f]
Allentown	7.59	4.62	18.36	17.45	83.24	19.38
Chambersburg	7.53	4.92	9.33	19.21	99.02	15.03
Franklin	5.46	7.38	9.40	17.29	68.15	22.10
Greenville	5.06	2.53	9.54	17.48	64.99	18.91
Harrisburg	4.67	4.58	8.23	16.84	83.72	22.49
Johnstown	4.95	8.35	7.99	16.75	47.58	20.56
Montrose	6.61	7.81	10.30	21.00	53.25	23.74
New Castle	4.13	3.01	12.70	19.69	73.52	17.91
Palmerton	7.96	2.77	24.79	18.87	101.87	19.17
Ridgway	4.62	2.42	15.08	16.66	55.57	19.99
State College	8.79	6.84	9.79	18.19	75.96	17.41
Stroudsburg	12.95	8.02	25.43	21.44	75.30	23.60
Towanda	6.94	5.25	10.41	25.16	93.71	20.95
Uniontown	7.96	7.29	5.61	18.39	63.27	16.11
Warren	4.37	2.05	13.13	19.60	45.46	16.56
West Chester	11.50	7.08	18.09	16.36	79.50	22.51
York	9.03	7.87	3.93	15.51	81.89	19.42
Average across 17 stations	7.07	5.46	12.48	18.58	73.29	19.75

a. DPA is downscaled percentages of absolute errors of average monthly precipitation amounts (%).
b. DPN is downscaled percentages of absolute errors of average monthly number of rainy days (%).
c. DPSD is downscaled percentages of absolute errors of standard deviations of monthly precipitation amounts (%).
d. SPA is raw simulated percentages of absolute errors of average monthly precipitation amounts (%).
e. SPN is raw simulated percentages of absolute errors of average monthly number of rainy days (%).
f. SPSD is raw simulated percentages of absolute errors of standard deviations of monthly precipitation amounts (%)

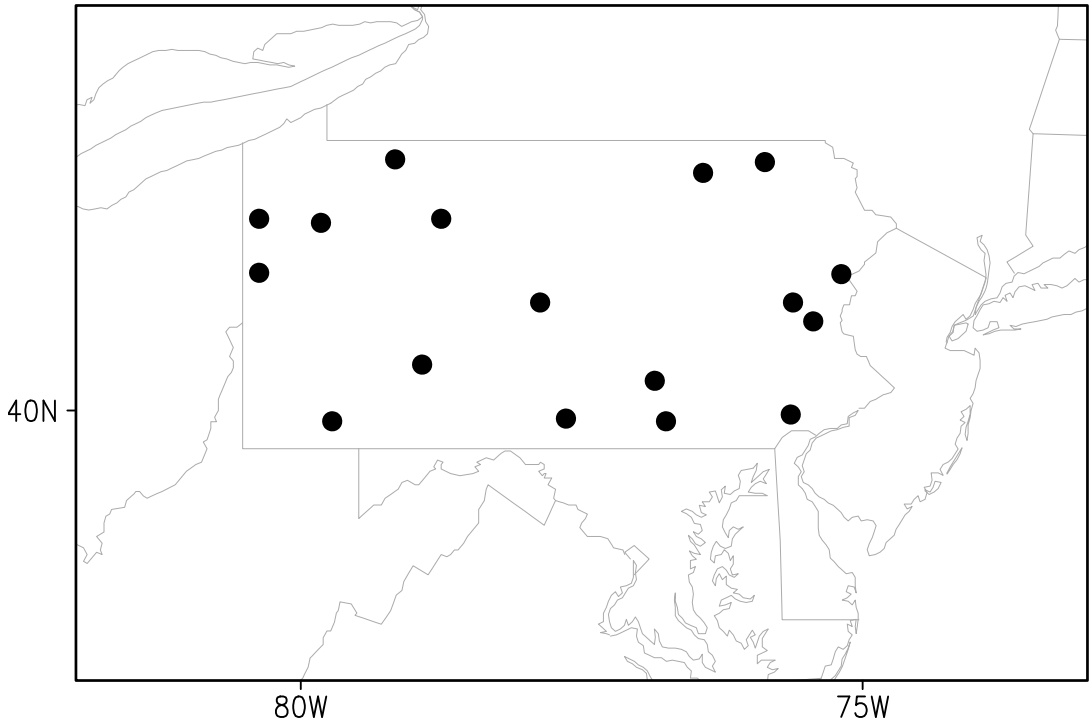

Figure 2-1. Map of Pennsylvania and the surrounding region, indicating the locations of the 17 meteorological stations used in the study.

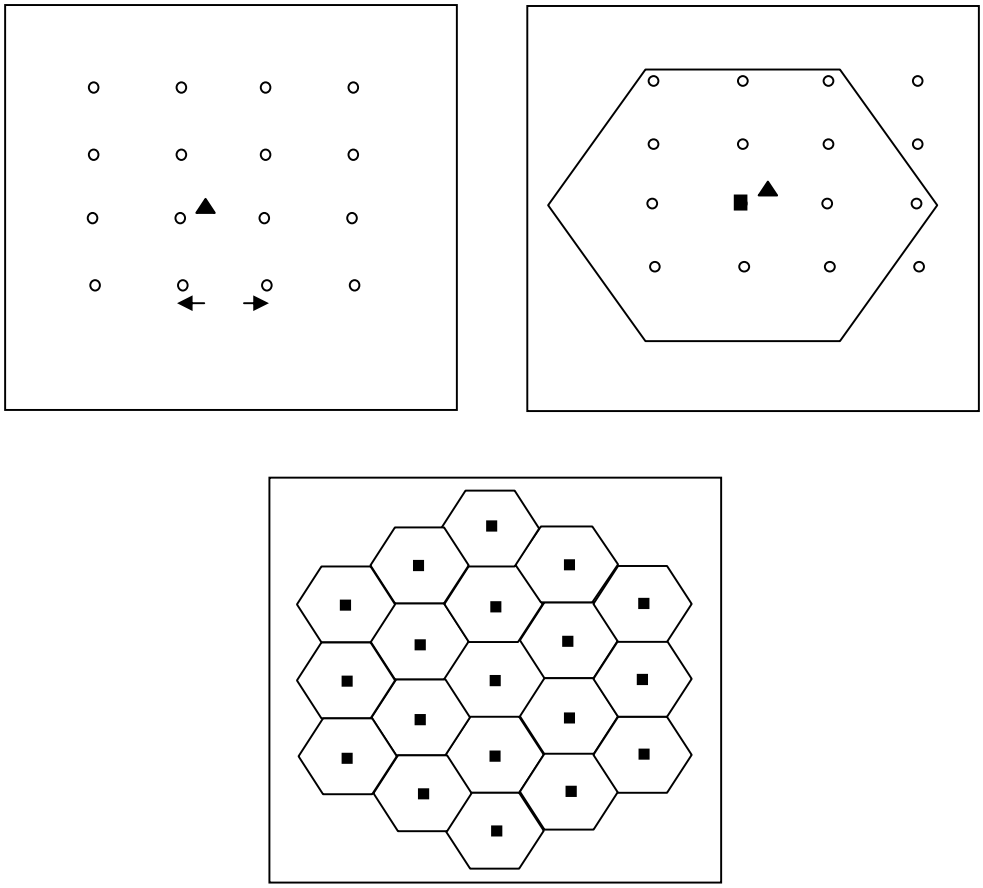

Figure 2-2. The SOMs pre-processing (triangle: target location).

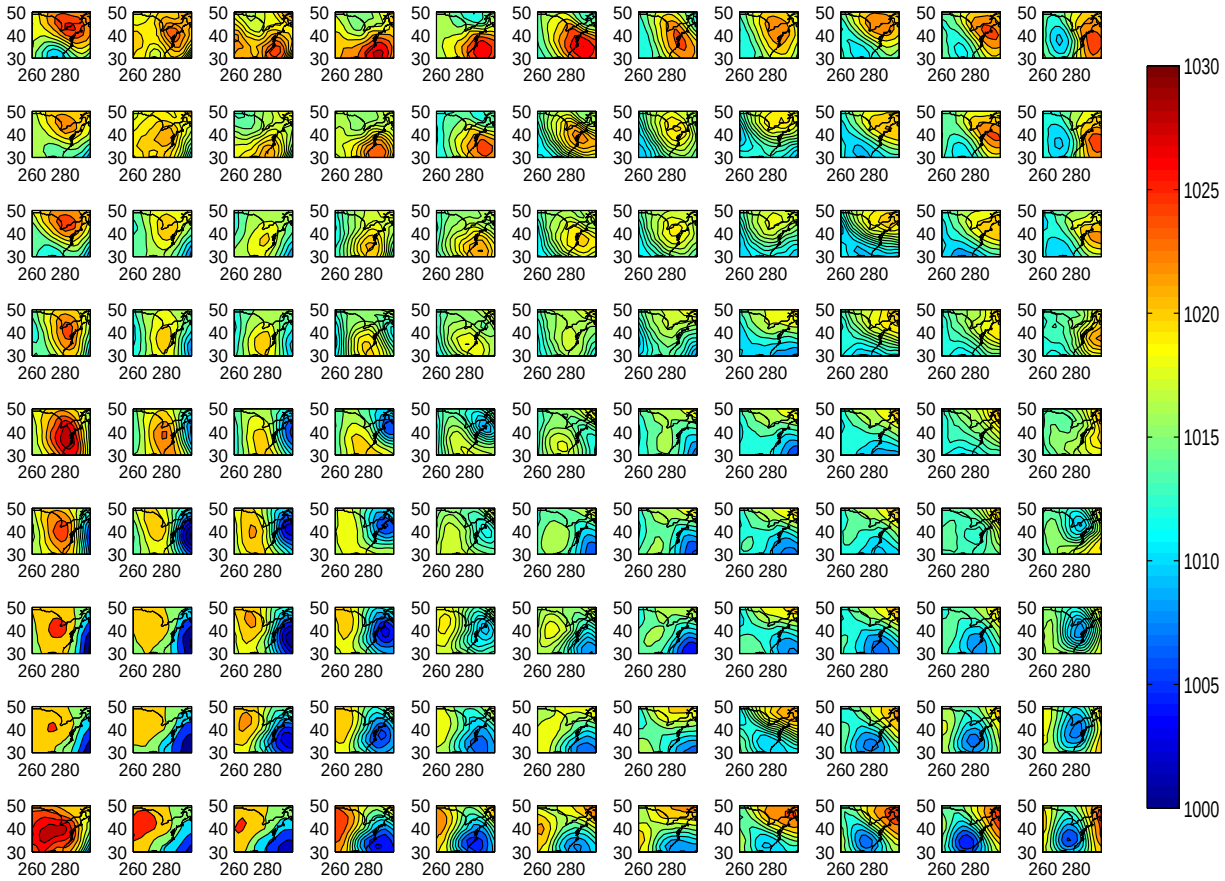

Figure 2-3. Sea level pressure distribution corresponding with 99 SOM nodes (Unit: hPa).

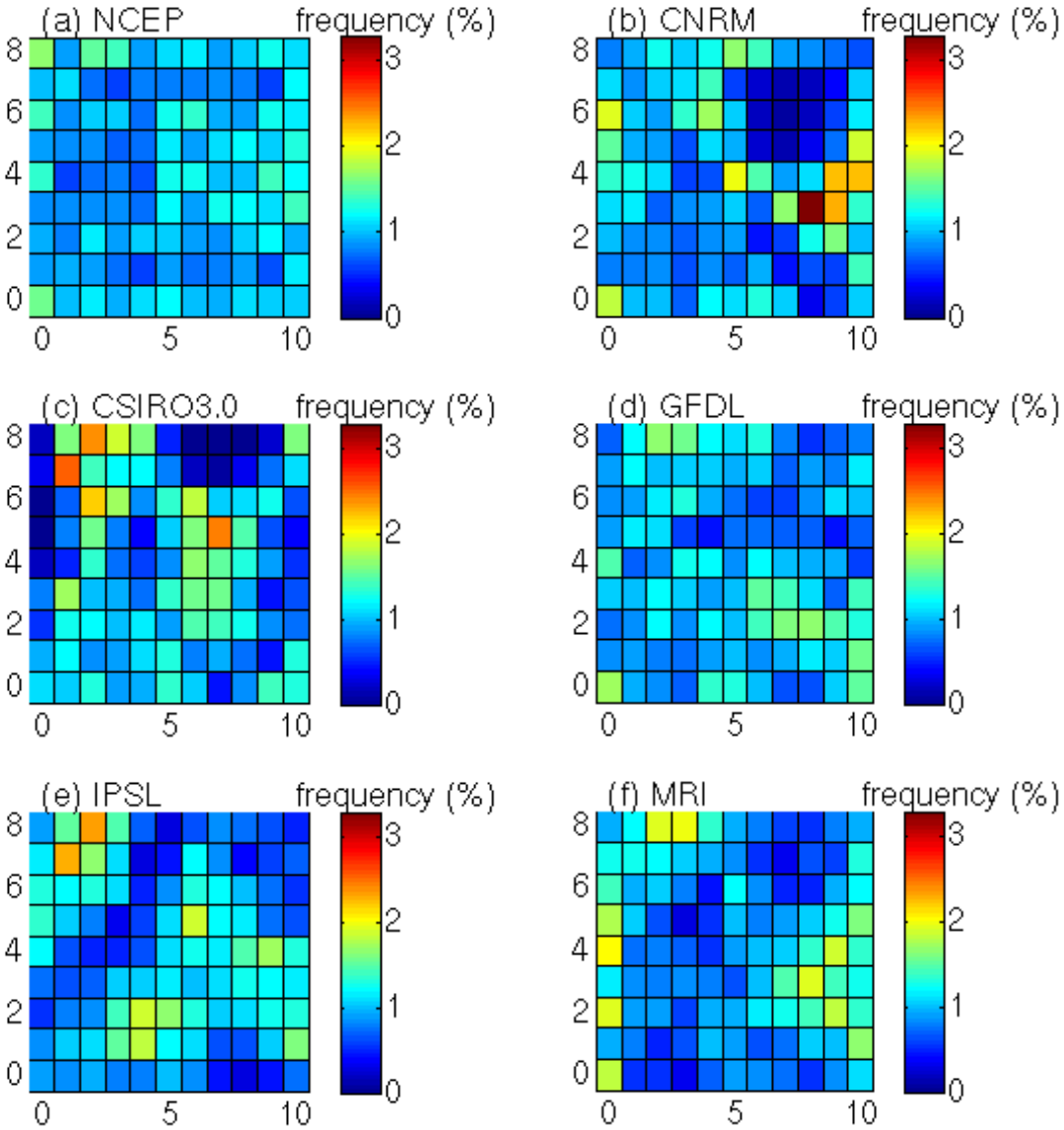

Figure 2-4. Frequency distributions across the SOM nodes for atmospheric circulation from NCEP (a), models CNRM (b), CSIRO3.0 (c), GFDL (d), IPSL (e), MPI (f) centered on 40.0°N and 76.5°W (Unit: %).

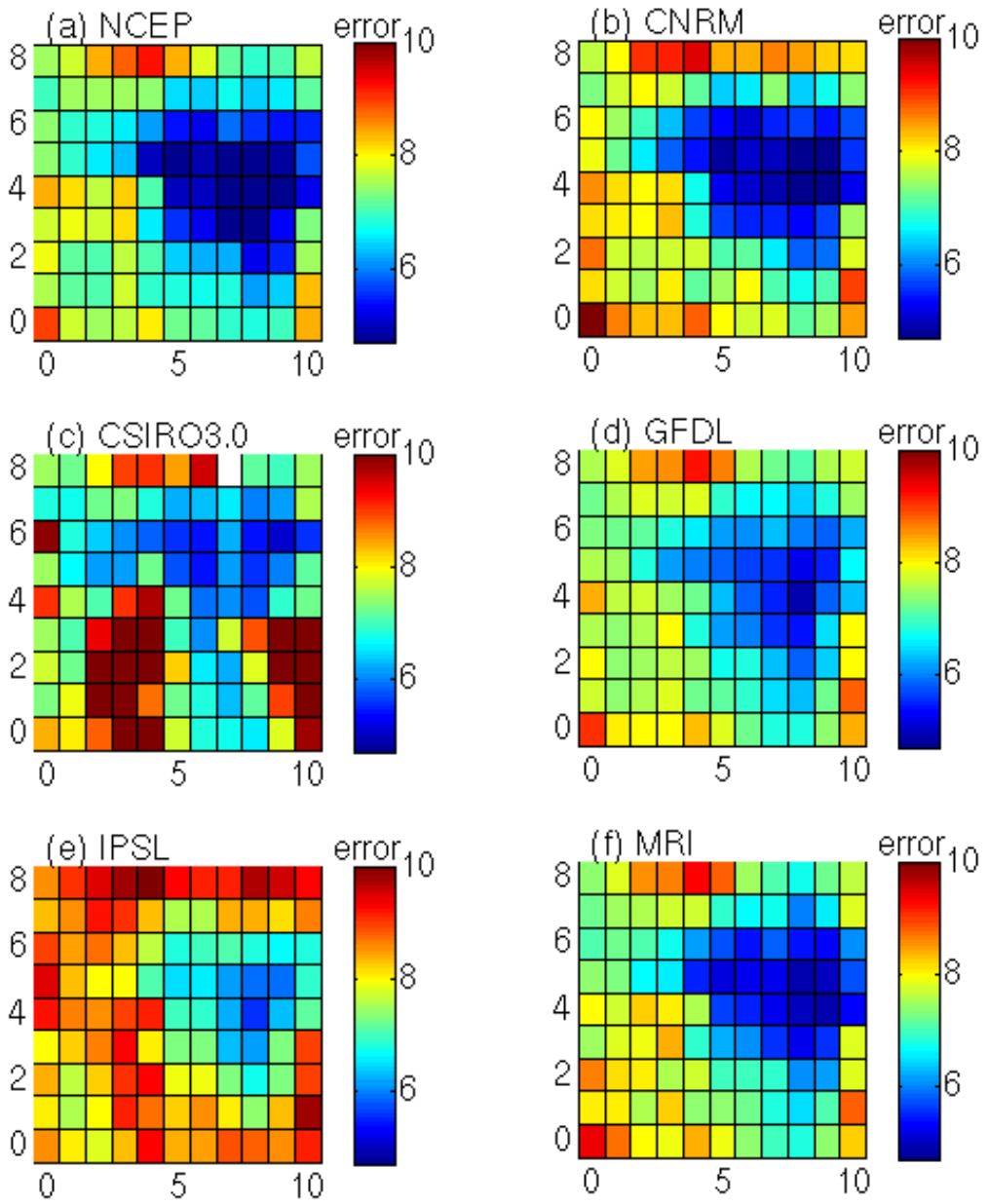

Figure 2-5. Average quantization error distributions across the SOM nodes for atmospheric circulation from NCEP (a), models CNRM (b), CSIRO3.0 (c), GFDL (d), IPSL (e), MPI (f) centered on 40.0°N and 76.5°W.

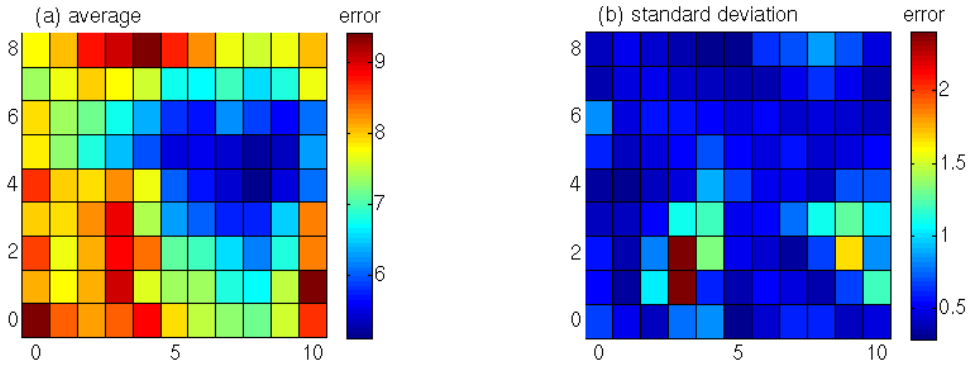

Figure 2-6. The average (a) and standard deviation (b) of the averaged quantization errors across the SOM nodes for NCEP and 9 GCMs circulation data centered on 40.0°N and 76.5°W.

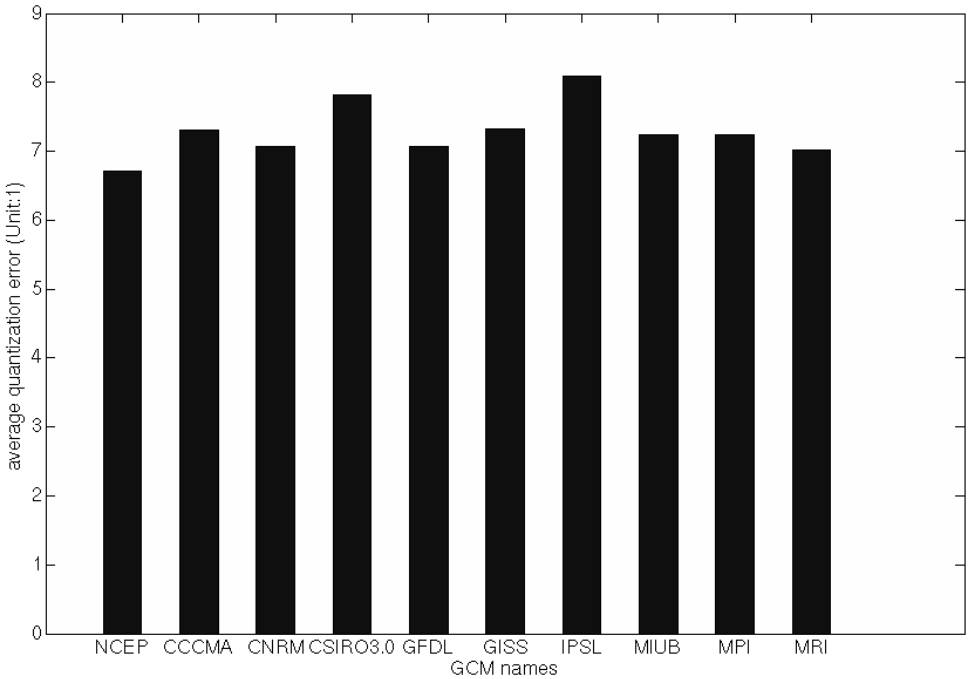

Figure 2-7. The average values of the averaged quantization errors over all the SOM nodes for NCEP and 9 GCMs circulation data centered on 40.0°N and 76.5°W.

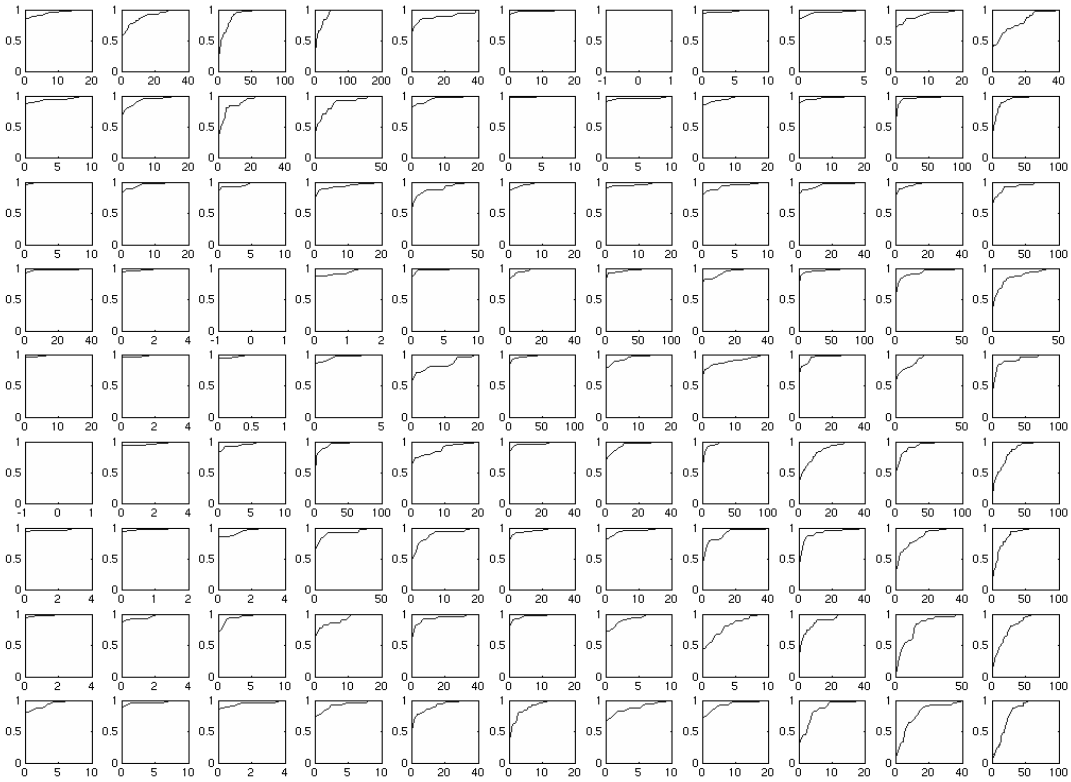

Figure 2-8. The cumulative distribution functions of daily precipitation values corresponding with 99 SOM nodes. (X-axis Unit: mm)

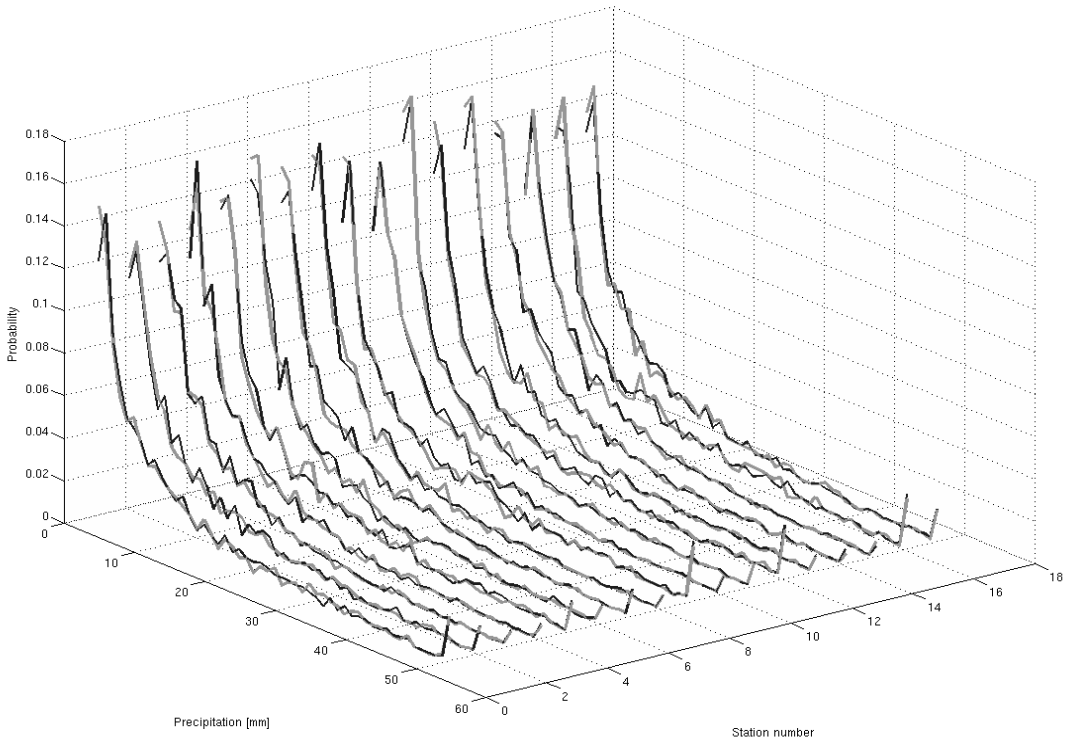

Figure 2-9. The probability distributions of observed (black) and downscaled (gray) daily precipitation over 17 stations in Pennsylvania during the period 1979-2005.

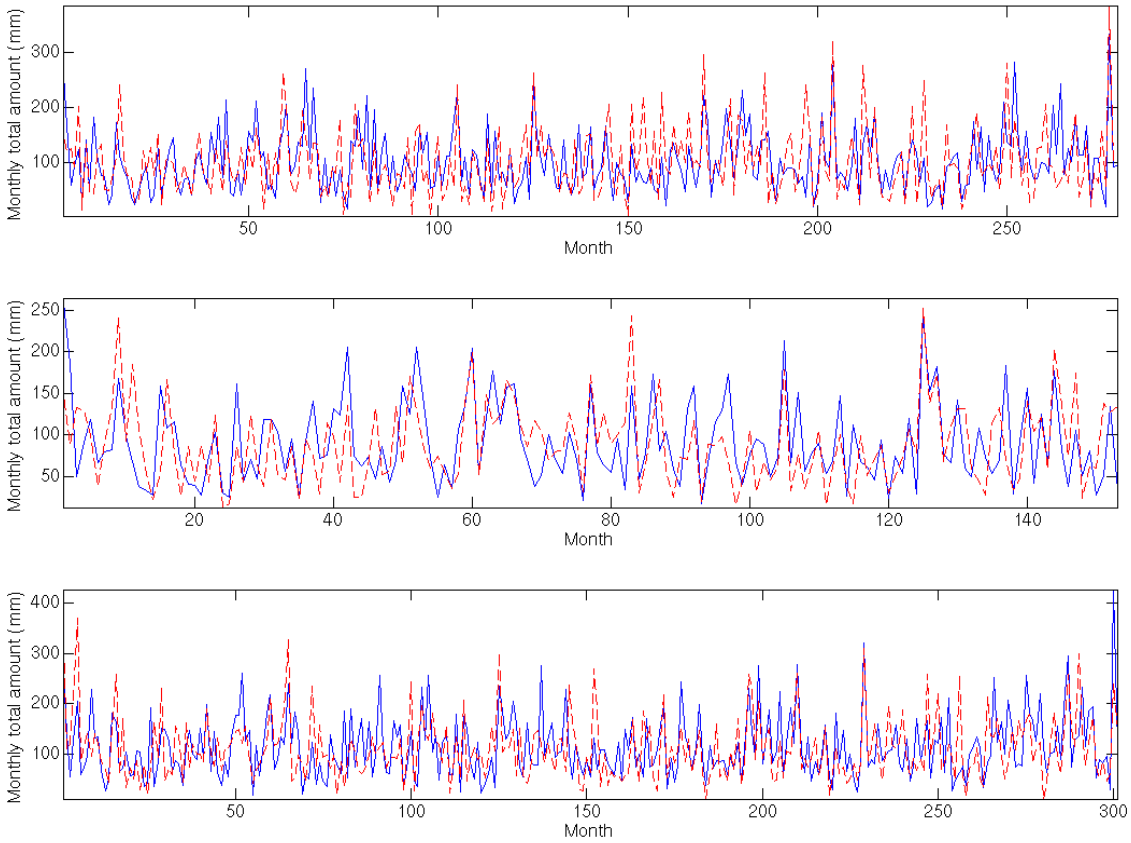

Figure 2-10. Observed (blue) and downscaled (red) monthly precipitation amount time series for period 1979-2005 over station Allentown (a), Harrisburg (b), and Towanda (c) (Unit: mm).

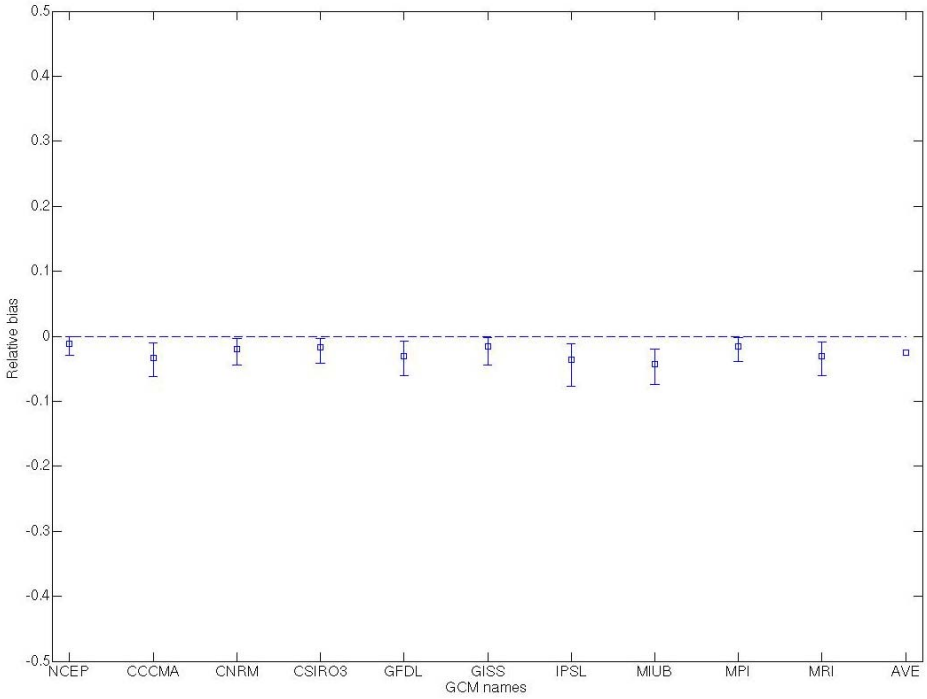

Figure 2-11. The average (square) and corresponding standard deviation (whiskers) of the relative bias of the monthly maximum dry spell from the downscaled results from NCEP data and nine GCMs across the 1500 iterations, and the average

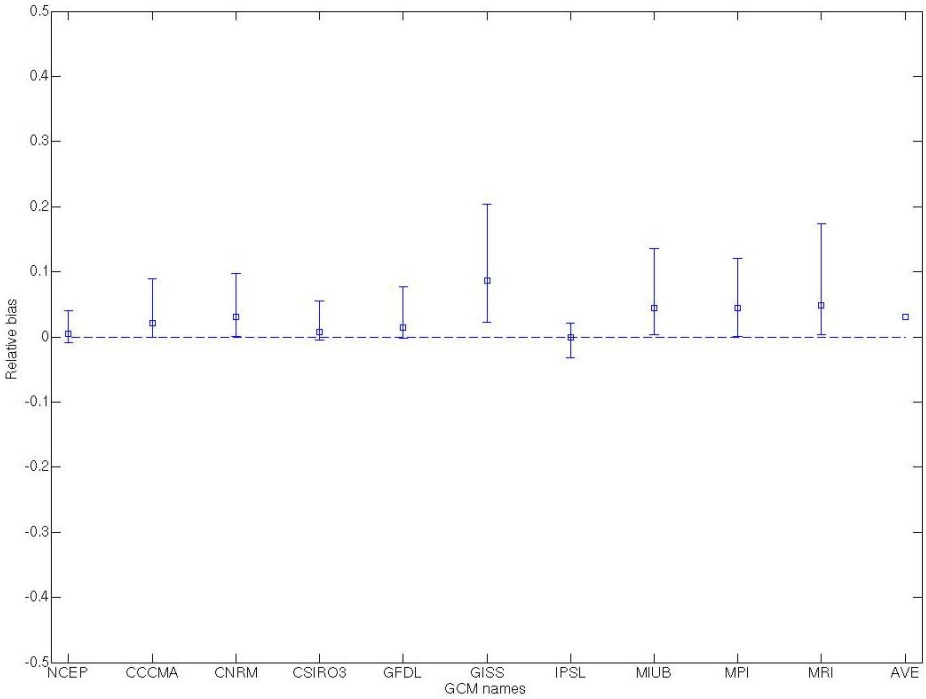

Figure 2-12. The average (square) and corresponding standard deviation (whiskers) of the relative bias of the monthly number of days with precipitation larger than 10 mm from the downscaled results from NCEP data and nine GCMs across the 1500 iterations, and the average

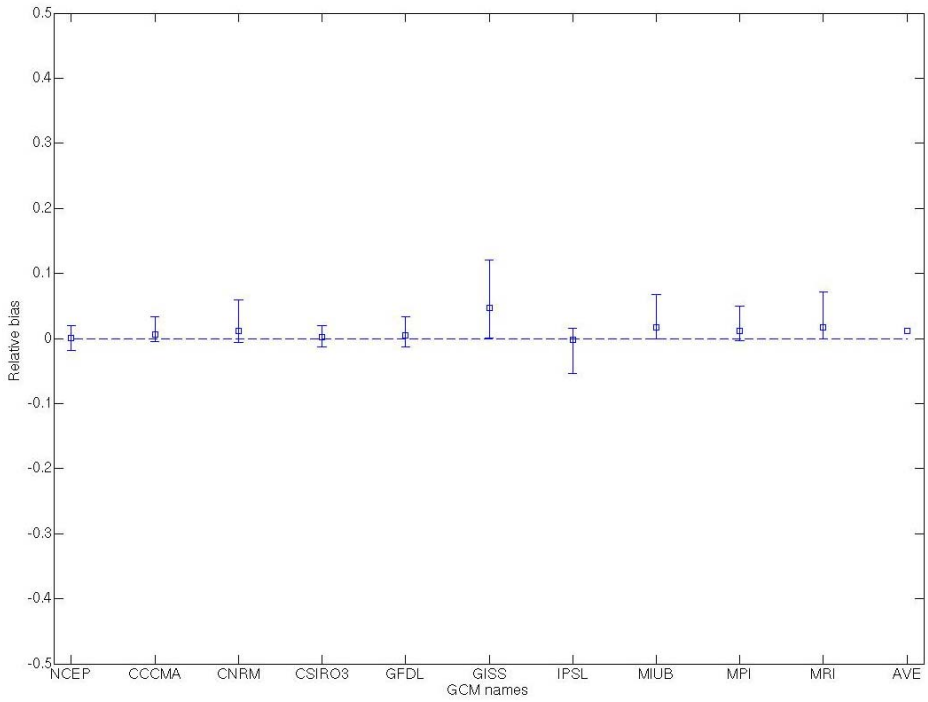

Figure 2-13. The average (square) and corresponding standard deviation (whiskers) of the relative bias of minimum total precipitation in consecutive 3 years from the downscaled results from NCEP data and nine GCMs across the 1500 iterations, and the average

Chapter 3

Probabilistic Projections of Anthropogenic Climate Change Impacts on Precipitation for the Mid-Atlantic Region of the United States

Introduction

Warming over the next century associated with anthropogenic increases in greenhouse gas concentrations is likely to be especially large over North America (Meehl et al, 2007). State-of-the-art General Circulation Models (GCMs) project that annual mean precipitation over North America is likely to increase in association with the consequent enhancement of atmospheric moisture (Christensen et al., 2007).

Although GCMs are the major tools used for future climate projections due to their well-established physical basis and ability to reproduce observed features of recent climate, particularly at continental and larger scales (Randall et al., 2007), GCMs cannot adequately resolve many important processes needed to capture regional climate changes, such as convective and topographically forced precipitation. Yet capturing such details is crucial for climate change impact studies at decision-making scales (Barron, 2009) and for the estimation of relevant hydrologic variables such as streamflow or soil moisture (Wagener et al., 2010). In order to bridge the gap between the GCMs and regional climate change, two types of downscaling methods have been developed and widely applied (IPCC, 2001; Christensen et al., 2007). One such approach, dynamical downscaling, uses Regional Climate Model (RCM) simulations (Chen et al., 2003; Plummer et al., 2006), while the alternative approach involves so-called statistical or empirical downscaling.

In this chapter we describe an application of empirical downscaling of daily precipitation over multiple locations in Pennsylvania (U.S.). The objective is to estimate future projections that can be used to drive hydrological and ecological models while employing a new approach to ensemble averaging, and to explore the uncertainty of these projections. Uncertainty exists in GCM projections of future climate largely because of the uncertainty in the projected anthropogenic forcing itself (i.e. the emissions scenario considered or 'scenario uncertainty'), inter-model differences in the physical parameterization of sub-grid-scale processes, and because of random variability and the dependence on initial conditions (see, for example, Maraun et al., 2010). Similar sources of uncertainty are found to dominate RCM projections (e.g. Rowell, 2005; Rowell and Jones, 2006). Frei et al. (2003) also conclude that deficiencies in the parameterizations for convection, the soil physics and land surface parameters, and the surface radiation balance are possible RCM error sources on simulations of daily precipitation statistics over European Alps. The sensitivity of projected mid-21st century climate changes is relatively insensitive to the scenario uncertainty (Fig. 10.4, Meehl et al., 2007); the spread in the projected global surface temperature increase through 2050 is only about 1 °C. It is thus reasonable to select, as in this study, one representative scenario, and focus instead on the physical uncertainties in projected future climate change

Much of these physical uncertainties arise from the characteristically low resolution and varying physical parameterizations of sub-grid-scale processes (radiative transfer, cloud formation, convection, etc) in the different GCMs analyzed (Meehl et al., 2007; Christensen et al., 2007). Downscaling can potentially circumvent, at least partly, the influence of such limitations on projections of daily precipitation. One caveat is that impacts from factors such as future land cover changes and the distribution of aerosols complicate efforts to downscale projected climate change to regional scales. Empirical downscaling does not reduce these additional scenario

uncertainties (although, with dynamical downscaling it is at least possible to examine the local sensitivity to these parameters).

Benestad (2002b) uses a multi-model ensemble method to evaluate the results of empirical downscaling of different global climate scenarios and different regions. He finds that the ensemble spread provides a crude measure of the uncertainties associated with different scenarios, and that different models show a reasonably strong level of agreement for projected winter temperature changes. Benestad (2004) also finds that a downscaling analysis of a multi-model ensemble can provide a first estimate for a probabilistic climate forecast, despite the large differences among climate scenarios and among GCMs. Hewitson and Crane (2006) also show that empirical downscaling can help to reduce the uncertainty arising from different GCM parameterization schemes. In this chapter, we will present how the downscaling method can reduce the inter-GCM uncertainties on future projected annual and seasonal precipitation changes.

Moreover, to assess the performance of downscaling methods in reducing uncertainty following the idea of Benestad et al. (2002a), we examine the changes of downscaled precipitation and related synoptic circulation North Atlantic Oscillation (NAO), which is the most prominent mode of atmospheric variability in the Northern Hemisphere winter climate (Wallace and Gutzler, 1981; Barnston and Livezey, 1987), and a major source of seasonal to interdecadal climate variability on winter surface temperature, storminess and precipitation over the Northern Atlantic and European regions (Deser, 2000; Thompson and Wallace, 2001; Wanner et al., 2001; Trenberth et al., 2007; Miettinen et al., 2011).

Due to the poleward expansion and weakening of the Hadley Circulation and a poleward shift of the storm tracks, sea level pressure is projected to increase over the subtropics and mid-latitudes and decrease over high latitudes as greenhouse gas concentrations increase in most models (Yin, 2005). Combined with other dynamical mechanisms related to the vertical structure of atmospheric temperature changes resulting from elevated greenhouse gas

concentrations (e.g. Miller et al., 2006), these responses generally lead to projections of a positive trend in the NAO across models (Meehl et al., 2007).

Many studies have shown that the NAO has a strong influence on regional temperature and precipitation variability over Europe (Hurrell, 1995; Rodó et al., 1997; López-Moreno and Vicente-Serrano, 2008). However, there are only a few studies addressing the influence of the NAO on precipitation patterns in North America, especially the Northeast U. S. (Hurrell et al., 2003). In this chapter, we investigate the relationship between winter precipitation over Pennsylvania and the NAO, and use model-projected changes in the NAO as a means of classifying and understanding some of the spread observed in the downscaled estimates of projected precipitation change.

Data and Methodology

Data and Downscaling Procedure

The study area Pennsylvania locates at Mid-Atlantic region of the U. S., and the locations of 17 stations used in this chapter are shown in Fig. 2-1. The observed precipitation data for the 17 stations are for the period 1961 to 2005. The empirical downscaling scheme used here is described briefly below and in detail in Ning et al. (2012a). The downscaling procedure employed here uses Self-Organizing Maps (SOMs) to define the characteristic modes of the synoptic-scale atmospheric state centered on each of the points (meteorological stations) for which the downscaling takes place. SOMs are analogous to a fuzzy-clustering algorithm, and are usually used to visualize and characterize multivariate data distributions (Kohonen, 1989; 1995). A SOM is typically depicted as a two-dimensional array of nodes, where each node is described by a vector representing the average of the surrounding points in the original data space. For an

input data set that is described by a matrix of n variable data points and m observations, each node in the SOM is described by a reference vector having length n. The initial step in the SOM training involves assigning random values to each node reference vector, and then comparing the data record with each node vector. The reference vector that most closely matches the data vector is defined as the "winning" node. Then the reference vector of the winning node is updated slightly toward the direction of the input data by a factor termed the "learning rate". All the surrounding nodes are also updated in the direction of the input data by a smaller learning rate. The entire process is then repeated for multiple iterations until the differences between iterations are smaller than a selected threshold value. This training procedure is described in detail in Crane and Hewitson (2003). In the training step, all the seven or eight variables (see descriptions below) from National Center for Environmental Prediction (NCEP) reanalysis data for period 1979-2007 are used to generate the SOM.

Then for each station, we compare the observed daily atmospheric data to the SOM nodes and map each day to one particular node. For each SOM node, we take all the days that map to that particular node and then rank the precipitation on those days from low to high. A spline is fit to the ranked precipitation data to define a continuous Cumulative Distribution Function (CDF) of the node's rainfall. This procedure is repeated for all the nodes in the SOM and then for all stations. In the downscaling procedure, each day's atmospheric state from present or future simulations of the GCMs is mapped to a node on the SOM, and a precipitation value is selected from the CDF of that node through the random number generator.

For a more detailed discussion of the downscaling procedure, and results for historical ("20c3m" CMIP3 multi-model) simulations, the reader is referred to our previous work (Ning et al., 2012a). During the historical period, our downscaling approach is shown to reproduce the major characteristics of the observed precipitation with smaller biases than the raw GCM-simulated precipitation. Here we apply the downscaling procedure to the 2046-2065 simulations

using the A2 emissions scenario for the same nine GCMs of the CMIP3 multi-model ensemble that were used for the historical period ('20c3m') analysis in Ning et al. (2012a): CCCMA_CGCM3_1, CNRM_CM3, CSIRO_MK3_0, GFDL_CM2_0, GISS_MODEL_E_R, IPSL_CM4, MIUB_ECHO_G, MPI_ECHAM5, and MRI_CGCM2_3_2A. In order to assess the sensitivity of future precipitation projections to the way in which changes in atmospheric humidity are represented, we try two downscaling approaches in this chapter. The first approach uses seven variables: *u*- and *v*- components of the wind at 10 m and 700 hPa, relative humidity at 850 hPa, air temperature anomaly at 2 m, and the lapse rate of temperature from 850 hPa to 500 hPa. In the second approach, the specific humidity at 850 hPa is added as an eighth variable in order to capture the water vapor increase brought by global warming.

Comparisons with an ensemble of RCM simulations over South Africa suggested that in some locations the use of specific humidity overestimated future rainfall change (Hewitson, Pers. Comm.). The rationale for including specific humidity is that increasing temperatures in the future could increase the potential for rain without changing relative humidity. Under present-day conditions downscaling over Pennsylvania with and without specific humidity gives essentially the same result (Ning et al., 2012a). Downscaling future climate projections, however, shows a significant difference. A range of input variables were tested prior to selecting the seven variables described in the original derivation of the methodology applied to South Africa by Hewitson and Crane (2006). In this chapter, therefore, we do not examine the uncertainty that results from including or excluding all combinations of input variables, but we do examine the differences that arise from including specific humidity as an additional humidity parameter.

Ensemble Averaging through Skill-based Weighting

In this chapter, we employ a new weighting method for constructing multi-model ensemble weighted-average monthly precipitation amounts from the individual downscaled model estimates, modified from a procedure introduced by Carter (2007) for South Africa. Calculating a weighted average based on the skill with which each GCM is able to recreate historical conditions is one option for producing a single time series from an envelope of ensemble projections (Brekke et al., 2008). The assumption is that models that do well under the present climate will also do well in the future. In this chapter we introduce a modification of the weighted average, accepting that with no better information to go on, the models that have higher skill in the present should be given greater weight in the future. However, we also consider that the relative skill exhibited by a particular model is not likely to be the same under all conditions, such as the large-scale atmospheric flow responsible for frontal rainfall and small-scale convection. The averaging method described here takes such variability into account.

The proposed method works as follows. During the downscaling procedure, each day's simulated atmospheric state is mapped to one of the characteristic synoptic states defined by the nodes in the SOM. As noted above, the SOM can be considered analogous to a non-linear fuzzy clustering algorithm, where each node in the SOM describes a cluster of points in the original multi-dimensional data space. For each node (or cluster) there is a corresponding quantization error defined by the distribution of points (days) that form the cluster. The quantization error is the sum of the absolute differences of each day from the group mean (analogous to the within group variance in cluster analysis). Larger quantization errors indicate greater variability between the days mapped to a particular node. The advantage of this approach is that it gives greater weight to those GCMs with simulations closer to the characteristic synoptic circulation and the weighting for each model changes each day as the atmospheric state changes. This

approach can generate a closer ensemble average to the observation than the simply averaging method for the historical period.

To produce an ensemble weighted-average daily precipitation amount, we first calculate the total quantization error from all GCMs for each day. We apply that quantity as a normalized inverse weight for that day's downscaled daily precipitation amount for each GCM and sum over the GCMs to obtain an ensemble averaged daily precipitation amount. The weighted ensemble average precipitation, $\overline{p}$, is given by:

$$\overline{p} = \sum_{i=1}^{9} \left(p_i * \frac{\frac{\sum_{i=1}^{9} e_i}{e_i}}{\sum_{i=1}^{9} \frac{\sum_{i=1}^{9} e_i}{e_i}} \right) \qquad (1)$$

where p_i is the downscaled daily precipitation for that day from the *i*th GCM, and e_i is the corresponding quantization error for that day from that GCM.

After generating the ensemble averages across all nine GCMs, the inter-GCM uncertainty is defined as the root mean squared deviation from the ensemble average for each precipitation metric. The same approach is used to compute the weighted ensemble average for both present and future conditions. The quantization error for the future projection shows how closely the simulation maps to the present atmospheric states, but the weighting also takes into account how the frequency of occurrence of those states changes in the future, thus the weighting of each GCM may actually change between the present and the future as changes occur in the simulation of the synoptic atmospheric conditions.

Results

Simulated Future Changes of the Synoptic States

Fig. 3-1a-i shows the differences in frequency distributions of characteristic synoptic-scale atmospheric states between the mid 21st century (2046-2065) and late 20th century modern control (1961-200) periods for the nine GCMs, for the Harrisburg station (40° N, 76.5° W), located in central Pennsylvania. The results shown correspond to the first of the two downscaling schemes (i.e., without specific humidity). Similar results are obtained using the second "dual humidity" scheme wherein specific humidity is used as well as relative humidity. The 11 × 9 matrix represents the SOM, where each cell in the matrix represents a characteristic synoptic atmospheric state composing seven circulation variables. The figure shows the percent difference in how many days map to each atmospheric state in the future compared to the present. Considering all days of the year (i.e. all seasons simultaneously), we see that for the majority of GCMs most of the substantial changes in frequency are found in the interior nodes of the SOM. When applying the averages plus/minus the standard deviations as significant thresholds, only 20%-30% of the nodes have significant changes for different GCMs. This observation suggests that the climate for this region is characterized by the same basic range of atmospheric states. The projected changes in climate, then, are largely represented through the shifts in the frequency of existing synoptic atmospheric states, rather than through the creation of new, non-analog states. Downscaling based on the SOM derived from present-day observations of the atmospheric state should thus be broadly valid for the projection of future changes.

Large increases in frequency at the edges of the SOM, if combined with large increases in the quantization error (Fig. 3-1j-r) on the same nodes might, on the other hand, indicate problems with stationarity (i.e., the future climate being so different to the present that it is trying

to map beyond the bounds of the SOM). The GCMs simulated present and future daily synoptic circulation state data sets should be considered as two data spaces. When the future synoptic circulation state data are mapped to the characteristic circulation patterns representing the present synoptic circulation state data, if the future synoptic circulation data are very different from the present synoptic circulation data, the SOM will have the tendency to map the days to the edges of the SOM, which are the bound of the present data space. Meanwhile, the quantization errors over the edges of the SOM will also be much larger since the future data spaces have much greater distances from the characteristic patterns than the present data space. Our results, however, show little evidence of such a problem and only about 10%-30% of the changes significant, with two notable exceptions: the IPSL and CSIRO 3.0 models. The IPSL model shows a reduction in quantization error across the whole SOM. This suggests that while the IPSL simulation of future climate includes the same range of atmospheric states, there is less variability around those states than exists in the present-day simulation. CSIRO 3.0, on the other hand, shows increased quantization errors on some nodes, and much reduced errors on others. This suggests that the future simulation exhibits a reduced range of states, but with increased variability around each state. Although it manifests itself in different ways, both models are showing reduced variability in atmospheric conditions in the future.

Fig. 3-2 shows the differences in quantization errors between the two periods averaged across all (99) SOM nodes, with their corresponding standard deviations, for each of the nine GCMs. With the notable exception of CSIRO3.0 and IPSL, the differences are indistinguishable from zero, reinforcing the conclusion that circulation states in the future map similarly close to their associated nodes for the present.

Projections of Future Precipitation (GCM versus Downscaled Results)

Changes in Annual Precipitation

Table 3-1 compares downscaled and raw simulated changes from late 20th to mid 21st century in average monthly precipitation amounts and number of rain days for each of the nine GCMs for the Harrisburg station. Only daily precipitation totals that meet the standard definition of a 'rain day' (larger than 0.25 mm, i.e. 0.01 inch--see Fitzpatrick et al., 1967; Hershfield, 1971; Gallus and Segal, 2004) are considered. Results are shown for the raw GCM projections as well as for the two downscaling methods.

For the downscaled precipitation based on the first method (relative humidity only), changes in monthly average precipitation range from roughly -3 mm to +9 mm, with an ensemble average +2.7 mm. All GCMs show small (less than 1 day) changes in the average monthly rain day totals, with an average of +0.2 days, considering both the observed and downscaled average monthly numbers of rain days are about 11 days. Using the second method (dual humidity variables), monthly average precipitation increases are larger, ranging from +0.6 mm to +8.7 mm, with an ensemble average of +3.1 mm, while the change in mean monthly rain day totals is identical (average of +0.2 days over models). For the raw model-simulated precipitation, increases are larger than those for either downscaling approach, with an ensemble averaged increase of +6.5 mm. The change in rain day totals (± 1 day) remains small, though the nominal number of rain days is already greatly overestimated (about 20 days per month) by the GCMs for the modern day control—see Ning et al. (2012a). Note that the inter-model variability, defined as the standard deviation, is much larger for the raw GCM changes than for either of the two downscaling-based estimates.

There is no consistent pattern between the three sets of results in Table 3-1 across models. For CCCMA, the projected change in precipitation is essentially the same for the raw GCM estimates and both downscaling estimates. For CNRM, the downscaling with both humidity values increases the projected rainfall change and moves it closer to the raw GCM values. For CSIRO3.0, on the other hand, using both humidity parameters reduces the projected increase and reduces agreement between the downscaling and raw model values. However, for six out of the nine models, using both humidity parameters enhances the precipitation increase in the future, since including specific humidity will take the future water vapor increase into account and tend to increase the precipitation probability in the downscaling procedure. For two models, the changes switch from negative to positive, and only in one case does it reduce the future change. Overall, the standard deviation of future projections is much greater for the raw GCM values than it is for either of the downscaling results.

Spatial Variation

Fig. 3-3a-f shows the spatial distribution of changes in precipitation and rain days for the ensemble average across the nine GCMs over all months. For the downscaling without specific humidity (Fig. 3-3a), decreases are found over northwest Pennsylvania, while increases are found over southeast Pennsylvania. This pattern of gradual increase from northwest to southeast also exists in the downscaled changes with dual humidity variables (Fig. 3-3c), but the changes in that case are all positive and larger than those changes in the downscaled results without specific humidity. One possible explanation for this spatial pattern is suggested by Rowell et al. (2006), who found that the large land-sea contrast in lower tropospheric warming will lead to reduced humidity in air advected from the Great Lakes to the continent and, therefore, reduced rainfall. For the raw GCM simulation (Fig. 3-3e), the gradient is from north-east to

south-west, which is very different from the downscaled results. Note, however, that the figure implies more spatial information than actually exists for the raw GCM values. The 4° x 7° area represents between 1 and 8 GCM grid cells, depending on the original GCM resolution, with 6 of the models having only one or two grid cells over the region. This illustrates the danger of simply interpolating low resolution GCM data to a higher resolution spatial grid. The uncertainty that exists in applying GCM data at the local scale is considerably reduced by downscaling to a finer grid or to point locations.

For the changes in monthly rain day totals, the spatial patterns of the two downscaled results are similar to the patterns of precipitation amount changes (Fig. 3-3b and 3-3d). For the raw GCM simulations (Fig. 3-3f), nearly all the stations have a reduced number of monthly rain days. Increased precipitation with fewer rain days indicates an increase in precipitation intensity, a common feature of both observation and GCM simulations of future climate globally (Tebaldi et al. 2006; Ning and Qian, 2009) and for the Northeast U.S. (Hayhoe et al., 2007; Shortle et al., 2009).

Fig. 3-3g-r show projected changes in the various precipitation metrics for summer and winter. The GCMs show weak agreement with each other in summer and strong agreement in winter in projected precipitation over Pennsylvania (see e.g. Fig. 11.12 in Christensen et al., 2007; Shortle et al. 2009). From Fig. 3-3g-l, we see that both downscaling approaches imply decreased average precipitation and reduced numbers of rain days over nearly all of Pennsylvania in summer. The raw GCM precipitation projections, by contrast, suggest increased monthly precipitation amounts and decreased monthly number of rainy days for most of Pennsylvania. For winter months (Fig. 3-3m-r), both downscaling approaches and the raw GCM simulations indicate increased average monthly precipitation amounts and rain day totals. The magnitudes of the downscaled changes, however, are once again smaller than the simulated changes. As

discussed below, this observation may in part relate to the greater role played by changes in the NAO in the downscaled precipitation projections.

Annual vs. Seasonal Trends

An aggregate measure of the projected 21st century trends in precipitation is provided by averaging the differences between middle 21st century 2046-2065 and late 20th century (1981-2000) across either all 17 stations, all nine GCM simulations, or across both stations and GCM simulations. Fig. 3-4 shows the changes in monthly precipitation amount (y-axis) versus changes in monthly rain day totals (x-axis) for the whole year (a, b), summer (c, d) and winter (e, f), defined as the differences between the period 2046-2065 and the period 1981-2000. Fig. 3-4 a, c, e show the results for nine GCMs averaged over 17 stations, and Fig. 3-4 b, d, f show the results for 17 stations averaged over nine GCMs.

Considering all days of the year, downscaling of the model simulations yields predictions of increased monthly mean precipitation for both downscaling approaches and all nine raw GCM simulations (Fig. 3-4a). Increases in monthly mean precipitation are observed for all 17 stations using either the raw model precipitation or the dual humidity variables downscaling scheme, and for most stations using the relative humidity-only downscaling scheme (Fig. 3-4b).

For rain day totals, Fig. 3-5a shows that most GCM simulations (averaging over stations) predict increasing trends using either downscaling approach. By contrast, the raw simulated precipitation indicates decreasing trends for most of the simulations. All stations exhibit increases using the dual humidity downscaling scheme (Fig. 3-4b). The stations cluster around zero with one station showing a decreasing trend in the downscaling with only relative humidity. The raw GCM precipitation fields, by contrast, show decreasing trends for all stations.

Greater inconsistencies are found at the seasonal scale. For the summer season, averaging across stations (Fig. 3-4c), roughly half of the GCM simulations predict increasing trends in both monthly mean precipitation and rain day totals for both downscaling schemes as well for the raw model precipitation field. Nearly all the GCMs predicting increases in monthly mean precipitation also predict increases in rain day totals. Averaging across GCM simulations (Fig. 3-4d), most stations in the relative humidity-only downscaling scheme, as with the raw GCM precipitation field, show decreasing trends for both monthly mean precipitation and rain day totals. Using the dual humidity variables downscaling, however, most stations show increasing trends for both monthly precipitation amounts and monthly rain day totals.

For the trends of winter months, when averaging across nine GCMs (Fig. 3-4e), most stations show consistent increasing trends on both monthly precipitation amounts and monthly number of rain days. This is more evident in the results averaged across 17 stations (Fig. 3-4f), with nearly all the GCM simulations showing increasing trends on both monthly precipitation amounts and monthly number of rain days, except several stations in the raw GCM simulations. Usually, the trends from both downscaling approaches are smaller than the trends from the raw GCM simulations.

Fig. 3-5 compares the histograms of monthly precipitation amounts and monthly rain day totals based on an ensemble of all nine GCMs from three approaches for a single station, Harrisburg. For both sets of downscaling results and for the raw GCM projections, there is a shift to the right with a fewer number of occurrences of months with lower rainfall amounts and an increase in months with higher rainfall totals (Fig. 3-5a-c). For the two downscaling approaches (Fig. 3-5d, e), there is also a shift with a fewer number of occurrences of months with small number of rainy days and an increase in months with larger number of rainy days. For the raw GCM projections (Fig. 3-5f), this shift appears on the month with number of rainy days larger

than 10, and the magnitude of the shift is much smaller suggesting a shift toward more intense rainfall events.

Analysis of Uncertainties

Comparisons of inter-GCM Uncertainties

There is considerably more uncertainty in the GCM simulations of precipitation than there is in their ability to simulate the larger scale characteristics of the atmospheric state. Because we use these large scale characteristics to downscale the precipitation, we get much closer agreement between the GCMs with the downscaled data than we do between the raw GCM simulations of precipitation. Consequently, the downscaling reduces some of the uncertainty that derives from different GCM parameterization schemes. The uncertainty introduced by using different input parameters for the downscaling is much less than the reduction in uncertainty obtained by using either of the downscaled data sets compared to the raw GCM values. This is further illustrated in Fig. 3-6, comparing the downscaled and simulated ensemble weighted-averages of mean monthly precipitation amount and monthly number of rain days averaged across all 17 stations, together with the corresponding inter-GCM uncertainties (computed as the root mean square difference from the ensemble average).

Fig. 3-6a compares the downscaled and simulated ensemble weighted-averages and inter-GCM uncertainties of mean monthly precipitation amount. For the annual changes using the downscaled results with only relative humidity, five GCMs predict increases for the monthly precipitation, and the ensemble average of the nine GCMs is 0.18 mm. For the downscaled results with both humidity values, six of nine GCMs predict increased monthly precipitation, and the ensemble weighted average is 2.09 mm. For the raw GCMs simulations, seven of nine GCMs

predict increases for the monthly precipitation, with an average of 7.02 mm. In each case, the root mean square difference from the ensemble weighted average is the greatest for the raw GCM precipitation.

Moreover, we also see that there is a seasonal difference, with the summer season showing greater variability between models than winter. For summer precipitation, although five of the GCMs simulate decreases in average monthly precipitation amounts, the ensemble weighted average shows a 2.15 mm increase. This is primarily a result of the large increase of 31.75 mm (40%) in the GISS GCM. Note that this model did less well at simulating the historical precipitation with a -45% error compared to observations (Ning et al., 2012a). The downscaling with one and two humidity values result in six and four models producing drying respectively. In both cases, the models are showing either a small increase in precipitation or a larger decrease, such that the weighted ensemble average suggests a slight drying. Including the specific humidity as a parameter to help define the atmospheric state increases the number of GCMs that project precipitation increases when averaged across the state, but the ensemble mean is still negative. This suggests that there is still considerable uncertainty in the summer precipitation projections, although the most likely projection is for little change or possibly a slight drying. This uncertainty in summer precipitation projections and the large difference between the GCM and downscaled projections also exist in dynamical downscaling conducted for North America (Chen et al., 2003; Han and Roads, 2004).

During winter, eight of the nine raw GCM projections give increased monthly precipitation. Seven GCMs project increases for the downscaling with RH only, and six for the downscaling with both humidity values. This level of agreement is most likely because of the strong synoptic control on precipitation during the winter months, with the differences between the raw GCM values and the downscaling arising because of the inability of the GCMs to capture

the higher resolution spatial variability. For both summer and winter, the root mean squared error is again much smaller for the downscaled projections than for the raw GCM data.

Fig. 3-6b shows similar results but for the monthly number of rain days changes. For annual changes, both the downscaling with only relative humidity and raw GCM simulation predict decreases of -0.04 days and -0.07 days, while the downscaling with dual humidity variables predicts an increase of 0.1 days. The downscaled inter-GCM uncertainty with only relative humidity is 0.26 days, and the downscaled uncertainty with dual humidity variables is 0.25 days. And both of them are smaller than the uncertainty from raw GCM simulations 1.29 days.

For summer months, both downscaling approaches and raw GCM simulations predict negative ensemble averages. The downscaling approaches with only relative humidity and with dual humidity variables predict the ensemble averages of -0.41 days and -0.18 days, and the raw GCM simulations predict the ensemble average -0.39 days. The inter-GCM uncertainties of the downscaled results are 0.52 days and 0.43 days, which are both smaller than the uncertainty of the raw GCM simulations (1.31 days). Based on our downscaling results and GCM simulated results over the Mid-Atlantic region, it seems that the increased humidity brought by global warming does not mean more or stronger convection in the future.

For winter months, both downscaling approaches show consistency with the GCM simulations on the ensemble average, but with reduced inter-GCM uncertainty. The ensemble averages of the two downscaling approaches are 0.32 days and 0.37 days, which are close to the raw GCM simulation (0.36 days). The inter-GCM uncertainties of the downscaled results are 0.35 days and 0.32 days, which are still smaller than the uncertainty of raw GCMs simulations (1.31 days).

So it can be concluded that for projections of both precipitation amount and number of rain days, the two downscaling approaches can obviously reduce the inter-GCM uncertainties introduced by different physical parameterizations from different GCMs.

NAO Influence on Winter Precipitation

Modern Observational Relationships

To examine the control of large-scale climate dynamics on the synoptic circulation patterns governing winter precipitation variability, we examined the relationship between the primary such dynamical feature—the North Atlantic Oscillation (NAO)—and winter precipitation variability over Pennsylvania that is the focus of our study. Fig. 3-7a shows the time series of the observed winter (Dec-Mar) NAO index, taken from the University of East Anglia (Jones et al., 1997; supplemented by more recent values available at: http://www.cru.uea.ac.uk/~timo/datapages/naoi.htm). Substantial variability is seen on both interannual and interdeadal timescales. High-NAO (defined as anomalies greater than +1 standard deviation above the long-term mean) years are 1966/67, 1982/83, 1988/89, 1991/92, 1992/93, 1993/94, 1994/95, 1999/2000, while low-NAO years (defined as anomalies as exceeding -1 standard deviation below the long-term mean) are 1962/63, 1964/65, 1968/69, 1976/77, 1978/79, 1995/96, and 2000/01.

We performed a series of analyses to confirm the NAO influence on synoptic-scale winter precipitation in Pennsylvania. In Table 3-2 we composite winter precipitation (Dec to Mar) for the years with high- and low- NAO indices. All stations except West Chester (this exception is likely due to the large amounts of missing data for this station in question) show a clear NAO influence, with greater mean precipitation during low-NAO years and less precipitation during

high-NAO years. The average differences over the 17 stations are significant at greater than the p=0.05 level using Student-t test, consistent with the previously established finding that positive NAO winters are associated with reduced mid-latitude storm influences on the region (Dong et al, 2010). In Fig. 3-7b, we show the composite sea level pressure (SLP) difference between the high- and low-NAO winters, which displays an increased penetration of the mean subtropical Bermuda/Azores high into the Mid-Atlantic region of the U.S., implying a blocking of mid-latitude storms, conducive to reduced storm-related winter precipitation in the region.

The relationship between the NAO and synoptic-scale precipitation was then evaluated for each of the nine GCM simulations. For each simulation, a winter NAO series was calculated as the difference between simulated SLP over the grid points closest to the centers of Bermuda/Azores high and Greenland low. To assess the ability of the models to reproduce the observed influence of the NAO on the synoptic-scale atmospheric circulation, we calculated the difference in SOM node frequencies between high- and low-NAO winters for each GCM simulation over the historical period and compared with a parallel analysis based on the NCEP reanalysis data (Fig. 3-8).

Having found that the main features in the SOM difference patterns shown in Fig. 3-8 are statistically significant, we evaluated the degree of similarity between the observed (NCEP) and GCM-simulated difference patterns. We calculated the pattern correlation between the NCEP SOM difference pattern and that of each of the 9 GCM simulations, employing a one-sided hypothesis test (since only a positive correlation is physical) assuming N=99-2 = 97 degrees of freedom. Only two of the models (GISS and CCCMA) provide a statistically significant (p<0.05) match with the observational SOM difference pattern, suggesting that these two models are best able to reproduce the observed influence of the NAO on the distribution of synoptic atmospheric circulation states (see Fig. 3-8; the one-sided p=0.05 significance threshold is r=0.166). Most of the models do, however, at least capture the general shift from the upper left corner of the SOM

(associated with high sea level pressure) to the bottom left corner (associated with low sea level pressure).

There are some caveats to keep in mind in this analysis. In the NCEP observations, there is some tendency for neighboring SOM nodes to change in opposite directions, suggesting that the NAO influence on synoptic circulation states is fairly subtle, i.e. that the differences between high and low positive NAO states results in somewhat subtle shifts in the strength or location of high and low pressure centers. With the models on the other hand, the changes in SOM occupancy show greater coherency in state space, with adjacent SOM nodes tending to change in the same direction. This discrepancy might indicate a too simplified representation of synoptic circulation states in the models, though it could alternatively result from biases in observational (NCEP reanalysis and station precipitation) data.

Projected Changes

Fig. 3-9 shows the relationship between projected 21st century trends of the NAO and projected changes in mean winter (DJFM) Pennsylvania precipitation. The NAO trends were defined by the best-fit linear trend in the diagnosed NAO series for each GCM over the common 21st century period 2004-2099. The trends in precipitation were defined, as earlier, by the differences between the simulated future period 2046-2065 and the simulated late 20th century period 1981-2000 as before, averaged over all 17 Pennsylvania stations. The symbols for GISS and CCCMA are highlighted for reasons discussed in the previous section.

From the figure, we can see that there is a very strong relationship between changes in the NAO and changes in winter precipitation, consistent with the substantial dynamical control on Pennsylvania winter precipitation evident for the late 20th century in both NCEP observations and the GCMs (see previous section). Those models with the greatest tendency toward the positive

phase of the winter NAO tend to show the greatest projected reduction in winter precipitation. The relationship is substantially stronger for the downscaled precipitation than for the raw GCM precipitation: r=-0.74 and r=-0.72 for the relative humidity-only and dual humidity downscaling respectively ($p \approx 0.01$ in both cases), vs. a much lower r=-0.22 (p=0.28) for the raw GCM-simulated winter precipitation. It thus appears that large-scale climate dynamics related to NAO are playing a far more important role in winter precipitation trends in the downscaled precipitation products than in the raw GCM simulations themselves. It is reasonable to speculate that this is due to limitations in the raw GCM simulation itself in capturing the subtle controls on winter synoptic-scale precipitation in the region that are alleviated or at least reduced through the use of appropriate downscaling methods. This can be tested through the composite analysis of the downscaled precipitation and raw GCM simulated precipitation during the GCM simulated high- and low-NAO winters in the future study.

Given the critical apparent relationship in the downscaling exercises between projected changes in the winter NAO and Pennsylvania winter precipitation, it is clear that clarifying and understanding the nature of response of the NAO to anthropogenic forcing is critical to reducing uncertainty in projections of winter precipitation. We note that six of the nine GCMs predict a tendency toward the positive phase of the NAO in response to projected anthropogenic forcing. That response is due at least in part to the intensification and westward expansion of the North Atlantic boreal winter Subtropical High with increasing CO_2 (Li et al., 2011), though more subtle responses involving the stratospheric response to anthropogenic forcing may be important (Miller et al, 2006).

Notably, the GISS model, which as discussed above displays the closest relationship with the observations with regard to the influence of the winter NAO on synoptic-scale circulation states influencing winter precipitation, projects a (modestly) negative NAO response to 21st century anthropogenic forcing. This response contributes to a larger projected increase in

winter precipitation. On the other hand, the other model (CCCMA) that reproduces reasonably well the observed NAO influence on synoptic-scale circulation, displays an opposite trend toward a more positive NAO, mitigating any tendency for increased winter precipitation.

As noted earlier, a weaker relationship is found between the projected changes in the winter NAO and winter precipitation using the raw GCM precipitation field (Fig. 3-9c). We speculate that synoptic-scale atmospheric dynamics are playing an artificially weak role in this case, owing to a combination of low model resolution and imperfect physical parameterizations of the processes governing winter-season synoptic-scale precipitation. In the absence of a realistic representation of large-scale dynamical controls on winter precipitation, the models are presumably producing an increase in precipitation in association with the larger atmospheric water vapor mixing ratios in a warmer winter climate. Consequently, the models' raw precipitation field, in eight of the nine model simulations, shows an increase in winter precipitation in the region.

Conclusions

Using a statistical downscaling method based on SOMs, we have presented projections of future (mid 21st century) changes in precipitation over the state of Pennsylvania. In order to examine the sensitivity of future precipitation due to changes in atmospheric water vapor associated with global warming, we tested two alternative approaches to downscaling, using either one (relative humidity) or two (relative and specific humidity) humidity variables in calibrating relationships between atmospheric variability and precipitation. An examination of the resulting SOM node distributions and the associated quantization errors suggests that the downscaling procedure is able to capture the prevailing synoptic circulation patterns that

characterize the warmer climate of the mid 21st century for both cases, thus providing justification for using the SOM-based downscaling technique to project future changes in precipitation.

The downscaled as well as the raw GCM-simulated precipitation suggest an overall tendency for increasing trends in annual precipitation. Seasonal precipitation trends are more variable though. For summer precipitation, there is a large spread among models, and while the raw GCM precipitation and downscaling using relative humidity alone yield decreasing summer precipitation for most GCMs, downscaling using dual humidity variables yields increases. Indeed, the additional use of specific humidity in the downscaling always yields larger positive precipitation projections, suggesting that explicit use, in the training of the SOM, of specific humidity—which increases sharply with temperature via the Claussius-Clapeyron equation—yields greater sensitivity to the increased water vapor content of the atmosphere in a warming atmosphere.

For winter precipitation, there is greater agreement among GCMs and downscaling approaches and with raw GCM precipitation with regard to the projected tendency for an increase in precipitation, but the magnitude is strongly dependent on atmospheric dynamics related to the NAO. Particularly in the downscaled estimates, which explicitly incorporate synoptic-scale atmospheric dynamics in estimating precipitation, there is a tendency for greater winter precipitation increases in those models with less positive-trending changes in the NAO. In fact, downscaling of the minority of models that project a more negative NAO yields, in several cases, predictions of a decrease, rather than increase, in winter precipitation.

A method for generating ensemble average downscaled precipitation estimates, based on the use of information from the quantization errors in the downscaling approach, is also introduced in this study. Application of this approach does reduce the inter-GCM uncertainty seen in projections based on the raw GCM precipitation field, and will in principle allow for reduced uncertainty in probabilistic projections of future precipitation changes. In our future work

we will link this approach for creating downscaled ensemble projections to establish a novel Bayesian hydro-climatological framework able to produce probabilistic projections of hydrological indicators (Singh et al., 2011).

Table 3-1. The changes of the downscaled and simulated average monthly precipitation amounts and average monthly numbers of rain days between the future period (2046-2065) and historical period (1961-2000) from nine GCMs over station Harrisburg.

GCM names	DA[a]	DN[b]	DAB[c]	DNB[d]	SA[e]	SN[f]
CCCMA	8.53	0.18	8.70	0.39	8.65	-0.16
CNRM	1.28	0.32	6.05	0.16	10.00	0.66
CSIRO3.0	4.06	0.07	2.02	-0.10	5.65	-0.19
GFDL2.0	-1.06	-0.10	2.34	0.49	13.16	-0.20
GISS	2.79	0.39	3.07	0.40	24.66	3.26
IPSL	4.31	0.09	6.55	0.00	-7.47	-1.55
MIUB	-2.85	-0.16	0.61	-0.07	-7.93	-1.36
MPI	5.70	0.54	6.35	0.48	8.09	0.09
MRI	3.32	0.09	0.75	-0.03	3.56	-0.54
Ensemble average	2.68	0.16	3.10	0.19	6.49	0.00

a. DA is downscaled changes of average monthly precipitation amounts with only relative humidity (mm).

b. DN is downscaled changes of average monthly number of rain days with only relative humidity (day).

c. DAB is downscaled changes of average monthly precipitation amounts (mm) with both relative humidity and specific humidity (mm).

d. DNB is downscaled changes of average monthly number of rain days with both relative humidity and specific humidity (mm).

e. SA is simulated changes of average monthly precipitation amounts (mm).

f. SN is simulated changes of average monthly number of rain days (day).

Table 3-1. The average monthly precipitation amounts of the high- and low-NAO winters, and their difference (Unit: mm).

Station No.	Station names	Average monthly precipitation of the winters with NAO indices larger than one standard deviation to the mean	Average monthly precipitation of the winters with NAO indices smaller than one standard deviation to the mean	Difference between the average monthly precipitation of high- and low-NAO winters
1	Allentown	101.76	117.11	-15.34
2	Chambersburg	87.37	99.61	-12.25
3	Franklin	96.03	103.69	-7.66
4	Greenville	76.60	92.59	-15.99
5	Harrisburg	85.40	99.01	-13.61
6	Johnstown	108.51	134.48	-25.96
7	Montrose	115.96	130.71	-14.75
8	New Castle	67.46	87.75	-20.29
9	Palmerton	63.90	95.94	-32.04
10	Ridgway	89.75	110.06	-20.31

11	State College	89.16	97.88	-8.71
12	Stroudsburg	100.44	125.91	-25.47
13	Towanda	69.59	77.10	-7.52
14	Uniontown	94.90	101.25	-6.35
15	Warren	100.42	111.39	-10.97
16	West Chester	102.50	94.84	7.66
17	York	99.67	100.33	-0.66
	Average	91.14	104.69	-13.54

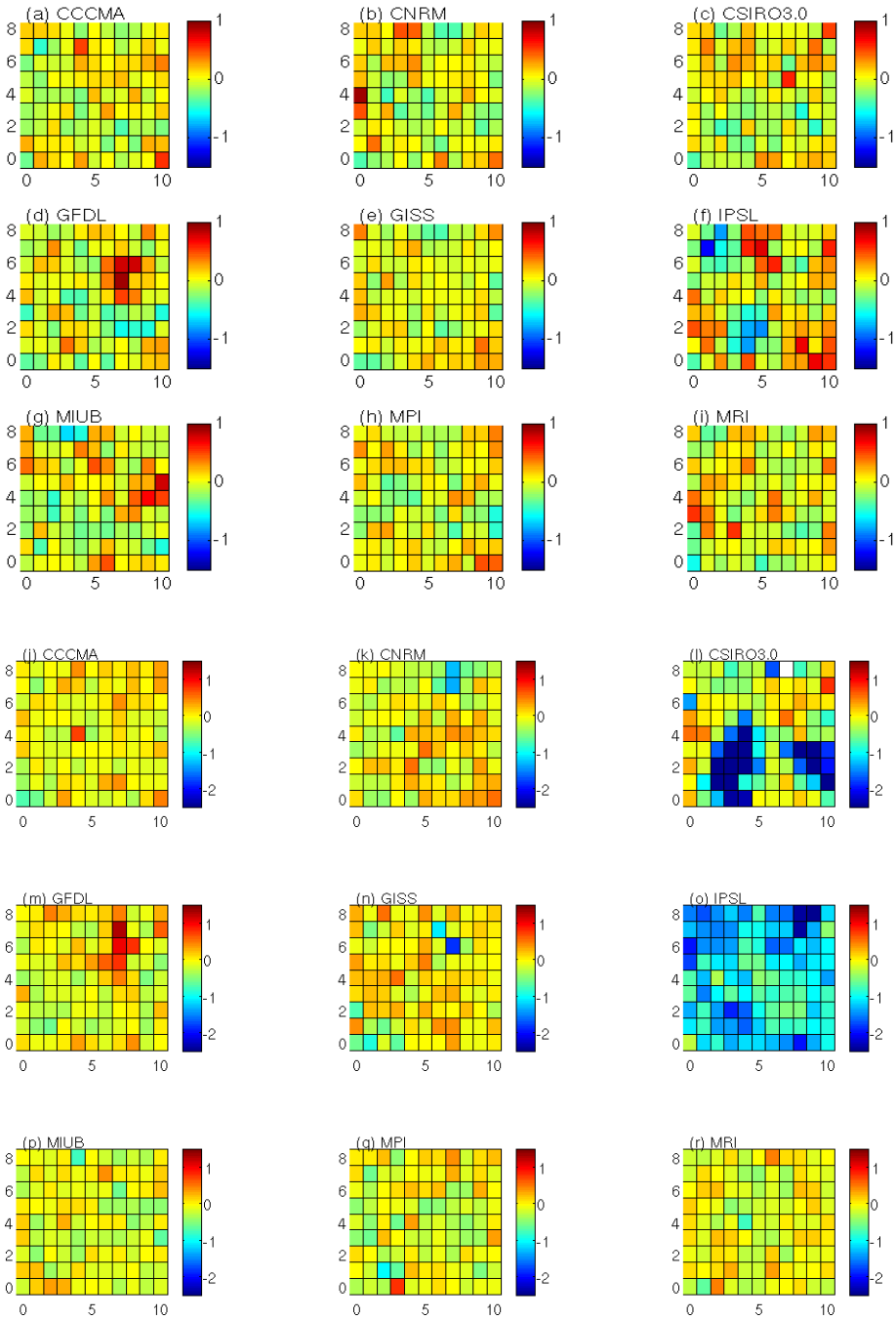

Figure 3-1. The differences of frequency distributions (a-i, unit: % change) and quantization error differences (j-r, unit: 1) between the future (2046-2065) and control (1961-2000) climate simulations centered on (40 °N, 76.5° W) for the nine GCMs.

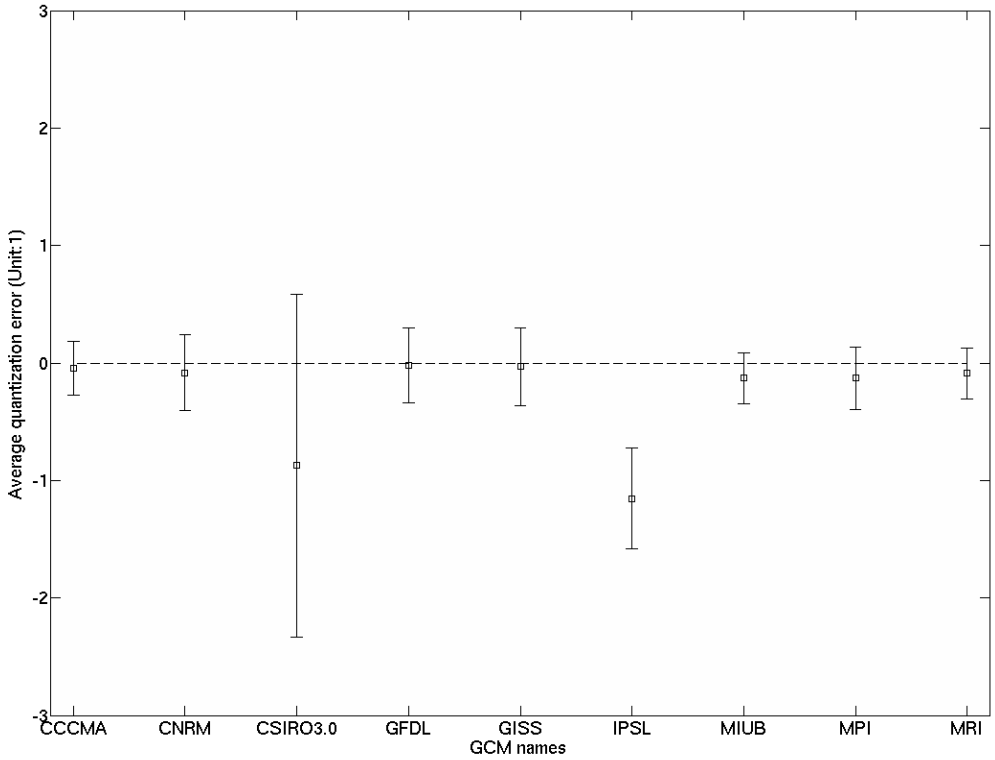

Figure 3-2. The values of quantization error differences averaged across all 99 nodes (squares) and standard deviations (whiskers) for the nine GCMs (Unit: 1).

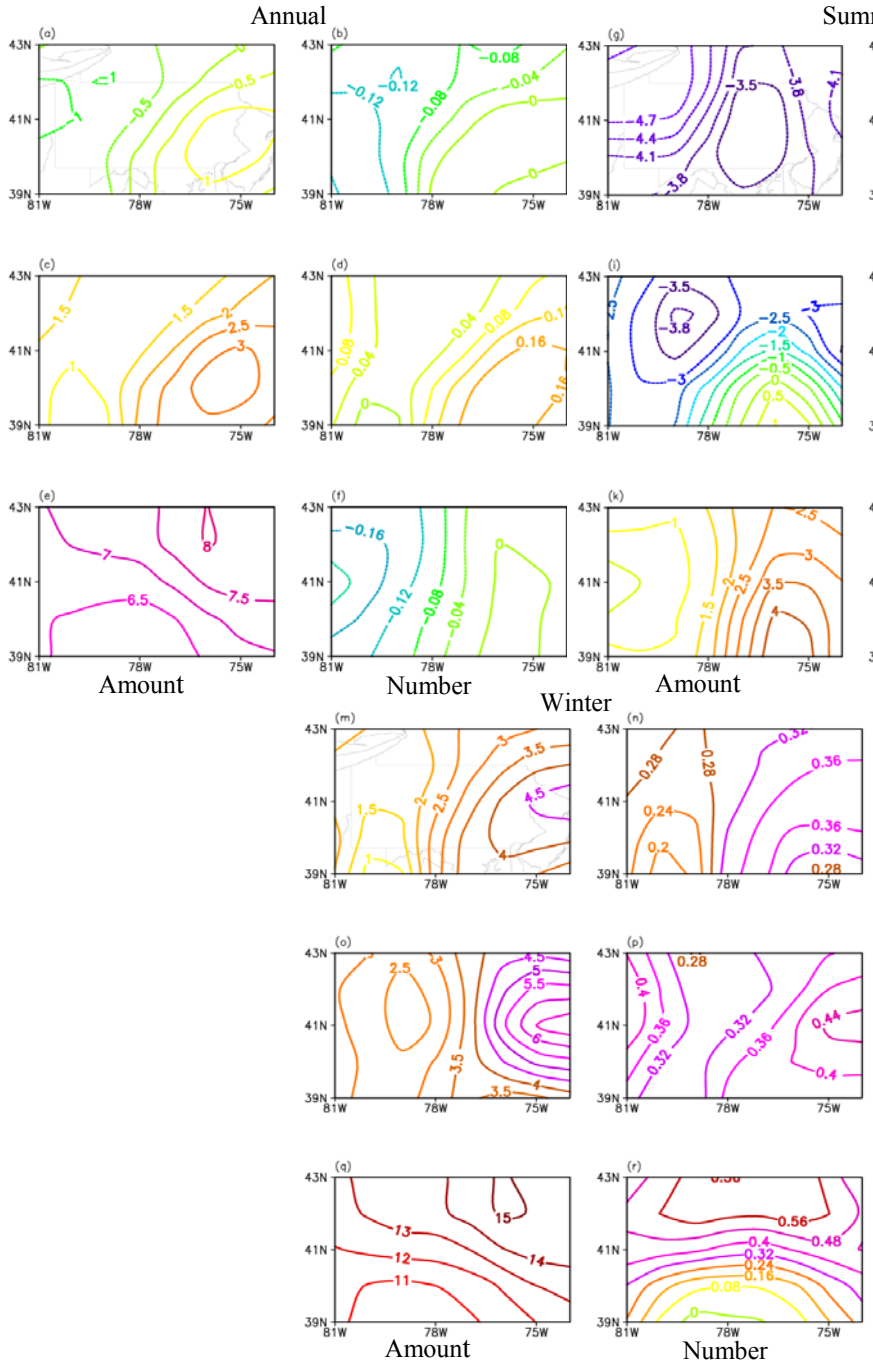

Figure 3-3. The spatial distributions of changes in annual (a-f), summer (g-f), and winter (m-r) mean monthly precipitation totals (left columns; in mm) and number of rain days (right columns; in day) based on downscaling using relative humidity (top rows), downscaling using relative humidity and specific humidity (middle rows), and raw GCM precipitation (bottom rows).

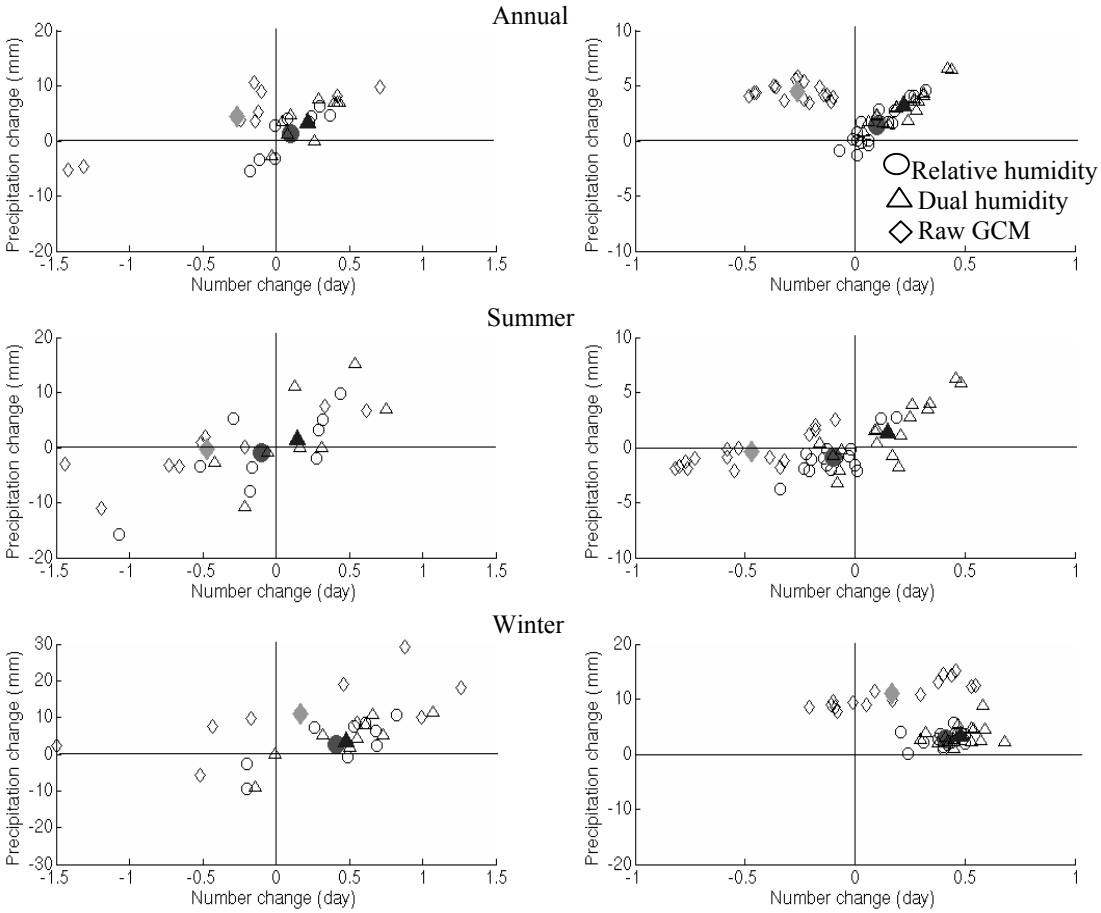

Figure 3-4. Future change of average monthly precipitation amount (y-axis, Unit: mm) and monthly number of rain days (x-axis, Unit: day) for annual (a, b), summer (c, d), and winter (e, f) months averaged over all 17 stations (a, c, e) and over nine GCMs (b, d, f) for the downscaled results with only relative humidity (circle), downscaled results from both relative and specific humidities (triangle), and raw GCM-simulated precipitation (diamond) between period 2046-2065 and period 1981-2000. The larger solid symbols show the average values of the group.

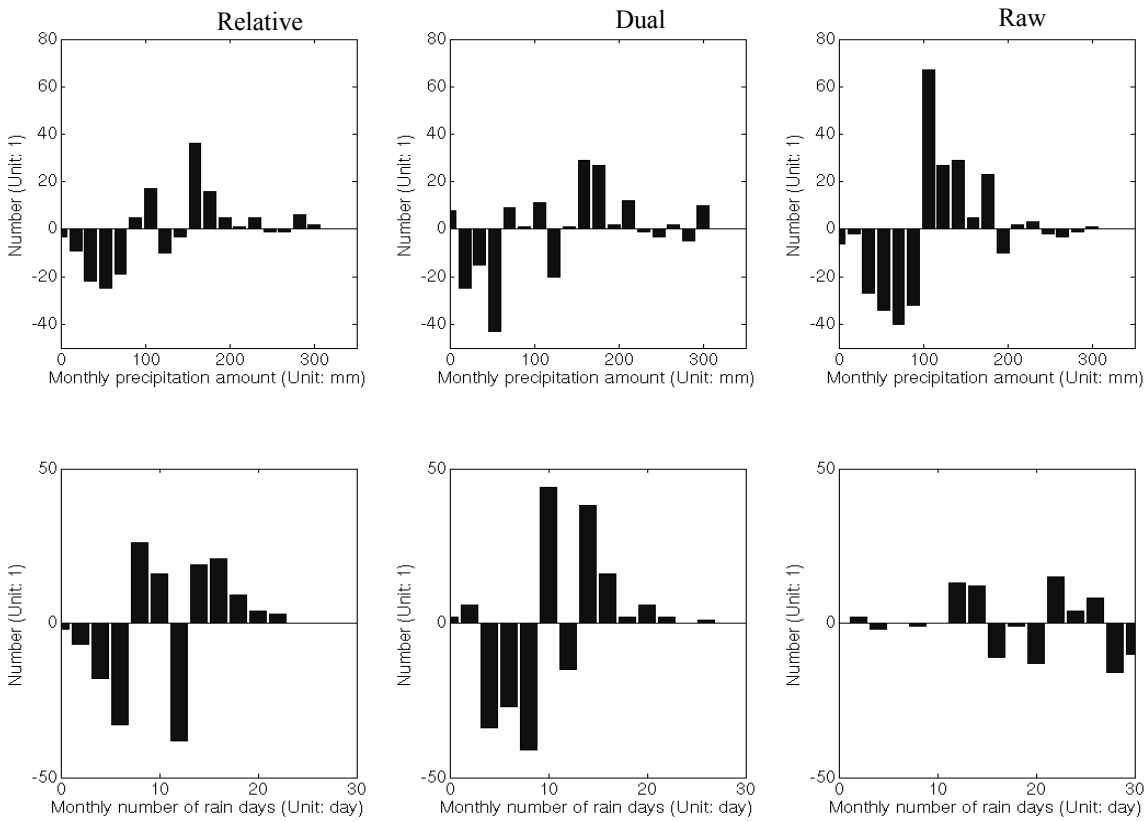

Figure 3-5. The changes of histogram of the monthly precipitation amounts (a-c) and monthly number of rain days (d-f) between future period 2046-2065 and historical period 1981-2000 from the downscaled results with only relative humidity (a, d), downscaled results with both humidity variables (b, e) and raw GCM simulations (c, f).

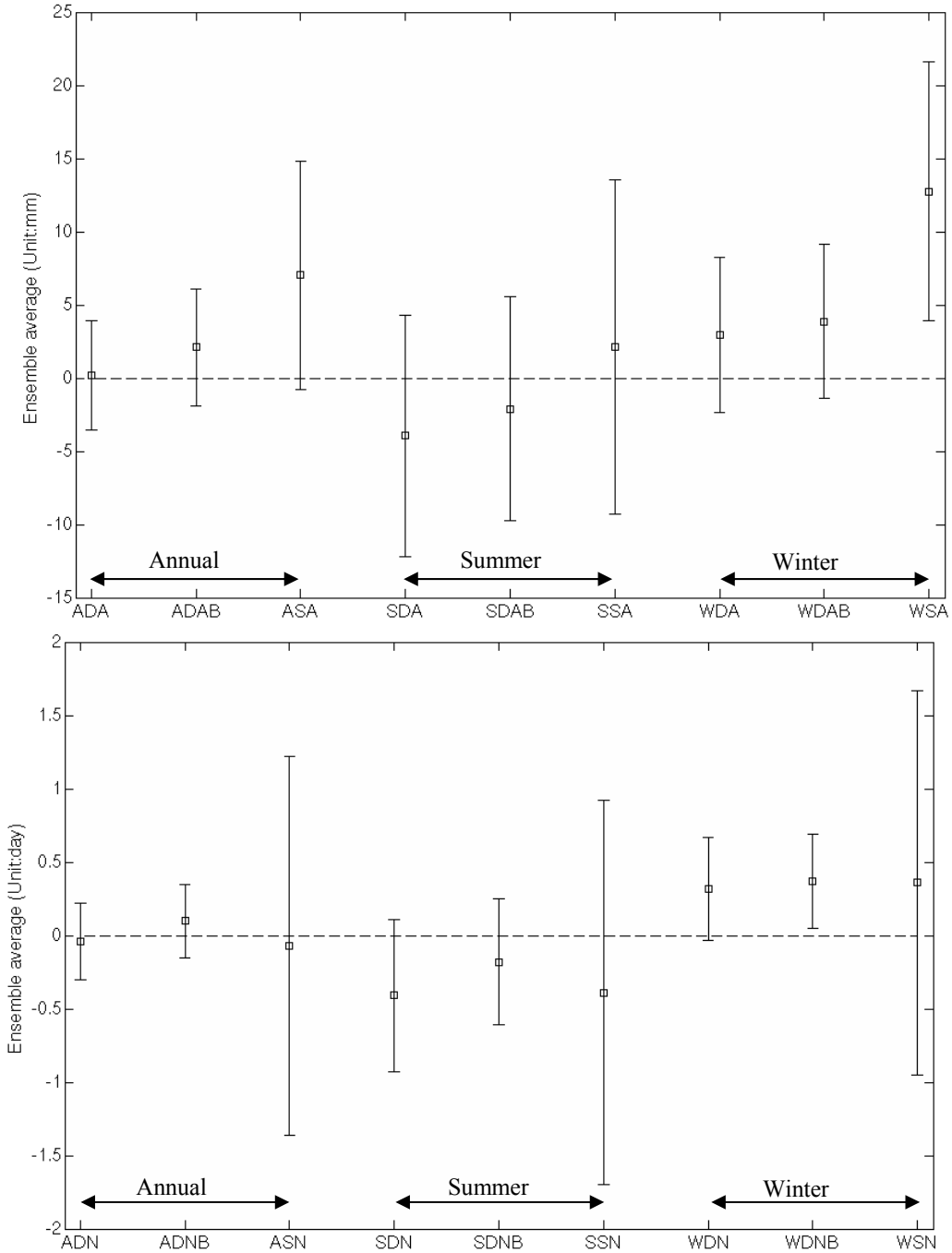

Figure 3-6. The ensemble averages of monthly precipitation amount changes (a) and monthly number of rain days changes (b) across nine GCMs (squares) and the corresponding inter-GCM uncertainties (whiskers) for annual, summer and winter months.

ADA: downscaled amount changes with only relative humidity for annual months (mm)

ADAB: downscaled amount changes with dual humidity variables for annual months (mm)

ASA: amount changes from raw GCM simulations for annual months (mm)

SDA: downscaled amount changes with only relative humidity for summer months (mm)

SDAB: downscaled amount changes with dual humidity variables for summer months (mm)

SSA: amount changes from raw GCM simulations for summer months (mm)

WDA: downscaled amount changes with only relative humidity for winter months (mm)

WDAB: downscaled amount changes with dual humidity variables for winter months (mm)

WSA: amount changes from raw GCM simulations for winter months (mm)

ADN: downscaled number changes with only relative humidity for annual months (day)

ADNB: downscaled number changes with dual humidity variables for annual months (day)

ASN: number changes from raw GCM simulations for annual months (day)

SDN: downscaled number changes with only relative humidity for summer months (day)

SDNB: downscaled number changes with dual humidity variables for summer months (day)

SSN: number changes from raw GCM simulations for summer months (day)

WDN: downscaled number changes with only relative humidity for winter months (day)

WDNB: downscaled number changes with dual humidity variables for winter months (day)

WSN: number changes from raw GCM simulations for winter months (day)

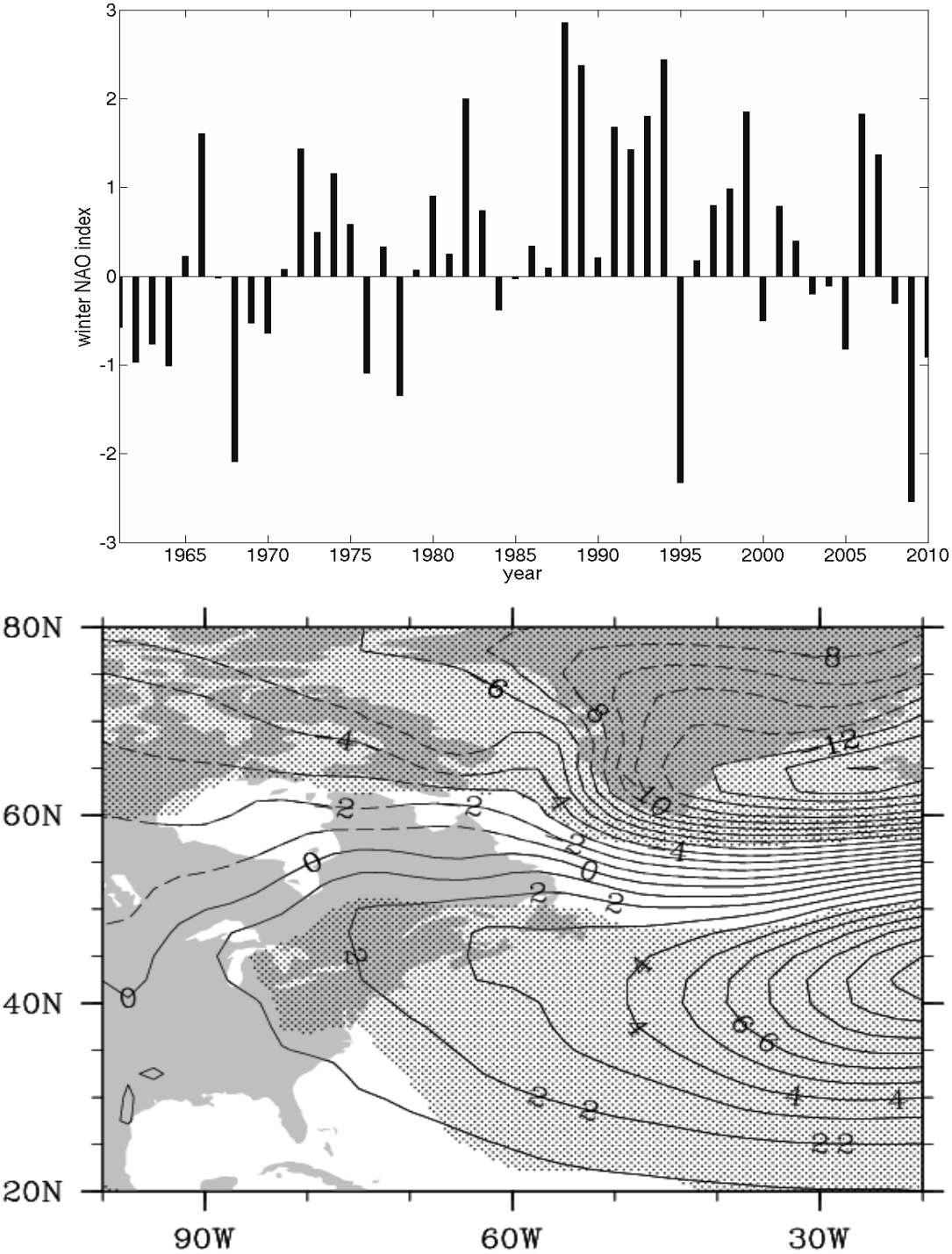

Figure 3-7. The time series of standard winter (DJFM) NAO index for period winter 1961/1962-2010/2011 (a), and SLP differences between winters with high- and low-NAO indices (b, unit: hPa). The shading indicates differences significant at the p=0.05 level.

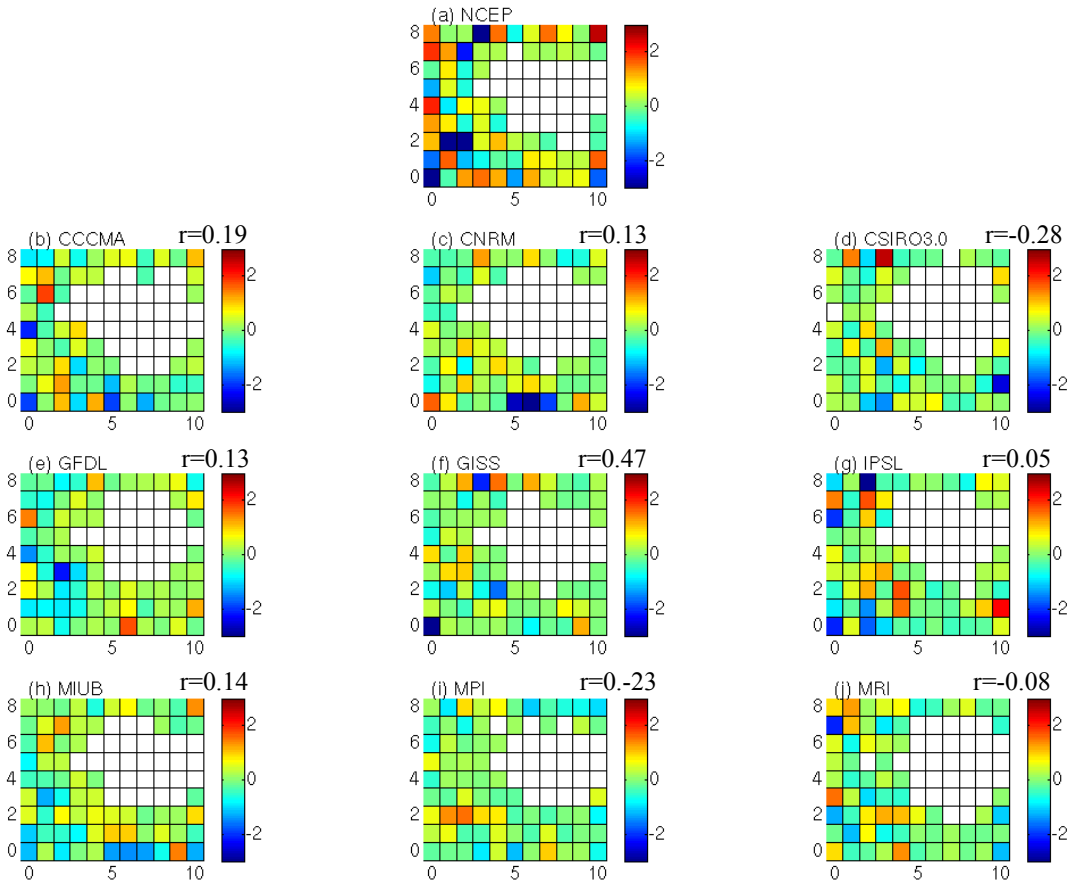

Figure 3-8. The difference of the frequency distributions of winters with high- and low-NAO indices from NCEP data and nine GCMs (Unit: %). Spatial correlations with NCEP pattern are given for each of the nine GCMs. White squares represent values of zero.

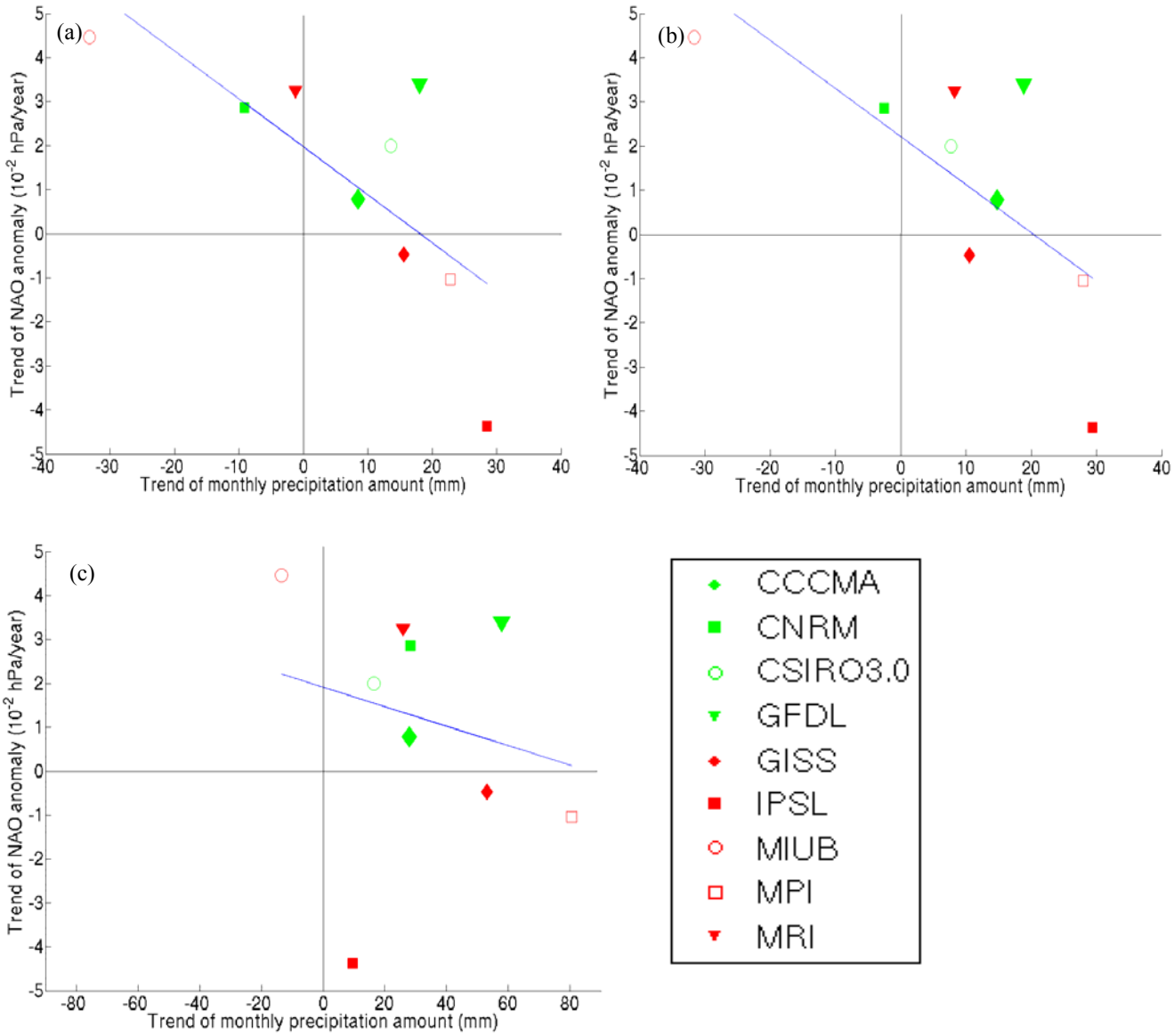

Figure 3-9. Projected trend in NAO (y-axis, unit: 10^{-2} hPa/year) against projected trend in mean winter precipitation over Pennsylvania (x-axis, unit: mm) with best-fit linear relationship (solid line). Shown are results based on downscaling with only relative humidity (a, r=-0.74, p=0.011), downscaling with dual humidity variables (b, r=-0.72, p=0.014), and the raw GCM simulated winter precipitation (c, r=-0.22, p=*0.28*). Results for GISS and CCCMA are highlighted as larger symbols, as discussed in text.

Chapter 4

Probabilistic Projection of Temperature Changes over Central Africa – Implication for Malaria Transmission

Introduction

Global mean surface temperature increased by about 0.74 ºC over the last century (Trenberth et al., 2007). According to simulations from different General Circulation Models (GCMs), this warming will very likely continue through this century, with the warming by the end of the 21st century relative to the end of 20th century ranging from 1 ºC to 7 ºC depending on various emissions scenarios (Meehl et al., 2007). On the regional scale, this warming is even more evident. Throughout Africa, the warming during this century is very likely to be larger than the global annual mean warming in all seasons, with drier subtropical regions warming more than the moister tropics (Christensen et al., 2007).

This warming will induce notable impacts on many ecosystems, the environment, and human health. Harvell et al. (2002) indicate that the warming over Africa will bring more frequent or severe infectious disease impacts through increasing pathogen development and survival rates, disease transmission, and host susceptibility. Among the infectious diseases, the transmission and distribution of malaria, which is a large threat to human health in Africa and warrants long-term investment for control, are greatly influenced by environmental and climatic factors, such as temperature and rainfall (Craig et al., 1999). Therefore, the assessment of potential change in malaria risk due to past and projected warming trends in Africa, especially over the Eastern African highland is one of the most important questions at the interface of climate science and human health (Patz and Olson, 2006). Most of these studies focus on the

impacts from mean temperature change; however, Paaijmans et al. (2010) show that in addition to mean temperature, daily fluctuations in temperature affect parasite infection, the rate of parasite development, and essential elements of mosquito biology that combine to determine malaria transmission intensity.

To predict future condition of malaria transmission, reliable regional temperature over Africa is needed. The GCMs are the major tools to predict future temperature, however, their coarse spatial resolution limits their applicability for assessing malaria transmission. To bridge the gap, different downscaling methods have been developed to transfer the coarse-resolution GCM simulations to qualified high-resolution regional climate changes (Christensen et al., 2007). In this study, we adopt a statistical downscaling method, which has been shown to be effective in both reproducing historical climate variability and predicting future precipitation changes over Africa and the Mid-Atlantic region of the United States (Hewtison and Crane, 2006; Ning et al., 2012a, b), to generate high-resolution temperature data sets to serve as input to a malaria transmission model. The downscaled temperature data are also evaluated using metrics relevant for malaria transmission model.

Many previous studies also indicate that El Niño – Southern Oscillation (ENSO) has a detectable influence on the transmission of infectious disease through temperature and rainfall anomalies, and the forecast system based on this relationship can help predict malaria risk and improve the lead time over malaria warnings (Harvell et al., 2002; Thomson et al., 2006). Therefore, in this chapter, we will also address the ENSO influences on regional temperature change over Africa, and analyze the downscaled temperature data in the content of ENSO.

Data and Methodology

In this chapter, observed maximum temperature and minimum temperature data from National Climate Data Center (NCDC) of 12 stations over Central Africa, which are 12 major cities and also important sites for malaria studies, are used. The locations of the 12 stations used in this chapter are shown in Fig. 4-1. The names, latitudes, longitudes, elevations, and the time periods of observed maximum temperature and minimum temperature of the 12 stations are presented in Table 4-1. The empirical downscaling scheme used here is described briefly here and in detail in Ning et al. (2012a). The downscaling procedure uses Self-Organizing Maps (SOMs) to define the characteristic modes of the synoptic-scale atmospheric state centered on each of the points (meteorological stations) for which the downscaling takes place. SOMs are analogous to a fuzzy-clustering algorithm, and are usually used to visualize and characterize multivariate data distributions (Kohonen, 1989; 1995). A SOM is typically depicted as a two-dimensional array of nodes, where each node is described by a vector representing the average of the surrounding points in the original data space. For an input data set that is described by a matrix of n variable data points and m observations, each node in the SOM is described by a reference vector having length n. The initial step in the SOM training involves assigning random values to each node reference vector, and then comparing the data record with each node vector. The reference vector that most closely matches the data vector is defined as the "winning" node. Then the reference vector of the winning node is updated slightly toward the direction of the input data by a factor termed, the "learning rate." All the surrounding nodes are also updated in the direction of the input data by a smaller learning rate. The entire process is then repeated for multiple iterations until the differences between iterations are smaller than a selected threshold value. This training procedure is described in detail in Crane and Hewitson (2003). In the training step, three variables (see descriptions below) from National Center for Environmental Prediction (NCEP)

reanalysis data for the period 1979-2007 are used to generate the SOM. For each station, we compare the observed daily atmospheric data to the SOM nodes and map each day to one particular node. For each SOM node, we take all the days that map to that particular node and then rank the maximum temperatures on those days from low to high. A spline is fit to the ranked maximum temperature data to define a continuous Cumulative Distribution Function (CDF) of the node's maximum temperature. In order to treat the daily maximum temperature and minimum temperature as a vector, the corresponding minimum temperatures are also arranged in a distribution for that node. This procedure is repeated for all the nodes in the SOM and then for all stations. In the downscaling procedure, each day's atmospheric state from present or future simulations of the GCMs is mapped to a node on the SOM, and a maximum temperature value and corresponding minimum temperature are selected from the CDFs of that node through a random number generator.

For a more detailed discussion of the downscaling procedure, and the performance for historical ("20c3m" CMIP3 multi-model) precipitation simulations over the U.S. Mid-Atlantic region, the reader is referred to our previous work (Ning et al., 2012a). Here we apply the downscaling procedure to the historical period 1961-2000 ('20c3m' emission scenario) and future period 2046-2065 (A2 emission scenario) for eight GCMs: CCCMA_CGCM3_1, CNRM_CM3, CSIRO_MK3_0, GFDL_CM2_0, IPSL_CM4, MIUB_ECHO_G, MPI_ECHAM5, and MRI_CGCM2_3_2A. GISS_MODEL_E_R is not used in this part of analysis because the output data over East Africa are not available. Four variables (specific humidity at 850 hPa, relative humidity at 850 hPa, air temperature at 2 m, and day of year described as a sinusoidal function) are used in the downscaling. These four variables are closely related to the local maximum and minimum temperature. The air temperature at 2 m and day of year provide the seasonal cycle, and the relative humidity and specific humidity are important in cloud formation, which

influences the solar short-wave radiation absorbed by the surface during the day and outgoing long-wave radiation from the surface during the night.

Results

Evaluation of the downscaled method

Fig. 4-2 compares the probability distributions of the observed and NCEP downscaled daily maximum temperature, minimum temperature, and two other important variables affecting malaria transmission: the average temperature and the diurnal temperature range (DTR). All of the observed probability density functions (PDFs) are well reproduced in the downscaled results with only some small differences.

For the four stations in West Africa, both the observed and NCEP downscaled daily maximum temperature range from about 20 ºC to 45 ºC; the probability peaks at a temperature slightly lower than 40 ºC, with a gentle slope on the left and a sharp slope on the right. The high peak temperatures are mainly because the four stations are located at sub-Saharan region, which is usually dry and cloudless, and easily heated up due to the radiation. For the seven stations in East Africa and one station in West Coastal Africa, the observed and NCEP downscaled temperature range from about 20 ºC to 40 ºC with much narrower PDFs. The PDFs of daily average temperature and minimum temperature are similar to the PDFs of daily maximum temperature, with about 5 ºC and 10 ºC shift towards left separately. The narrowness of the PDFs is probably because the annual cycles of temperature are not as significant as those over West Africa due to the high elevation or coastal location.

For the four stations in West Africa, the observed and NCEP downscaled daily DTR range from about 5 ºC to 25 ºC with probability peaks located at about 12 ºC. For the remaining

eight stations, most DTR probability distributions are similar to those of the West African stations. Station Cotonou has the smallest probability peaks at about 5 ºC because its coastal location and amplitude water vapor tend to reduce the temperature difference between day and night.

Fig. 4-3 compares the observed and NCEP downscaled annual cycles of maximum temperature, minimum temperature, average temperature, and DTR for the 12 stations. The observed annual cycles of all four variables are captured reasonably well by the downscaling.

For the maximum temperature at the four stations in West Africa, there is a larger peak around April of about 40 °C and another smaller peak around October of about 35 °C for both observed and downscaled temperature. The reason for this two-peak pattern is that in the summer season, West Africa is dominated by the Intertropical Convergence Zone, which brings large amount precipitation and reduces the temperature. For the remaining eight stations, the annual cycle of maximum temperature is not as obvious as those in West Africa, with a small peak around February since the wet season comes earlier over East Africa and West Coastal Africa. The annual cycles of the minimum temperatures and average temperatures are similar to those of maximum temperatures, with smaller magnitudes. The DTR annual cycles are not as obvious as the other three variables. Nearly all the stations have annual cycles around 12 ºC with smaller values during the wet seasons, and only exception is Cotonou with DTRs about 8 ºC since it is located at the coast and is more humid than other stations.

Evaluation of the GCM downscaled results

In order to quantitatively evaluate the downscaling of GCM output, the fractional mean square errors (MSEs) are used here. To calculate the fractional MSE, for each station, the variances of the deviation between observed and downscaled (or raw GCM simulated) annual cycles and PDFs are firstly calculated. Then, the ratios between variances of the deviation and

variances of observed annual cycles and PDFs are calculated. Finally, the ratios of the annual cycles and PDFs are averaged to generate the fractional MSE for each station.

Fig. 4-4a shows the regional average (averaged across the 12 stations) fractional MSE from NCEP-downscaled results, GCM-downscaled results, and the raw GCM simulations. The results from raw NCEP data are not shown because there is no daily maximum temperature and minimum temperature in the NCEP data. In the figure, it can be seen that NCEP downscaled results have the smallest fractional MSE 0.03, and the fractional MSEs from the GCMs downscaled results range from 0.22 (IPSL) to 0.38 (MRI) with an average of 0.27. Compared with the downscaled results, the raw GCM simulations have much larger fractional MSEs with the average 1.24. Even the smallest MSE from MPI is larger than 0.8, and the largest MSE from CNRM is almost 2. This means that the variances of the biases from the raw GCM simulations are comparable or even larger than the observed variances, and the downscaling can improve raw GCM simulations besides increasing the spatial resolution.

Fig. 4-4b shows similar results but for all the stations from NCEP-downscaled data, GCM-downscaled data, and raw GCM simulations. The fractional MSEs from NCEP-downscaled results are smaller than 0.1 over all the stations. The MSEs from GCM-downscaled results are much larger, ranging from 0.15 to 0.55, and this means that over most stations, the variances of the biases from GCM-downscaled results are smaller than half of the observed variances. The average downscaled MSE over each station is smaller than the MSE from raw GCM simulations, and this indicates that the downscaling can largely improve the simulations of observed annual cycle and PDF comparing with the raw GCM output.

Validation based on the malaria transmission model criteria

Since the downscaled results are used as the input data to the malaria transmission model, it is very necessary to validate the downscaled results based on the requirements of the malaria transmission model. Temperature is a major factor determining the distribution and incidence of malaria through the affect on the survival or development of both parasite and mosquito (Craig et al., 1999; Ebi et al., 2005). For here, two important threshold values in the malaria transmission model, 35°C for the maximum temperature and 16°C for the minimum temperature are used, because too high temperature will cause high vector population turnover, weak individuals and high mortality, while too low temperature will cause parasite development ceased and longer larval duration (Craig et al., 1999).

Fig. 4-5 compares the observed (blue) and NCEP-downscaled (red) monthly numbers of days with maximum temperature lower than 35 °C and with minimum temperature higher than 16 °C. In this analysis, in order to minimize the influence of missing values, only the months with more than 28 days of observations are used. From Fig. 4-5, it can be found that, for the monthly number of days with maximum temperature lowers than 35 °C, over the stations with obvious annual cycles (Fig. 4-5 a, b, c, d, e, j, k), the downscaling can reproduce the annual cycles well. For the rest of the stations, nearly all the daily maximum temperatures are lower than 35 °C, with only several months with some extremely high temperature, and the downscaling can also capture this anomaly. Similar conclusions can be found for the monthly number of days with minimum temperature higher than 16 °C. This figure shows that the downscaled temperature data is capable to be used to simulate the observed suitability conditions of the malaria transmission over the Central Africa.

Large scale climate variability influence

Previous studies have indicated that large scale climate modes, such as ENSO, have a strong influence on local temperature and precipitation over Africa (Christensen et al., 2007; Ogutu et al., 2007; Wolff et al., 2011).

Table 4-2 show the composite analysis of boreal winter (DJF) monthly average maximum temperature and minimum temperature during strong El Niño and La Niña events for the 12 stations. During La Niña events, the maximum temperature and minimum temperature over the West and West Coastal African stations (No. 1-4 and 12) are usually lower than average, while El Niño events do not show obvious influence over the whole region. The La Niña events induce negative anomalies on minimum temperature over the East African stations (No. 5-11), but not on maximum temperature.

To test the statistical significance of the differences, we apply the student t-test to the four groups of differences in two ways: on all 12 stations and on the five stations over West and West Coastal Africa. For the maximum temperature, the differences are significant at 95% on the west five stations, but not on all 12 stations. For the minimum temperature, the differences are significant at the 95% level on all 12 stations. The significance analysis shows that the ENSO effect on maximum temperature is more significant over West and West Coastal Africa than the whole region. For the minimum temperature, the ENSO effect is more significant over the whole region. This is consistent with the previous research showing that minimum temperature over East Africa is closely correlated with ENSO, while maximum temperatures is not (Ogutu et al., 2007).

Table 4-3 shows the composite analysis of boreal summer (JJA) monthly average maximum temperature and minimum temperature after strong El Niño and La Niña events over the 12 stations. The influences from ENSO are more uniform on summer temperatures than on

winter temperatures. After strong El Niño events, the maximum and minimum temperature anomalies are usually positive, with exceptions over the stations Niamey-Aero, Kericho, and Kilimanjaro for maximum temperature, and exception over Kilimanjaro for minimum temperature. After strong La Niña events, the temperature anomalies are usually negative, with exceptions over the stations Tillabery, Niamey-Aero, and Kilimanjaro for maximum temperature, and over Agadez and Tillabery for minimum temperature. All the anomaly differences are positive, except over Niamey-Aero and Kilimanjaro for the maximum temperature, and over Kilimanjaro for the minimum temperature. One possible reason for these negative differences is that there are too many missing values during the strong El Niño and La Niña seasons. The two groups of differences are significant at 95% level based on the student t-test.

Future temperature changes

Fig. 4-6 shows the future changes in maximum temperature, minimum temperature, average temperature, and DTR for the 12 stations. For the maximum temperature, minimum temperature, and average temperature, the increases over West Africa are about 1.75-2.5 °C, larger than those over East Africa and West Coastal Africa, which are between 1.5-2 °C. The inter-GCM uncertainty, defined as the standard deviation from the ensemble averages, have similar magnitudes of about 1 °C over most stations. For the future DTR changes, the decreases over West Coastal Africa is small with small inter-GCM uncertainty, while the magnitudes of the decreases over West Africa and East Africa are much larger and the inter-GCM uncertainties are also larger than West Coastal Africa.

For boreal summer months (Fig. 4-7), the regional differences are not as obvious as for annual results, except two stations over West Africa show smaller increases for maximum temperature and average temperature. Most stations have maximum temperature, minimum

temperature, and average temperature increases around 2 °C with close inter-GCM uncertainties. The DTR decreases over all East Africa and West Coastal Africa are close to zero, and most inter-GCM uncertainties are about 0.3 °C. Over West Africa, the DTR decreases are all about -0.5 °C with inter-GCM uncertainties about 0.5 °C.

For boreal winter months (Fig. 4-8), the regional differences are more obvious than those in the annual results. Over the West Africa, the maximum temperature, minimum temperature, and average temperature increases are within 2-2.5°C. And over East Africa, the maximum temperature and average temperature increases are around 1.5 °C, while the minimum temperature increase are close to 2 °C. For West Coastal Africa, the temperature increases are all about 2 °C. And the magnitudes of the inter-GCM uncertainties over the three regions are similar to those in annual and summer results. For the DTR changes, the changes over West Africa and West Coastal Africa are around zero with small inter-GCM uncertainties, while the DTR decreasing over East Africa are more obvious since they are close to -0.3°C with much larger inter-GCM uncertainties. These results show that in the future, under the background of global warming, the temperature responses over West Africa are stronger, especially for annual and boreal winter months, and these are consistent with the results of IPCC report (Fig. 11.2, Christensen et al., 2007). There are several aspects that contribute to the larger magnitudes of temperature increases over West Africa. Firstly, the warming will induce more precipitation over the tropical region along the equator, and this will reduce the magnitudes of temperature increase over East Africa and West Coastal Africa. Secondly, the less water availability over West Africa will induce smaller evaporative cooling than those over the West Africa and West Coastal Africa. Thirdly, the thermal capacity over the arid sub-Saharan region is smaller, so the temperature response to the increased radiation will be larger over West Africa. The source of the inter-GCM uncertainties may be due to the uncertainty of the future ENSO projection (Meehl et al., 2007), since the ENSO has strong influence on temperature change over Central Africa as we discussed

in previous section. Moreover, over the whole region, the minimum temperature usually has larger increases than the maximum temperature since the water vapor increase will bring more cloud, which will induce larger temperature increase during the evening through the reflection of long wave radiation and smaller temperature increase during the daytime through the reflection of solar radiation, and this will bring decreases of the DTR.

Conclusion

Using a statistical downscaling method, we generate a set of high-resolution maximum temperature and minimum temperature over the 12 stations in central Africa as the input to a malaria transmission model, and also evaluate the downscaled temperature data with metrics relevant to the malaria transmission model. The downscaling based on NCEP data can reproduce the seasonal cycles of the observed maximum temperature, minimum temperature, average temperature, and DTR, with small fractional MSEs. The fractional MSEs from the downscaled results based on GCM simulations are much smaller than the fractional MSEs from raw GCM simulations, and this indicates that the downscaling can largely improve the raw GCM simulations.

When examining the performance of the downscaling on the monthly number of days with maximum temperature lower than 35 ºC and monthly number of days with minimum temperature higher than 16 ºC, the downscaling can reproduce the temporal variability of these two metrics along with the extreme values.

The ENSO influences on the winter maximum temperature and minimum temperature changes over central Africa are also examined. The results show that strong La Niña events induce the negative winter maximum temperature and minimum temperature anomalies over West Africa and West Coastal Africa, while over East Africa this influence mainly happens on

winter minimum temperature. And for the following summer, strong El Niño events bring positive anomalies to both maximum and minimum temperatures over the whole central Africa, while strong La Niña events bring negative anomalies. When applying student t-test, all the opposite influences between strong El Niño events and La Niña events are significant.

Finally, the future changes of the four metrics between period 2046-2065 and period 1981-2000 are explored. For annual and boreal winter months, the maximum, minimum, and average temperature increases over West Africa are usually larger than those over East Africa and West Coastal Africa. For boreal summer months, the regional differences are not obvious, with the temperature increases about 2°C. The magnitudes of annual and boreal summer DTR decreases over West Africa are larger than those over the other two regions, while for boreal winter months the DTR decreases over East Africa are more obvious.

Table 4-1. The locations and elevations of the 12 stations over Central Africa.

Number	Stations	Nations	Latitude	Longitude	Altitude (m)	Observation time period (year/month)
1	Agadez	Niger	16.97	7.97	505	1976/07-1996/08
2	Tillabery	Niger	14.20	1.45	210	1978/10-1998/09
3	Niamey-Aero	Niger	13.48	2.17	227	1975/03-1998/09
4	Bamako	Mali	12.53	-7.95	381	1977/04-2010/08
5	Moyale	Kenya	3.53	39.03	1097	1983/04-1998/10
6	Kitale	Kenya	1.02	35.00	1875	1982/12-2005/10
7	Kisumu	Kenya	-0.10	34.75	1146	1978/12-2010/04
8	Kericho	Kenya	-0.37	35.35	2184	1987/02-1998/02
9	Embu	Kenya	-0.50	37.45	1493	1979/09-1998/07
10	Garissa	Kenya	-0.47	39.63	147	1980/06-2010/04
11	Kilimanjaro	Tanzania	-3.42	37.07	896	1975/05-2010/04
12	Cotonou	Benin	6.35	2.38	6	1975/07-1998/07

Table 4-2. The composite of the boreal winter (DJF) monthly maximum and minimum temperature anomalies during strong El Niño and La Niña events over the 12 stations. Strong El Niño (La Niña) events are defined as anomalies greater (smaller) than +0.75 (-0.75) standard deviation above the long-term (1951-2008) mean Nino3.4 index. Numbers in bold indicate differences significant at the 95% level.

.NO.	Stations	Tmax in El Niño (°C)	Tmax in La Niña (°C)	Tmax difference (°C)	Tmin in El Niño (°C)	Tmin in La Niña (°C)	Tmin difference (°C)
1	Agadez	**-0.68**	**-1.51**	**0.82**	**-0.42**	**-0.85**	**0.43**
2	Tillabery	**-0.55**	**-1.66**	**1.12**	**-0.03**	**-0.37**	**0.35**
3	Niamey-Aero	**-0.44**	**-0.98**	**0.54**	**-0.30**	**0.36**	**-0.66**
4	Bamako	**-0.03**	**-0.65**	**0.61**	**-0.15**	**-0.40**	**0.25**
5	Moyale	-0.57	-0.23	-0.34	**-0.16**	**-0.14**	**-0.02**
6	Kitale	-0.14	0.07	-0.21	**0.18**	**-0.39**	**0.57**
7	Kisumu	-0.23	0.40	-0.63	**0.13**	**-0.37**	**0.50**
8	Kericho	-0.29	-0.33	0.04	**0.39**	**-0.26**	**0.65**
9	Embu	-0.22	-0.73	0.51	**0.34**	**-0.25**	**0.59**
10	Garissa	-0.28	-0.09	-0.19	**-0.11**	**-0.14**	**0.04**
11	Kilimanjaro	-0.72	0.44	-1.16	**-0.01**	**-0.24**	**0.23**
12	Cotonou	**0.14**	**-0.39**	**0.53**	**-0.16**	**-0.88**	**0.72**
	Average	-0.33	-0.47	0.14	-0.02	-0.33	0.30

Table 4-3. The composite of the boreal summer (JJA) monthly maximum and minimum temperature anomalies during strong El Niño and La Niña events over the 12 stations. Strong El Niño (La Niña) events are defined as anomalies greater (smaller) than +0.75 (-0.75) standard deviation above the long-term (1951-2008) mean Nino3.4 index. Numbers in bold indicate differences significant at the 95% level.

NO.	Stations	Tmax in El Niño (°C)	Tmax in La Niña (°C)	Tmax difference (°C)	Tmin in El Niño (°C)	Tmin in La Niña (°C)	Tmin difference (°C)
1	Agadez	**0.37**	**-0.01**	**0.38**	**0.21**	**0.16**	**0.05**
2	Tillabery	**0.27**	**0.15**	**0.12**	**0.22**	**0.13**	**0.09**
3	Niamey-Aero	**-0.01**	**0.18**	**-0.19**	**0.14**	**-0.10**	**0.24**
4	Bamako	**0.13**	**-0.20**	**0.32**	**0.17**	**-0.17**	**0.34**
5	Moyale	**0.04**	**-0.92**	**0.96**	**0.08**	**-0.53**	**0.61**
6	Kitale	**0.11**	**-0.21**	**0.32**	**0.23**	**-0.22**	**0.45**
7	Kisumu	**0.11**	**-0.18**	**0.29**	**0.19**	**-0.16**	**0.35**
8	Kericho	**-0.01**	**-0.49**	**0.48**	**0.10**	**-0.28**	**0.38**
9	Embu	**0.26**	**-0.78**	**1.04**	**0.15**	**-0.39**	**0.54**
10	Garissa	**0.26**	**-0.08**	**0.34**	**0.14**	**-0.08**	**0.22**
11	Kilimanjaro	**-0.16**	**0.03**	**-0.18**	**-0.27**	**-0.14**	**-0.14**
12	Cotonou	**0.12**	**-0.12**	**0.25**	**0.21**	**-0.30**	**0.50**
	Average	0.12	-0.22	0.34	0.13	-0.17	0.30

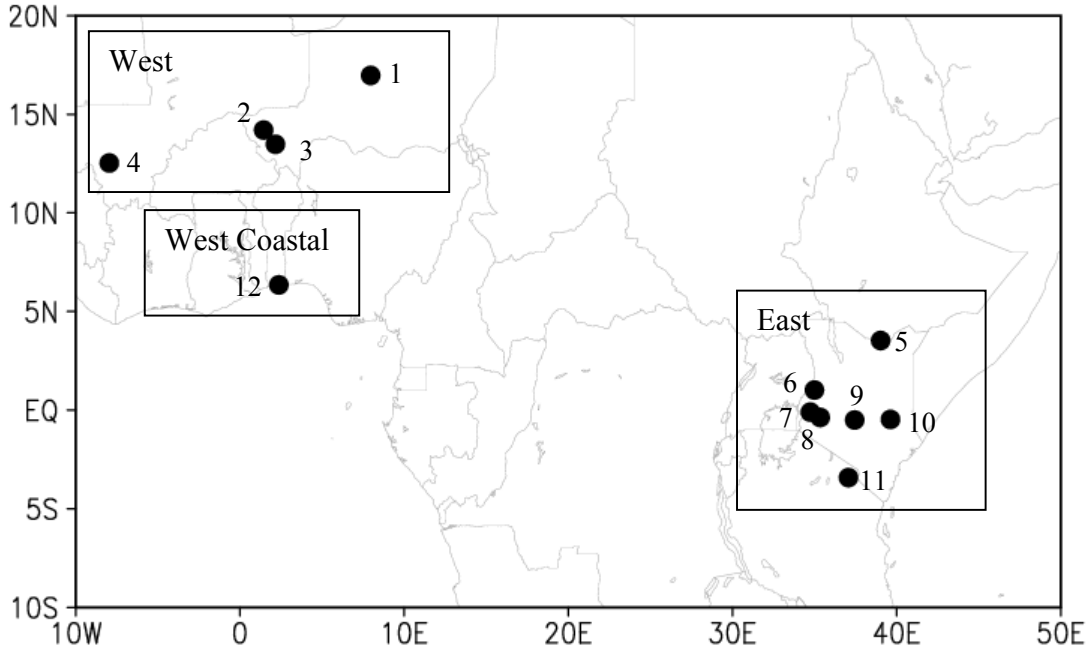

Figure 4-1. The locations of the 12 stations and the three climate regions.

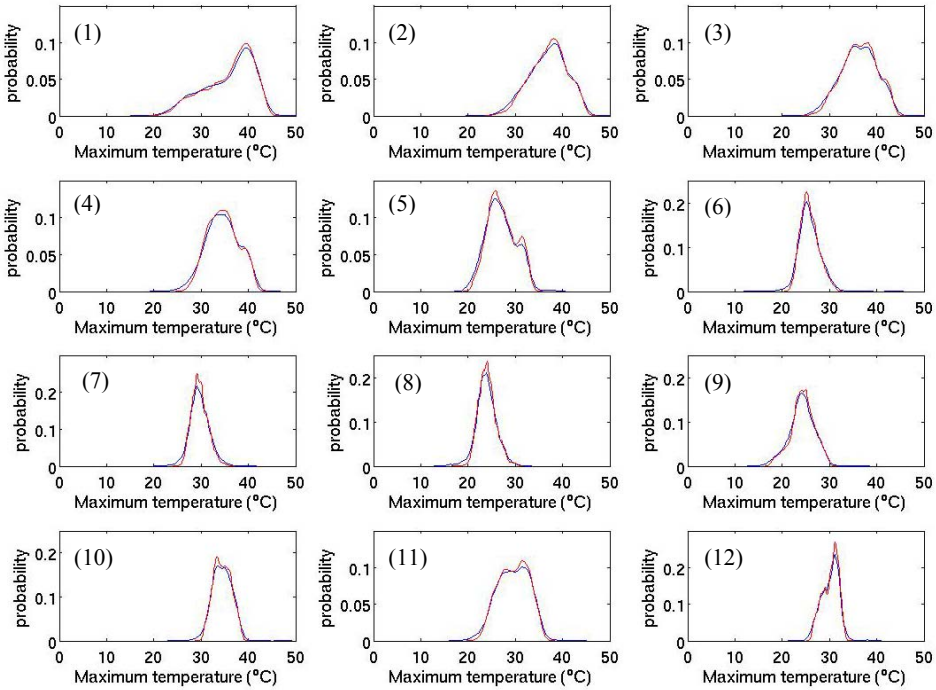
(1)
(2)
(3)
(4)
(5)
(6)
(7)
(8)
(9)
(10)
(11)
(12)
probability
Maximum temperature (°C)

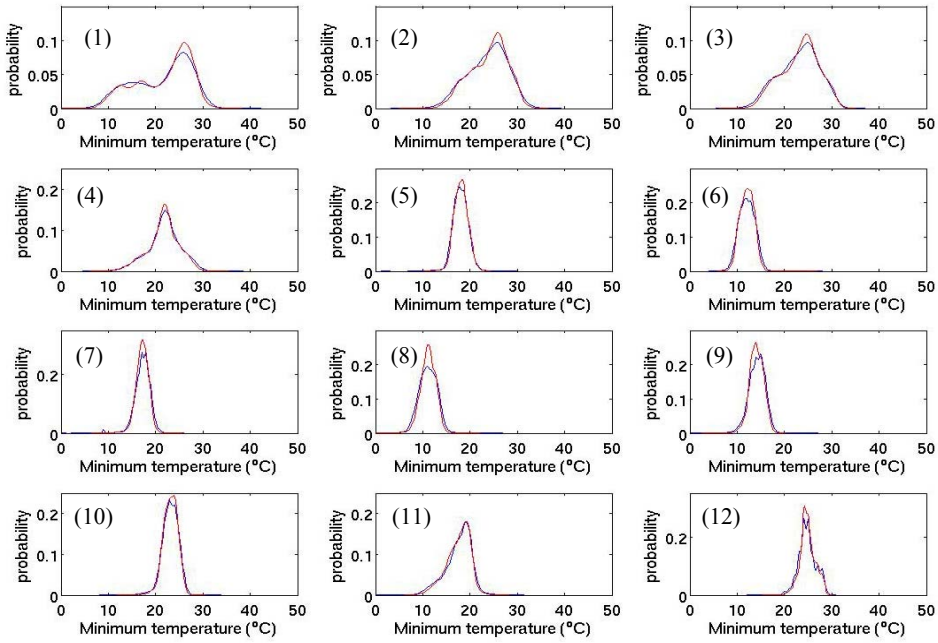
(1)
(2)
(3)
(4)
(5)
(6)
(7)
(8)
(9)
(10)
(11)
(12)
probability
Minimum temperature (°C)

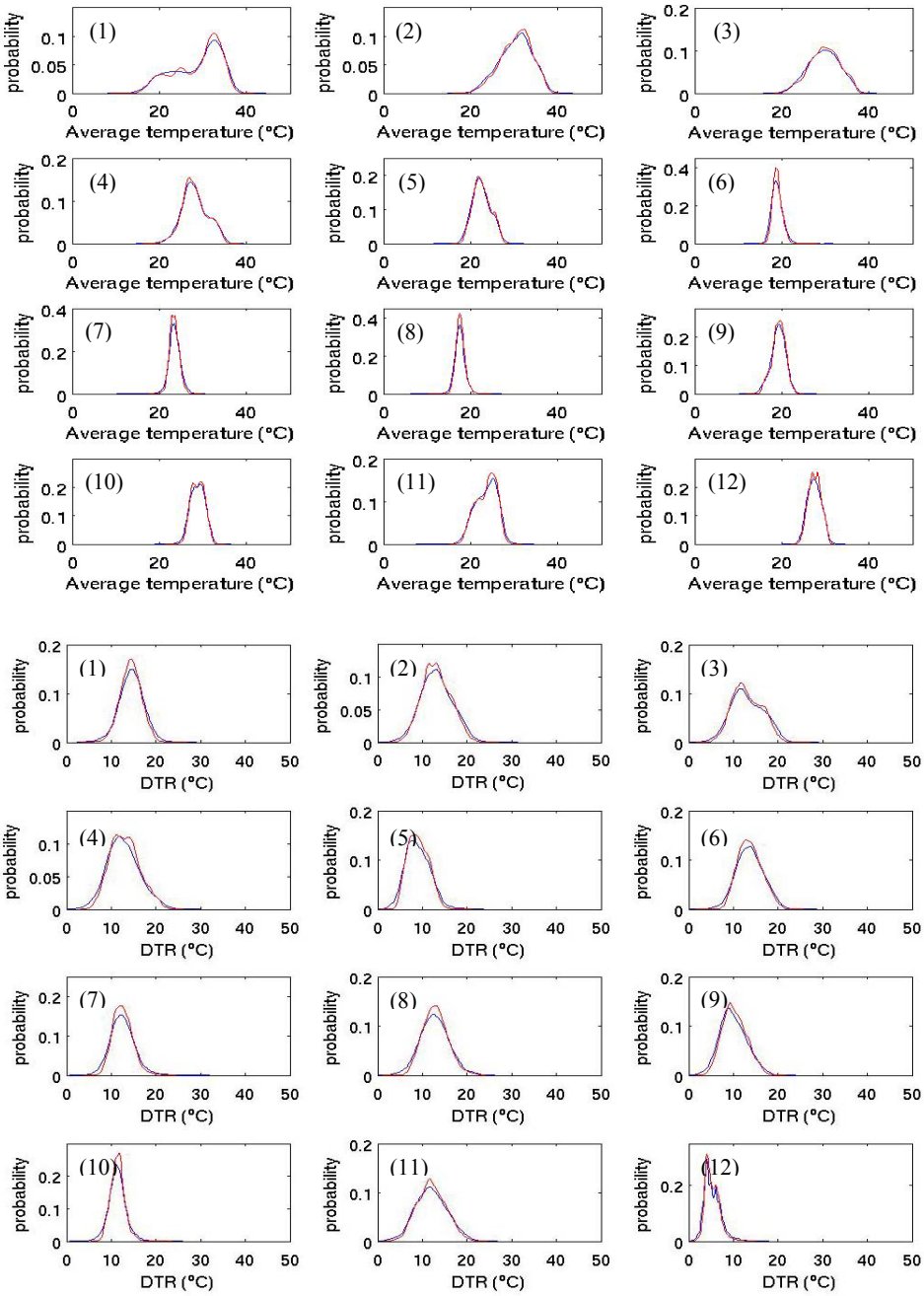

Figure 4-2. The observed (blue) and NCEP downscaled (red) probability distributions of daily maximum temperatures, minimum temperatures, average temperatures, and diurnal temperature ranges (DTRs) over the 12 stations. The vertical scales are different in order to fit the results. The labels are marked on the results of maximum temperature; the other parts of results follow the same station order.

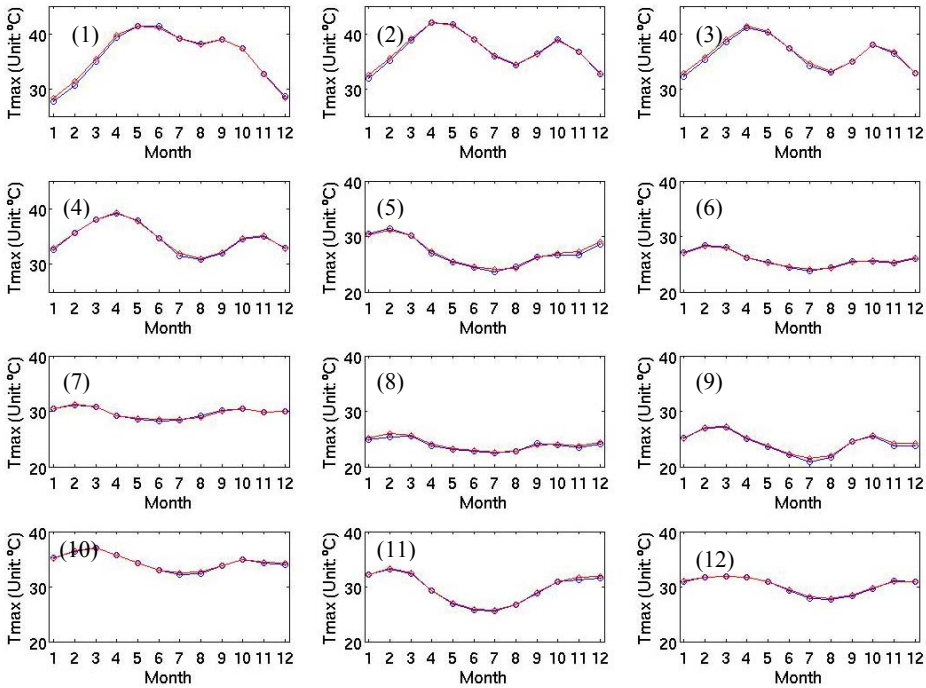
(1)
(2)
(3)
(4)
(5)
(6)
(7)
(8)
(9)
(10)
(11)
(12)
Tmax (Unit:°C)
Month

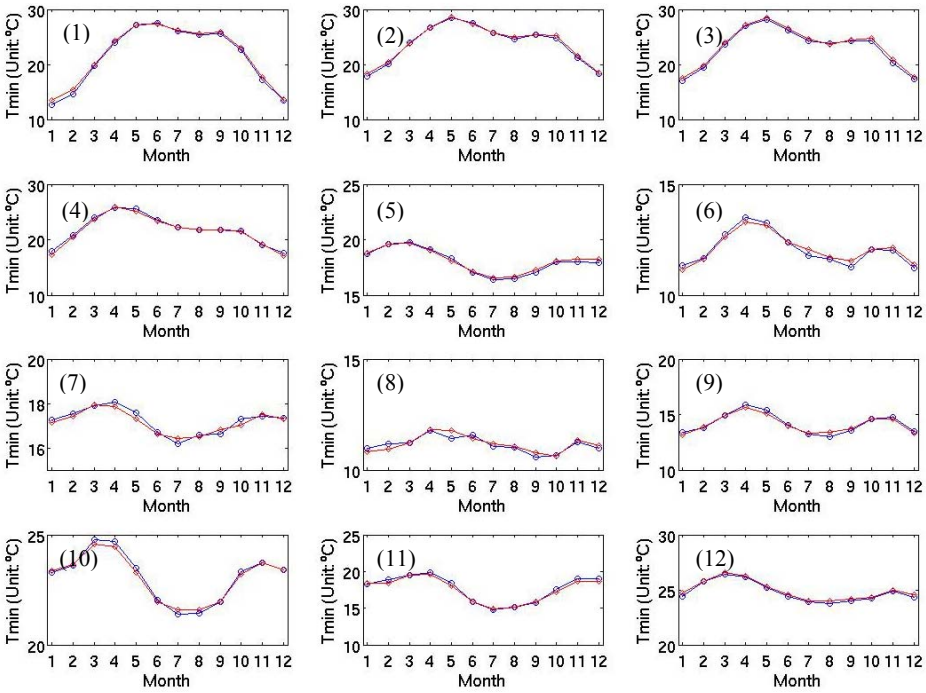
(1)
(2)
(3)
(4)
(5)
(6)
(7)
(8)
(9)
(10)
(11)
(12)
Tmin (Unit:°C)
Month

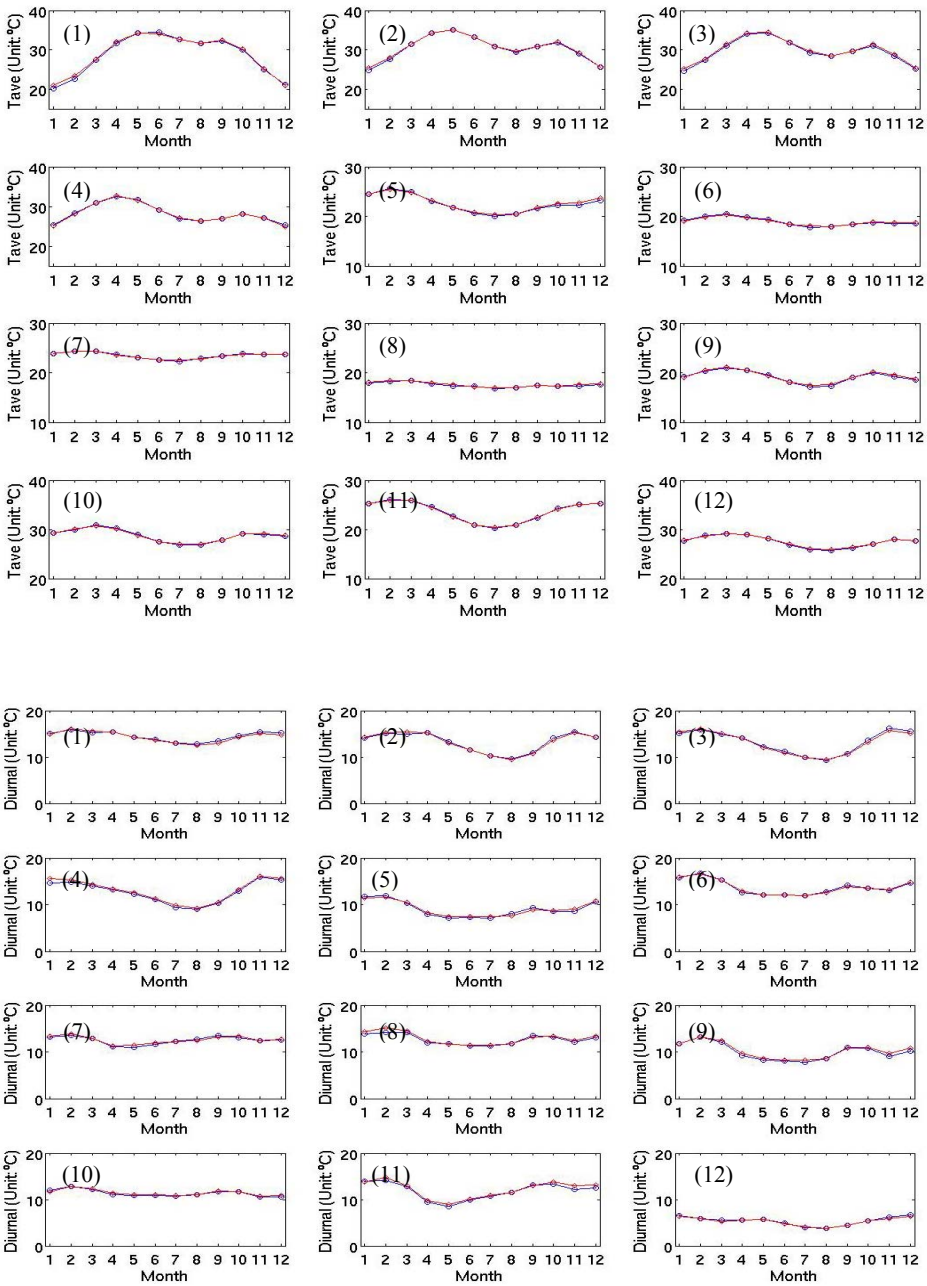

Figure 4-3. Comparison of the observed (blue) and NCEP downscaled (red) annual cycles of the maximum temperature, minimum temperature, average temperature, and DTR over the 12 stations (Unit: °C). The vertical scales are different in order to fit the results. The labels are marked on the results of maximum temperature, and the rest parts of results follow the same station order.

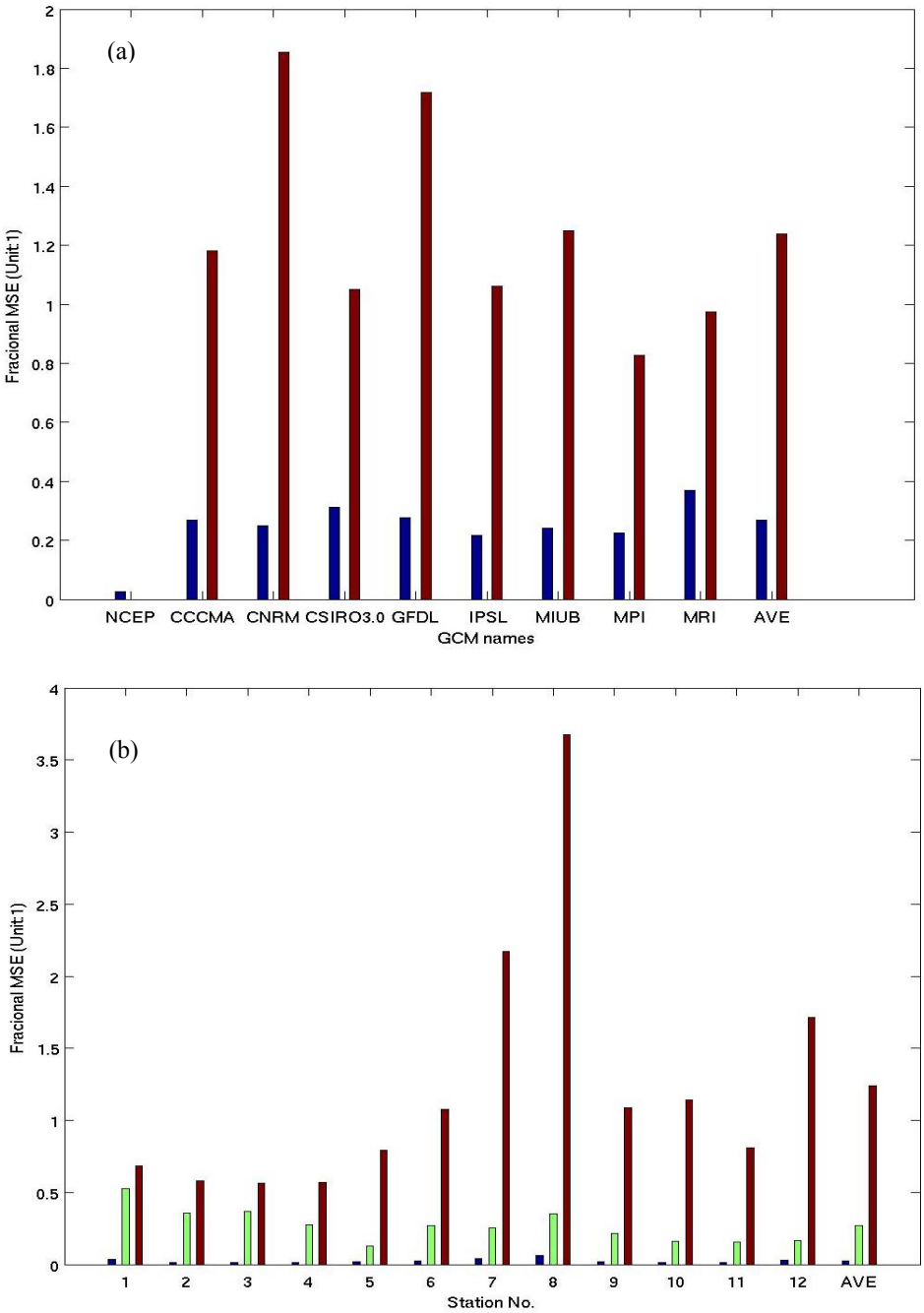

Figure 4-4. (a) The regional average (averaged across the 12 stations) fractional MSE from downscaled (blue) and raw simulated (red) annual cycles and PDFs from NCEP data and GCMs, and the average across the eight GCMs. (b) The average fractional MSE from NCEP-downscaled data (blue), GCM-downscaled (green), and raw GCM simulations (red) over the 12 stations, and the average across the 12 stations.

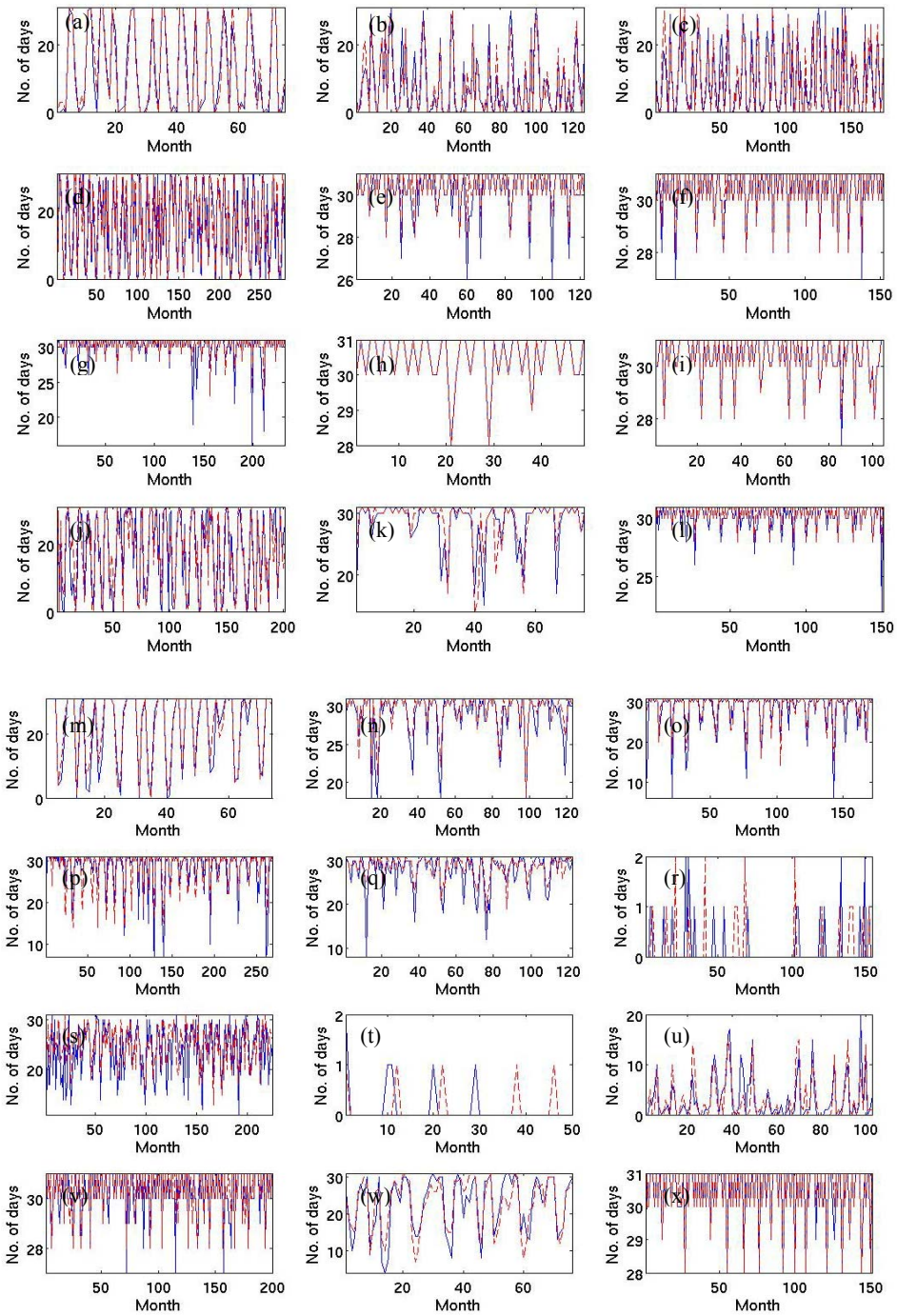

Figure 4-5. The observed (blue) and NCEP-downscaled (red) monthly number of days with maximum temperature lower than 35 °C (a-l) and with minimum temperature higher than 16 °C (m-x) (Unit: day). The vertical scales are different in order to fit the results.

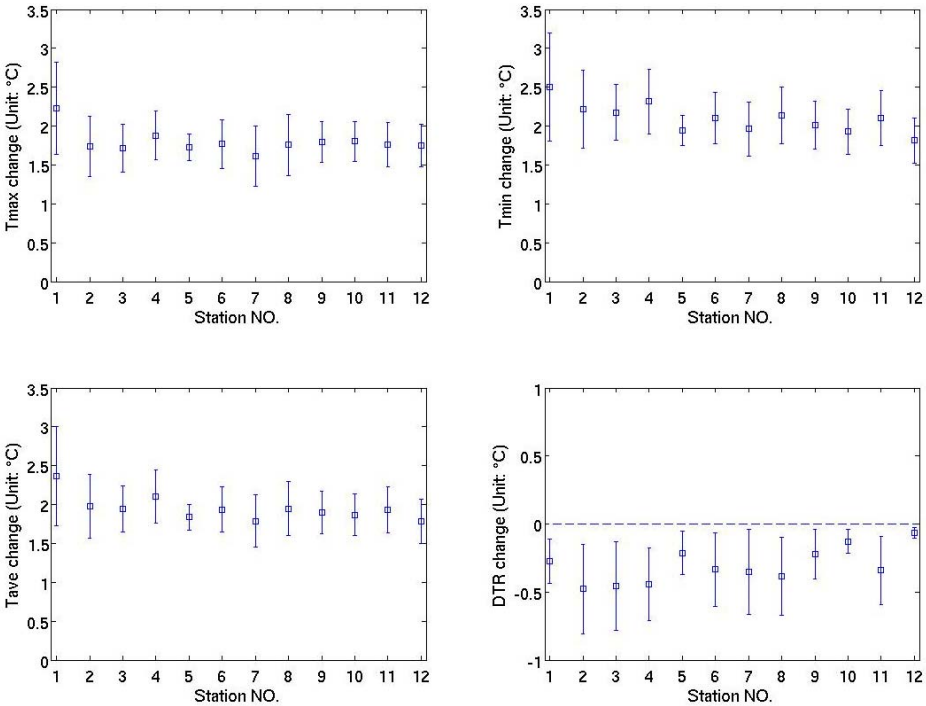

Figure 4-6. The future changes of the annual average maximum temperature, minimum temperature, average temperature, and DTR between the period 2046-2065 and the period 1981-2000 for each of the 12 stations (Unit: °C).

The squares are the ensemble average across the eight GCMs, and the whiskers are the inter-GCM uncertainties.

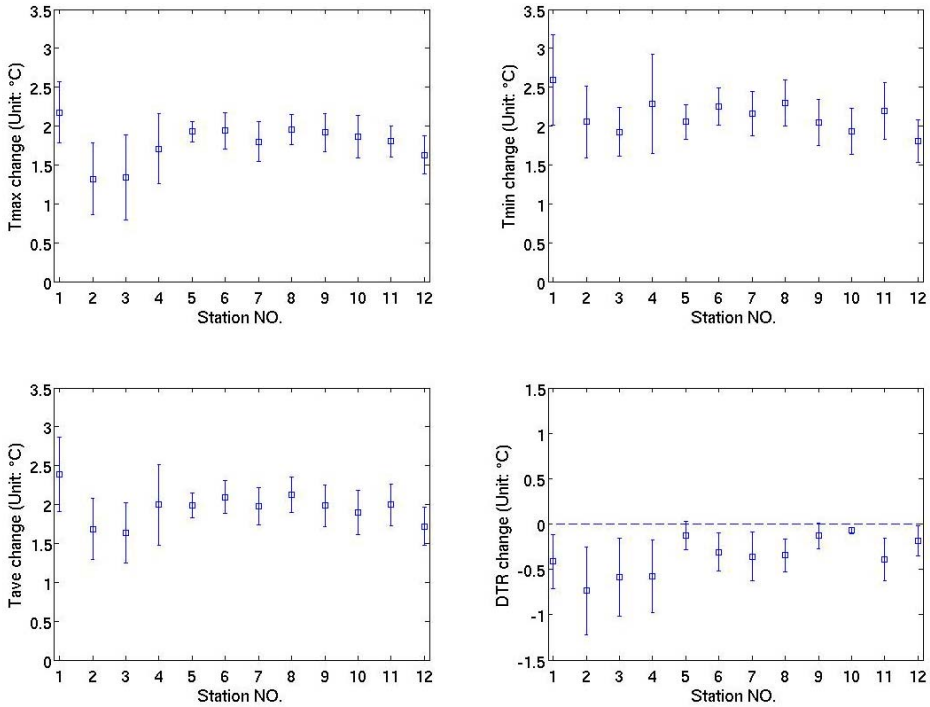

Figure 4-7. Similar to Fig. 4-6, but the boreal summer months (Unit: °C).

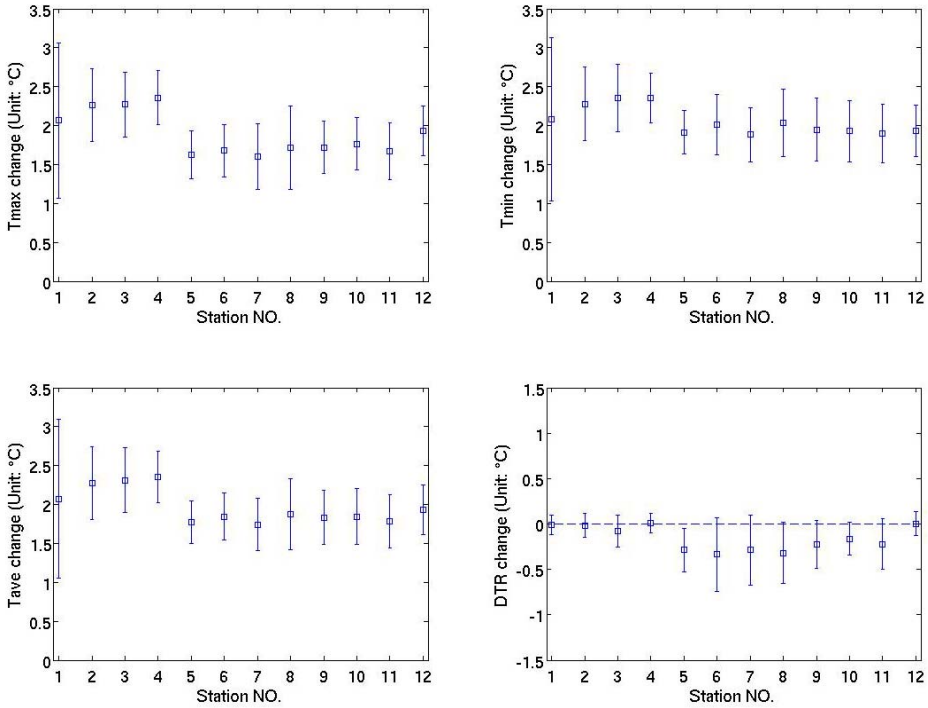

Figure 4-8. Similar to Fig. 4-6, but the boreal winter months (Unit: °C).

Chapter 5

Conclusion

Using a statistical downscaling method based on Self-Organizing Maps (SOMs), the probabilistic estimations of regional climate changes over Mid-Atlantic region and Central Africa are generated and evaluated. Firstly, the historical precipitation changes over Pennsylvania in the Mid-Atlantic regional of U.S. are reproduced and validated through using the large-scale atmospheric states from NCEP data and nine GCM simulations. When applying the downscaling approach to NCEP atmospheric observations, it is demonstrated that the downscaled precipitation can reproduce a variety of observed precipitation characteristics reasonably.

For the downscaled precipitation from the nine GCM simulations, it is shown that, although there are still some biases between the observed and downscaled precipitation statistics, the biases are considerably reduced through the downscaling procedure. Moreover, the downscaling does improve the inter-GCM consistency, and this suggests that bypassing the individual model's own varying precipitation parameterization schemes can yield more robust estimates of the distribution of local precipitation from the models.

When using the statistical downscaling method to project the future precipitation changes for the period 2046-2065 over Pennsylvania, it is firstly found that the downscaling method is able to capture the prevailing synoptic circulation patterns that characterize the warmer climate of the mid-21st century through changes of the SOM frequency and associated quantization error distributions, and this suggests that our SOM-based downscaling method is capable to project future precipitation changes.

For the annual precipitation, both the raw GCM simulations and downscaled results suggest an overall increasing trend. For summer precipitation, the spread among models is really

large for both raw GCM simulations and downscaled results, and the ensemble average of raw GCM simulations predicts increase, while the ensemble average of downscaled results predicts decrease. For winter precipitation, the agreements both among GCMs and downscaling and raw GCM precipitation are much higher, since most GCMs predict increases in winter precipitation in both raw GCM simulations and downscaling, with an increasing ensemble average. When examining the influence on downscaled winter precipitation changes from the large scale climate variability NAO, it is found that there is a tendency for greater winter precipitation increases in those models with less positive-trending NAO changes, and this is consistent with the negative relationship between winter precipitation and NAO drawn from the observation.

In order to examine the sensitivity of future precipitation changes due to the atmospheric water vapor increases associated with global warming, we tested two different downscaling approaches: using only relative humidity or both relative and specific humidity variables in calibrating relationships between atmospheric variability and precipitation. Over the historical period, both downscaling approaches can generate similarly skillful precipitation statistics, with no significant difference. While, for the future precipitation projections, the downscaling using both relative humidity and specific humidity always yields larger positive precipitation projections than the downscaling using only relative humidity. This suggests that, in the procedure of training SOMs, the inclusion of specific humidity, which increases sharply with temperature via the Claussius-Clapeyron equation, will induce larger sensitivity to the increased water vapor content of the atmosphere in a warming atmosphere.

In this study, we also introduce a new ensemble average method for the downscaled precipitation estimates. The new ensemble average method uses the quantization errors as an evaluation of GCM performances in simulating the synoptic scale circulations, and it is shown that this new method does reduce the inter-GCM uncertainty seen in projections based on the raw

GCM precipitation field, and will in principle allow for reduced uncertainty in probabilistic projections of future precipitation changes.

Finally, the probabilistic estimations of maximum temperature and minimum temperature changes over the 12 stations in Central Africa as the input to the malaria transmission mode are generated using the statistical downscaling method, and also validated based on the requirement of the malaria transmission model. The downscaling based on NCEP data can reproduce the seasonal cycles of the observed maximum temperature, minimum temperature, average temperature, and DTR, with small fractional MSE. The fractional MSEs from the downscaled results based on GCM simulations are much smaller than the fractional MSEs from raw GCM simulations, and this indicates that the downscaling can largely improve the raw GCM simulations. And both the downscaling and raw GCM simulations show better performances over West Africa and West Coastal Africa than East Africa.

When examining the performance of the NCEP downscaled results on the monthly number of days with maximum temperature lower than 35 ºC and minimum temperature higher than 16 ºC, the downscaling can reproduce the temporal variability and extreme values. And the ENSO influences on the maximum temperature and minimum temperature changes show that strong La Niña events will induce the negative winter maximum temperature and minimum temperature anomalies over West Africa and West Coastal Africa, while over East Africa this influence mainly happens on minimum temperature. While for the following summer, the ENSO has similar influences on maximum temperature and minimum temperature, and the temperature anomaly differences between strong El Niño events and La Niña events are significant for the whole central Africa.

The future changes of the maximum temperature, minimum temperature, and average temperature between period 2046-2065 and period 1981-2000 show that the temperature variables show increasing trends for annual and both boreal summer and winter months. The

temperature increases over West Africa are significantly larger than those increases over East Africa and West Coastal Africa for annual and boreal winter months, while the regional differences are not obvious in boreal summer months. For the DTR changes, West Africa shows large decreasing trends for annual and summer months, and small increasing trends for winter months. East Africa shows smaller decreasing trends for annual, summer and winter months. For the West Coastal Africa, there are always decreasing trends for annual and both summer and winter months.

Therefore, the downscaled projections of future regional climate changes are more reliable than the projections from raw GCM simulations besides the higher resolution, and can be used as credible input to the hydrological and malaria transmission models to simulate the future streamflow over Mid-Atlantic region and malaria transmission conditions over Central Africa under the background of global warming. The frameworks for probabilistic projections of streamflow relevant thermoelectric power plant management and human health improvements will be provided to the decision makers to develop and evaluate the adaptations and mitigations of future anthropogenic climate changes and the corresponding influences.

BIBLOGRAPHY

Barnston, A. G., and R. E. Livezey, 1987: Classification, seasonality and persistence of low-frequency atmospheric circulation patterns. *Mon. Wea. Rev*., 115, 1083-1126

Barron, E. J., 2009: Beyond climate science. *Science*, **326**, 643, doi: 10.1126/science.1179807

Benestad, R. E., 2002a: Empirically downscaled temperature scenarios for northern Europe based on a multi-model ensemble. *Clim. Res.*, **21**, 105-125

Benestad, R. E., 2002b: Empirically downscaled multimodel ensemble temperature and precipitation scenarios for Norway. *J. Climate*, **15**, 3008-3027

Benestad, R. E., 2004: Tentative probabilistic temperature scenarios for northern Europe. *Tellus*, **56A**, 89-101

Benestad, R. E., 2005: Climate change scenarios for northern Europe from multi-model IPCC AR4 climate simulations. *Geophy. Res. Lett.*, **32**, L17704, doi: 10.1029/2005GL023401

Brekke, L., Dettinger, M., Maurer, E., Anderson, M., 2008. Significance of model credibility in estimating climate projection distributions for regional hydroclimatological risk assessments. *Clim. Change*, **89**, 371-394

Cai, W., P. V. Rensch, T. Cowan, and A. Sullivan, 2010: Asymmetry in ENSO teleconnection with regional rainfall, its multidecadal variability, and impact. *J. Climate*, **23**, 4944-4955

Carter, Suzanne, 2007: Approaches to quantifying and reducing uncertainty in GCMs over southern Africa. Unpublished Ph.D. thesis, University of Cape Town.

Cavazos, T., 1999: Large-scale circulation anomalies conducive to extreme precipitation events and derivation of daily rainfall in northeastern Mexico and southeastern Texas. *J. Climate*, **12**, 1506-1523.

Chen, M. D., D. Pollard, and E. J. Barron, 2003: Comparison of future climate change over North America simulated by two regional models. *J. Geophys. Res.*, **108**, D12, 4348, doi: 10.1029/2002JD002738

Christensen, J.H., B. Hewitson, A. Busuioc, A. Chen, X. Gao, I. Held, R. Jones, R.K. Kolli, W.-T. Kwon, R. Laprise, V. Magaña Rueda, L. Mearns, C.G. Menéndez, J. Räisänen, A. Rinke, A. Sarr and P. Whetton, 2007: Regional Climate Projections. In: *Climate Change 2007: The Physical Science Basis. Contribution of Working Group I to the Fourth Assessment Report of the Intergovernmental Panel on Climate Change* [Solomon, S., D. Qin, M. Manning, Z. Chen, M. Marquis, K.B. Averyt, M. Tignor and H.L. Miller (eds.)]. Cambridge University Press, Cambridge, United Kingdom and New York, NY, USA.

Collins, M., 2000: Understanding uncertainties in the response of ENSO to greenhouse warming. *Geophy. Res. Lett.*, **27**, 3509-3512

Collins, M., S. An, W. Cai, et al., 2010: The impact of global warming on the tropical Pacific Ocean and El Niňo. *Nature Geoscience*, **3**, 391-397

Craig, M. H., R. W. Snow, and D. le Sueur, 1999: A climate-based distribution model of malaria transmission in sub-Saharan Africa. *Parasitol Today*, **15**, 105-111

Crane, R. G. and B. C. Hewitson, 1998: Double CO_2 precipitation changes for the Susquehanna Basin: down-scaling from the Genesis general circulation model. *Int. J. Climatol.*,**18**, 65-76.

----, and ----, 2003: Clustering and upscaling of station precipitation records to regional patterns using self-orginizing maps (SOMs). *Clim. Res.*, **25**, 95-107.

Deser, C., 2000: On the teleconnectivity of the "Arctic Oscillation". *Geophys. Res. Lett.*, **27**, 779-782.

Dong, B, R. T. Sutton, T. Woollings, 2010: Changes of interannual NAO variability in response to greenhouse gases forcing. *Clim. Dyn.*, **35**, DOI: 10.1007/s00382-010-0936-6

Ebi, K. L., J. Hartman, N. Chan, J. McConnell, M. Schlesinger, and J. Weyant, 2005: Climate suitability for stable malaria transmission in Zimbabwe under different climate change scenarios. *Climatic Change*, **73**, 375-393

Efron, B., 1982: *The Jackknife, the Bootstrap, and other resampling plans*. The Society for Industrial and Applied Mathematics, 92.

Fitzpatrick, E. A., and A. Krishnan, 1967: A first-order Markov model for assessing rainfall discontinuity in central Australia. *Theor. Appl. Climatol.*, **15**, 242-259

Frederick, K. D., and P. H. Gleick, 1999: Water and global climate change: Potential impacts on U.S. water resources. Pew Center on Global Climate Change, Washington D.C., USA

Frei, C., J. H. Christensen, M. Déqué, D. Jacob, R. G. Jones, and P. L. Vidale, 2003: Daily precipitation statistics in regional climate models: evaluation and intercomparison for the European Alps. *J. Geophys. Res.*, **108**, D3, doi: 10.1029/2002HD002287

Gallus, W. A., and M. Segal, 2004: Does increased predicted warm-season rainfall indicate enhanced likelihood of rain occurrence? *Wea. Forecasting*, **19**, 1127-1135

Guilyardi, E., 2006: El Niño-mean state-seasonal cycle interactions in a multi-model ensemble. *Climate Dyn.*, **26**, 329-348

Han, J., and J. O. Roads, 2004: U. S. climate sensitivity simulated with the NCEP regional spectral model. *Clim. Change*, **62**, 115-154

Hanssen-Bauer, I., C. Achberger, R. E. Benestad, D. Chen, E. J. Førland, 2005: Statistical downscaling of climate scenarios over Scandinavia. *Clim. Res.*, **29**, 255-268

Harvell, C. D., C. E. Mitchell, J. R. Ward, S. Altizer, A. P. Dobson, R. S. Ostfeld, and M. D. Samuel, 2002: Climate warming and disease risks for terrestrial and marine biota. *Science*, **296**, 2158-2162

Hayhoe, K., C. P. Wake, T. G. Huntington, L. Luo, M. D. Schwartz, J. Sheffield, E. Wood, B. Anderson, J. Bradbury, A. Degaetano, T. J. Troy, D. Wolfe, 2007: Past and future changes in

climate and hydrological indicators in the U.S. Northeast. *Climate Dyn.*, **27**, DOI 10.1007/s00382-006-0187-8

Hayhoe, K, and co-authors, 2008: Regional climate change projections for the Northeast USA. *Mitig. Adapt. Strat. Glob. Change*, **13**, 425-436

Hershfield, D. M., 1971: The frequency of dry periods in Maryland. *Chesapeake Science*, **12**, 72-84

Hewitson, B. C. and R. G. Crane, 1992: Regional-scale climate prediction from the GISS GCM. *Palaeogeography, Palaeoclimatology, Palaeoecology (Global and Planetary Change Section)*, **97**, 249- 267.

----, and ----, 1992: Regional climates in the GISS global circulation model: synoptic-scale circulation. *J. Climate*, **5**, 1002-1011.

----, and ----, 1992: Large-scale atmospheric control on local precipitation in tropical Mexico. *Geophy. Res. Lett.*, **19**, 1835-1838.

----, and ----, 1996: Climate downscaling: techniques and application. *Clim. Res.*, **7**, 85-95.

----, and ----, 2002: Self-organizing maps: applications to synoptic climatology. *Clim. Res.*, **22**, 13-26.

----, and ----, 2006: Consensus between GCM climate change projections with empirical downscaling: precipitation downscaling over South Africa. *Int. J. Climatol.*, **26**, 1315-1337.

Hurrell, J. W., 1995: Decadal trends in the North Atlantic Oscillation: regional temperatures and precipitation. *Science*, **269**, 676-679

Hurrell, J. W., Y. Kushnir, G. Ottersen, and M. Visbeck, 2003: An overview of the North Atlantic Oscillation. *The North Atlantic Oscillation: climatic significance and environmental impact*, J. W. Hurrell, Y. Kushnir, G. Ottersen, and M. Visbeck Eds., Geophysical monograph 134, 1-35

IPCC, 2001: *Climate Change 2001: The Scientific Basis. Contribution of Working Group I to the Third Assessment Report of the Intergovernmental Panel on Climate Change* [Houghton, J.T., et al. (eds.)]. Cambridge University Press, Cambridge, United Kingdom and New York, NY, USA, 881 pp.

Knutson, T. R., S. Manabe, and D. Gu, 1997: Simulated ENSO in a global coupled ocean-atmosphere model: multidecadal amplitude modulation and CO2 sensitivity. *J. Climate*, **10**, 138-161

Kohonen, T., 1989: Self-organization and associative memory, 3rdedn. Springer-Verlag, Berlin.

----, 1995: Self-organizing maps. Spring-Verlag, Heidelberg.

Larkin, N. K., and D. E. Harrison, 2005: On the definition of El Niño and associated seasonal average U.S. weather anomalies. *Geophy. Res. Lett.,* **32**, L13705, doi: 10.1029/2005GL022738

Larkin, N. K., and D. E. Harrison, 2005: Global seasonal temperature and precipitation anomalies during El Niño autumn and winter. *Geophy. Res. Lett.*, **32**, L16705, doi: 10.1029/2005GL022860

Li, W., L. Li, R. Fu, Y. Deng, and H. Wang, 2011: Changes to the North Atlantic Subtropical High and its role in the intensification of summer precipitation variability in the southeastern United States. *J. Climate*, **24**, 1499-1506

Liang, X., E. F. Wood, and D. P. Lettenmaier, 1996: Surface soil moisture parameterization of the VIC-2L model: Evaluation and modification. *Global Plan. Change*, **13**, 195-206

----, ----, and ----, 1999: Modeling ground heat flux in land surface parameterization schemes. *J. Geophys. Res.*, **104**, 9581-9600

López-Moreno, J. I., and S. M. Vicente-Serrano, 2008: Positive and negative phases of the wintertime North Atlantic Oscillation and drought occurrence over Europe: a multitemporal-scale approach. *J. Climate*, **21**, 1220-1243

Liu, Z., S. Vavrus, F. He, N. Wen, and Y. Zhong, 2005: Rethinking tropical ocean response to global warming: the enhanced equatorial warming. *J. Climate*, 18, 4684-4700

Maurer, E. P., 2007: Uncertainty in hydrologic impacts of climate change in the Sierra Nevada, California, under two emission scenarios. *Climatic Change*, **82**: 309-325

Meehl, G. A., H. Teng, and G. Branstator, 2006: Future changes of El Niño in two global coupled climate models. *Climate Dyn.*, **26**, 549-566

Meehl, G.A., T.F. Stocker, W.D. Collins, P. Friedlingstein, A.T. Gaye, J.M. Gregory, A. Kitoh, R. Knutti, J.M. Murphy, A. Noda, S.C.B. Raper, I.G. Watterson, A.J. Weaver and Z.-C. Zhao, 2007: Global Climate Projections. In: *Climate Change 2007: The Physical Science Basis. Contribution of Working Group I to the Fourth Assessment Report of the Intergovernmental Panel on Climate Change* [Solomon, S., D. Qin, M. Manning, Z. Chen, M. Marquis, K.B. Averyt, M. Tignor and H.L. Miller (eds.)]. Cambridge University Press, Cambridge, United Kingdom and New York, NY, USA.

Meehl, G. A., and H. Teng, 2007: Multi-model changes in El Niño teleconnections over North America in a future warmer climate. *Clim. Dyn.*, **29**, 779-790

Miettinen A., N. Koc, I. R. Hall, F. Godtliebsen, and D. Divine, 2011: North Atlantic sea surface temperatures and their relation to the North Atlantic Oscillation during the last 230 years. *Clim. Dyn.*, **36**, 533-543

Miller, R.L., G.A. Schmidt, and D.T. Shindell, 2006: Forced annular variations in the 20th century Intergovernmental Panel on Climate Change Fourth Assessment Report models. *J. Geophys. Res.*, **111**, D18101, doi: 10.1029/2005JD006323.

Merryfield, W. J., 2006: Changes to ENSO under CO2 doubling in a multimodel ensemble. *J. Climate*, **19**, 4009-4027

Mo, K., 2010: Interdecadal modulation of the impact of ENSO on precipitation and Temperature over the United States. *J. Climate*, **23**, 3639-3656

New, M., and M. Hulme, 2000: Representing uncertainty in climate change scenarios: a Monte-Carlo approach. *Integr. Assess. J.*, **1**, 203-213

Ning, L., M. E. Mann, R. Crane, and T. Wagener, 2012a: Probabilistic projections of climate change for the Mid-Atlantic region of the United States - Validation of precipitation downscaling during the historical era. *J. Climate,* **25**, 509-526

Ning, L., M. E. Mann, R. Crane, T. Wagener, R. G. Najjar Jr., R. Singh, 2012b: Probabilistic projections of anthropogenic climate change impacts on precipitation for the Mid-Atlantic region of the United States. *J. Climate,* doi:10.1175/JCLI-D-11-00565.1, in press

Ning, L., and Y. Qian, 2009: Interdecadal change of extreme precipitation over South China and its mechanism. *Adv. Atmos. Sci.*, **26**, 109-118

Ogutu, J. O., H. –P. Piepho, H. T. Dublin, N. Bhola, and R. S. Reid, 2007: El Niño- Southern Oscillation, rainfall, temperature and normalized difference vegetation index fluctuations in the Mara-Serengeti ecosystem. *Afr. J. Ecol.*, **46**, 132-143

Paaijmans, K. P., S. Blanford, A. S. Bell, J. I. Blanford, A. F. Read, and M. B. Thomas, 2010: Influence of climate on malaria transmission depends on daily temperature variation. *Proc. Natl. Acad. Sci.,* **107**, 15135-15139

Patz, J. A., and S. H. Olson, 2006: Malaria risk and temperature: Influences from global climate change and local land use practices. *Proc. Natl. Acad. Sci.*, **103**, 5635-5636

Philip, S., and G. J. van Oldenborgh, 2006: Shifts in ENSO coupling processes under global warming. *Geophy. Res. Lett.*, **33**, L11704, doi:10.1029/2006GL026196

Plummer, D. A., D. Caya, A. Frigon, H. Côté, M. Giguère, D. Paquin, and S. Biner, R. Harvey, and R. De Elia, 2006: Climate and climate change over North America as simulated by the Canadian RCM. *J. Climate*, **19**, 3112-3132

Randall, D.A., R.A. Wood, S. Bony, R. Colman, T. Fichefet, J. Fyfe, V. Kattsov, A. Pitman, J. Shukla, J. Srinivasan, R.J. Stouffer, A. Sumi, and K.E. Taylor, 2007: Climate Models and

Their Evaluation. In: *Climate Change 2007: The Physical Science Basis*. *Contribution of Working Group I to the Fourth Assessment Report of the Intergovernmental Panel on Climate Change* [Solomon, S., D. Qin, M. Manning, Z. Chen, M. Marquis, K.B. Averyt, M. Tignor and H.L. Miller (eds.)]. Cambridge University Press, Cambridge, United Kingdom and New York, NY, USA.

Reusch, D. B., and R. B. Alley, 2007: Antarctic sea ice: a self-organizing map-based perspective. *Annals of Glaciology*, **46**, 391-396.

----, ----, and B. C. Hewitson, 2007: North Atlantic climate variability from a self-organizing map perspective. *J. Geophys. Res.,* **112**, D02104, doi: 10.1029/2006JD007460

Rodó, X., E. Baert, F. A. Comin, 1997: Variations in seasonal rainfall in Southern Europe during the present century: relationships with the North Atlantic Oscillation and the El Niño-Southern Oscillation. *Clim. Dyn.*, **13**, 275-284

Ropelewski, C. F., and M. S. Halpert, 1986: Northern American precipitation and temperature patterns associated with El Niño/ Southern Oscillation (ENSO). *Mon. Wea. Rev.*, **114**, 2352-2362

Ropelewski, C. F., and M. S. Halpert, 1989: Precipitation patterns associated with the high index phase of the Southern Oscillation. *J. Climate*, **2**, 268-284

Rowell, D. P., 2005: A scenario of European climate change for the late 21st century: seasonal means and interannual variability. *Clim. Dyn.*, **25**, 837-849

Rowell, D. P., and R. G. Jones, 2006: Causes and uncertainty of future summer drying over Europe. *Clim. Dyn.*, **27**, 281-299

Saturaro, G., 2003: A close look at the climatological discontinuities present in the NCEP/NCAR reanalysis temperature due to the introduction of satellite data. *Clim. Dyn.*, 21, 309-316

Singh, R., Wagener, T., van Werkhoven, K., Mann, M.E. and Crane, R. 2011: A trading-space-for-time approach to probabilistic continuous streamflow predictions in a changing climate – accounting for changing watershed behavior. *Hydrol. Earth Syst. Sci.*, **15**, 3591-3603.

Shortle, J., D. Abler, S. Blumsack, R. Crane, Z. Kaufman, M. McDill, R. Najjar, R. Ready, T. Wagener, and D. Wardrop, 2009: Pennsylvania Climate Impact Assessment, Report to the Department of Environmental Protection. Environment and Natural Resources Institute, The Pennsylvania State University.

Tebaldi, C., Hayhoe, K., Arblaster, J.M., Meehl, G.A., 2006. Going to the extremes: An intercomparison of model-simulated historical and future changes in extreme events. *Clim. Change,* **79**, 185-211.

Tennant, W., 2004: Considerations when using pre-1979 NCEP/NCAR reanalyses in the southern hemisphere. *Geophy. Res. Lett.*, **31**, L11112, DOI: 10.1029/2004GL019751

Thompson, D. W. J., and J. M. Wallace, 2001: Regional climate impacts of the Northern Hemisphere annual mode. *Science*, **293**, 85-89

Thomson, M. C., F. J. Doblas-Reyes, S. J. Mason, R. Hagedorn, S. J. Connor, T. Phindela, A. P. Morse, and T. N. Palmer, 2006: Malaria early warmings based on seasonal climate forecasts from multi-model ensembles. *Nature*, **439**, 576-579

Timmermann, A., J. Oberhuber, A. Bacher, M. Esch, M. Latif, and E. Roeckner, 1999: Increased El Niño frequency in a climate model forced by future greenhouse warming. *Nature*, **398**, 694-697

Trenberth, K.E., P.D. Jones, P. Ambenje, R. Bojariu, D. Easterling, A. Klein Tank, D. Parker, F. Rahimzadeh, J.A. Renwick, M. Rusticucci, B. Soden and P. Zhai, 2007: Observations: Surface and Atmospheric Climate Change. In: *Climate Change 2007: The Physical Science Basis. Contribution of Working Group I to the Fourth Assessment Report of the Intergovernmental Panel on Climate Change* [Solomon, S., D. Qin, M. Manning, Z. Chen, M.

Marquis, K.B. Averyt, M. Tignor and H.L. Miller (eds.)]. Cambridge University Press, Cambridge, United Kingdom and New York, NY, USA.

Van Oldenborgh, G. J., S. Y. Philip, and M. Collins, 2005: El Niño in a changing climate: A multi-model study. *Ocean Sci.*, **1**, 81-95

Wagener, T., M. Sivapalan, P. A.Troch, B. L.McGlynn, C. J. Harman, H. V. Gupta, P. Kumar, P. S. C.Rao, N. B.Basu and J. S. Wilson, 2010: The future of hydrology: An evolving science for a changing world. *Water Resources Research*, **46**, W05301, doi: 10.1029/2009WR008906.

Wallace, J. M., and D. S. Gutzler, 1981: Teleconnections in the geopotential height field during the northern hemisphere winter. *Mon. Wea. Rev.*, **109**, 784-812

Wanner, H., S. Brönnimann, C. Casty, D. Gyalistras, J. Luterbacher, C. Schmutz, D. B. Stephenson, and L. Xoplaki, 2001: North Atlantic Oscillation- concepts and studies. *Surveys in Geophys.*, **22**, 321-382

Wilby, R. L., and T. M. L. Wigley, 1997: Downscaling general circulation model output: a review of methods and limitations. *Progress in Physical Geography*, **21**: 530-548

Willett, K. M., P. D. Jones, P. W. Thorne, and N. P. Gillett, 2010: A comparison of large scale changes in surface humidity over land in observations and CMIP3 general circulation models. *Environ. Res. Lett.*, **5**, doi:10.1088/1748-9326/5/2/025210

Wolff, C. G. H. Haug, A Timmermann, J. S. Sinninghe Damsté, A. Brauer, D. M. Sigman, M. A. Cane, D. Verschuren, 2011: Reduced interannual rainfall variability in East Africa during the last ice age. *Science*, **333**, 743-747

Wood, A. W., E. P. Maurer, A. Kumar, and D. P. Lettenmaier, 2002: Long-range experimental hydrologic forecasting for the eastern United States. *J. Geophys. Res.,* **107**: NO. D20, 4429, doi:10.1029/2001JD000659

----, L. R. Leung, V. Sridhar, and D. P. Lettenmaier, 2004: Hydrologic implications of dynamical and statistical approaches to downscaling climate model outputs. *Climatic Change*, **62**: 189-216

Yeh, S. W., J. S. Kug, B. Dewitte, M. H. Kwon, B. P. Kritman, and F. F. Jin, 2009: El Niňo in a changing climate. *Nature*. **461**, 511-514

Yin, J. H., 2005: A consistent poleward shift of the storm tracks in simulations of 21st century climate. *Geophys. Res. Lett.*, **32**, L18701, doi: 10.1029/2005GL023684

Van Oldenborgh, G. J., S. Y. Philip, and M. Collins, 2005: El Niño in a changing climate: A multi-model study. *Ocean Sci.*, **1**, 81-95

Zelle, H., G. J. van Oldenborgh, G. Burgers, and H. Dijkstra, 2005: El Niño and greenhouse warming: results from ensemble simulations with NCAR CCSM. *J. Climate*, **18**, 4669-4683

VITA
Liang Ning

Liang Ning was born on June 4th, 1982 in Shandong, China. He entered the Department of Atmospheric Science in Nanjing University in September 2000 and received his B.S in Atmospheric Sciences in June 2004. Then, he continued his graduate study in Department of Atmospheric Science in Nanjing University, and worked with Prof. Yongfu Qian. He finished his master thesis titled "The Analysis on the Trends of Precipitation and the Mechanism of the Increase of the Extreme Precipitation over China in 1990s" , and received his M.S. in Meteorology in June 2007. The results from this research were published in three different papers. After his graduation from Nanjing University, he entered the Pennsylvania State University in September 2007 to pursue a Ph. D. in Meteorology. Since then, he has been working on climate analysis and statistical downscaling under supervision of Dr. Michael E. Mann.

Liang Ning married Lili Lei in 2007, and they have a daughter, Ellie Yuxuan Ning, born on March 2011.